ASSOCIATION OF POLYMERS AND SMALL SOLUTE MOLECULES WITH PHOSPHOLIPID MEMBRANES

Yachong Guo

ASSOCIATION OF POLYMERS AND SMALL SOLUTE MOLECULES WITH PHOSPHOLIPID MEMBRANES

Yachong Guo

ASSOCIATION OF POLYMERS AND SMALL SOLUTE MOLECULES WITH PHOSPHOLIPID MEMBRANES

Yachong Guo

Association of polymers and small solute molecules with phospholipid membranes

Tesis presentada para obtener el grado de Doctor en Ciencias por

Yachong Guo
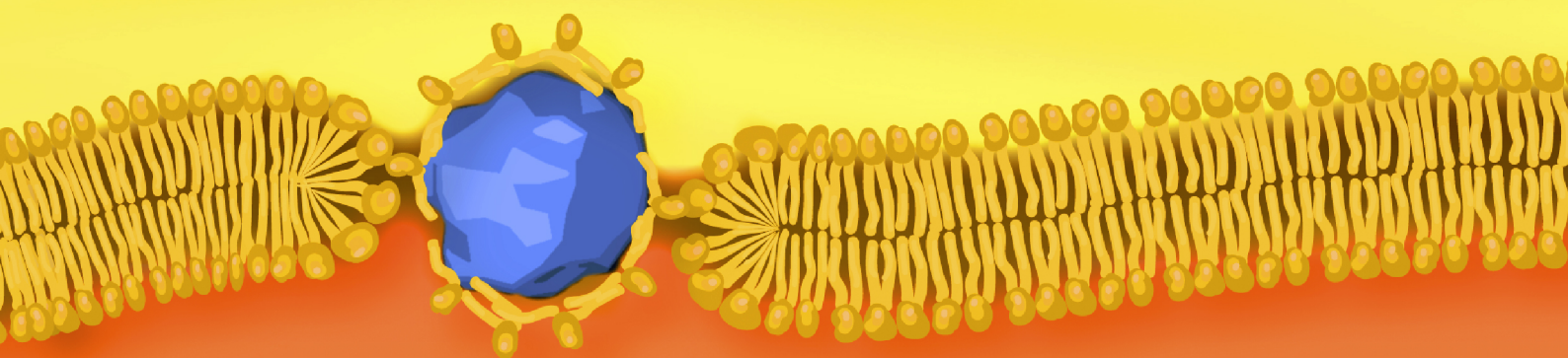
Tarragona, Spain, 2016

Yachong Guo

Association of polymers and small solute molecules with phospholipid membranes

Doctoral Thesis
Supervised by Dr. Vladimir A. Baulin

Departament d'Enginyeria Química
Molecular Simulation Group

UNIVERSITAT
ROVIRA I VIRGILI

Tarragona, 2016

UNIVERSITAT
ROVIRA I VIRGILI

Departament d'Enginyeria Química

Av. Països Catalans, 26
Tarragona 43007 (Spain)
Tel: +34 977 55 86 75
Fax: +34 977 55 96 21

FAIG CONSTAR que aquest treball, titulat "**Association of polymers and small solute molecules with phospholipid membranes**", que presenta **Yachong Guo** per a l'obtenció del títol de Doctor, ha estat realitzat sota la meva direcció al **Departament d'Enginyeria Química** d'aquesta universitat.

HAGO CONSTAR que el presente trabajo, titulado "**Association of polymers and small solute molecules with phospholipid membranes**", que presenta **Yachong Guo** para la obtención del título de Doctor, ha sido realizado bajo mi dirección en el **Departamento de Ingeniería Química** de esta universidad.

I STATE that the present study, entitled "**Association of polymers and small solute molecules with phospholipid membranes**", presented by **Yachong Guo** for the award of the degree of Doctor, has been carried out under my supervision at the **Department of Chemical Engineering** of this university.

Tarragona, Febrer 1, 2016 / Tarragona, Febrero 1, 2016 / Tarragona, February 1, 2016

El/s director/s de la tesi doctoral
El/los director/es de la tesis doctoral
Doctoral Thesis Supervisor/s

Dr. Vladimir A. Baulin

UNIVERSITAT ROVIRA I VIRGILI
ASSOCIATION OF POLYMERS AND SMALL SOLUTE MOLECULES WITH PHOSPHOLIPID MEMBRANES
Yachong Guo

Ohana means family.
Family means nobody gets left behind, or forgotten.

— Lilo & Stitch

I was so alone, and I owe you so much

— John Watson

This thesis is dedicated to
the company of my grand parents MingZhi Xu, Wen Liu
For their endless love, support and encouragement

the loving memory of my parents Wenhong Xu and Jin Guo
For all the love in my heart, all the faith in my soul
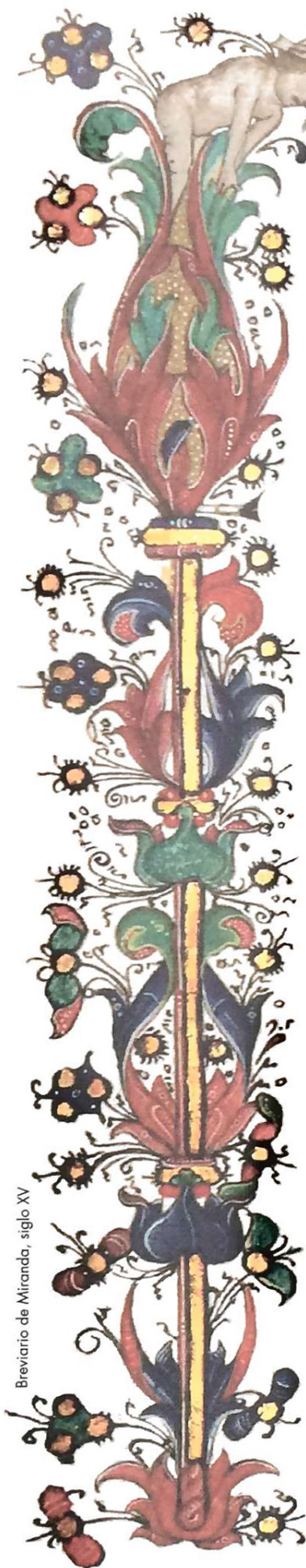
Breviario de Miranda, siglo XV

Códice Calixtino

apitulum huius Almae Apostolicae et Metropolitanae Ecclesiae Compostellanae, sigilli Altaris Beati Iacobi Apostoli custos, ut omnibus Fidelibus et Peregrinis ex toto terrarum Orbe, devotionis affectu vel voti causa, ad limina SANCTI IACOBI, Apostoli Nostri, Hispaniarum Patroni et Tutelaris convenientibus, authenticas visitationis litteras expediat, omnibus et singulis praesentes inspecturis, notum facit: Dnum

Yachong Guo

hoc sacratissimum templum, perfecto Itinere sive pedibus sive equitando post postrema centum milia metrorum, birota vero post ducenta, pietatis causa, devote visitasse. In quorum fidem praesentes litteras, sigillo eiusdem Sanctae Ecclesiae munitas, ei confert.

Datum Compostellae die 15 mensis Octobris anno Dni 2015

Vicarie Pro: Mingzhi Xu.
Wen Liu.

Segundo L. Pérez López
Decanus S.A.M.E. Cathedralis Compostellanae

ABSTRACT

Present work is devoted to the development and practical applications of several theoretical and simulation methods including Molecular dynamics, Monte Carlo and Mean field calculations to understand the physical properties of the lipid bilayer system as well as the interaction of nano-scale object in contact with lipid bilayers. In partcular, the work covers the following topics: 1. Optimization and equilibrium properties of lipid bilayers using Single Chain Mean Field theory. 2. Developing the model and study the equilibrium properties of bilayers with oxidized lipids with mean field and molecular dynamics methods 3. Study the equilibrium properties of bilayer with nanoparticles using mean field and Monte Carlo methods4. Optimization of translocational polymer through membrane GPU technique 5. Statistical methods used to the surface properties of micro blades disrupting lipid bilayers.

All knowledge is, in the final analysis, history.
All sciences are, in the abstract, mathematics.
All methods of acquiring knowledge are, essentially, through statistics.

— **C.R. Rao**

ACKNOWLEDGMENTS

This thesis represents not only my work at the keyboard, it is a milestone in three years work in Europe. It is a great pleasure to acknowledge here all the people and organizations who were supporting me all the way through my PhD study, and made this thesis completion possible.

First and foremost I wish to thank my supervisor, Dr. Vladimir A. Baulin for his excellent guidance, caring, patience. Thanks to him I had the opportunity to come to Europe to manage the project. He helped me come up with many great ideas and guided me over through. During the most difficult times in between, he gave me the support and the freedom I needed to move on. And thank you for three years of trips to the mountains, villages, sea and ski.

Dozens of people have helped and taught me immensely during my study in Europe. Important scientific contribution to this work, in form of inspiring and fruitful discussions, was done by many colleagues from many different institutes. Prof. Fabrice Thalmann welcomed me to the L'Institut Charles Sadron many times during my stay, also where I meet a great friend Dr. Olivier Benzerara. They have been a source of knowledge and energy ever since, amazing help and support from both of them in my study and life and wonderful time we have been spent together in Strasbourg. And thank you to Olivier for many times of hosting me in your room, I indeed enjoy a lot of your cooking and wine.

A special group from Dresden is not mentioned yet, because they deserve their own part: the Leibniz-Institut für Polymerforschung, special thanks to Hauke Rabbel, Marco Werner, who as a great friend and superior scientist have been amazing help all this time and offer me a place to stay when I am in Dresden. And thank you Marco Werner and your girlfriend Steffi for hosting me one month in your apartment, I indeed like your birds and the cooking.

I would like to thank Dr. Jean-Baptiste Fleury, who as a good friend, for all the useful discussion and helpful advise. And his kindful invitiation to visit his group in Universität des Saarlandes in German. And I enjoy a lot talking with you. Especially your French accent xD.

I would like to thank Dr. Vladimir Loncar from Institute of Physics, Belgrade, Serbia for the guidance, useful discussion and help during my learning period of

人生每一次抉择需要多大的力量，又有多少力量来自孤独着的坚强？无论左转右行，我们总会孤独地穿越一片黑暗之地。那么，是否有一群人，他们在最美的时光陪伴你，在你最需要的时候帮助你，爱护你。这一路来的陪伴，爱与包容的付出，是否让你在多年以后，心中还是一样的温暖。所有帮助过，爱护过，鼓励过我的人们，是你们，给我插上了翅膀，让我不会跌落万丈深渊，也让我看到了更高的天空。对于你们所做的，我无以为报，只希望我不会辜负你们为了我付出的心血和尊严，也希望有一天我能回报给你们。

终将有一天，我要背上行囊登船了。不是那艘钢铁巨兽，只是一叶很小的竹筏。我会努力扎起薄弱的帆，希望你能看见一点遥远的白色。或许在深邃的宇宙中，偶尔你能注视一眼。那就会让我知道，你安全地降落在另一片土地上，欢歌笑语，我们已经记不起什么叫作惆怅。

你将去到一个本该属于你的城市，你将在那里继续你的学业或者事业，那里有你的爱人和儿时的伙伴，那里的冬天漫天飞雪或者四季如春，而留在这里的人们，继续做着他们的欧洲梦。希望你带着童心与梦想上路，不为世俗所污染，也希望你在陌生的城市保护好自己，如果能再见，一定要比现在更好。

海天在望，不尽依迟

致

我最爱的亲人们，朋友们，导师们

CONTENTS

LIST OF FIGURES

LIST OF TABLES

LISTINGS

ACRONYMS

1

MOTIVATION AND GOALS

1.1   FOREWORD

The regulations [1] of the Chemical Engineering Department of the Universitat Rovira i Virgili allows a student to manage his doctorate thesis out of his publications in peer-reviewed journals with high impact factors, with at least two articles published during his doctorate study. Usage of this option brings the format of the present thesis book. First chapter presents the introduction, motivation and goals of the study. Next six chapters contain reprints of the articles written during the study.

1.2   LIPID AS A MATTER OF FAT

All the living organisms in the world are divided into three categories: the eukaryotes, the eubacteria and the archaebacterial, are often considered the last two together as prokaryotes.[2–4] Eubacteria usually refers to the common bacteria we meet in daily life, while the Archaebacterial can be find in rather extreme environment in most cases such as deep under the sea. Eukaryotes are known for most of us as animals plants fungis and yeast. Although they have different shape, size and activity, eukaryotes, eubacteria and archaebacterial all share the same building blocks and based on the same small organic molecules which can be essentially summarized into 4 groups: sugars, amino acids, nucletides and fatty acids.[4–6]

Figure 1: Left) Eukaryotes: human red and white blood cells with thrombocyte in middle Middle) Archaebacterium: Halobacteria Right) Eubacterium: Escherichia coli

Among the molecules of life as we presented above, lipid and fatty acids plays an unique and important role in nature.[2, 4, 7] Lipids tend to assemble into lipid membrane. A cell membrane usually is composed of billions in quantity with hundreds in kind of lipid molecules as the basic repeat units, and various types of proteins, sugar molecules, glycolipids, especially for proteins, typically occupy 50% of membrane volume and responsible for many different biological activities.[8] Cell membranes have many important physiological functions: they maintain a stable metabolism of the intracellular environment, modulate and select bio-molecules that can penetrate inside the cell. The molecules interacting with cell membrane can be absorbed, digested or excreted from the membrane through different processes like pinocytosis, phagocytosis, exocytosis [9]. Such selectivity of the cell membranes

guarantees relatively stable intracellular environment and the orderly operation of varieties of biochemical reactions [10].
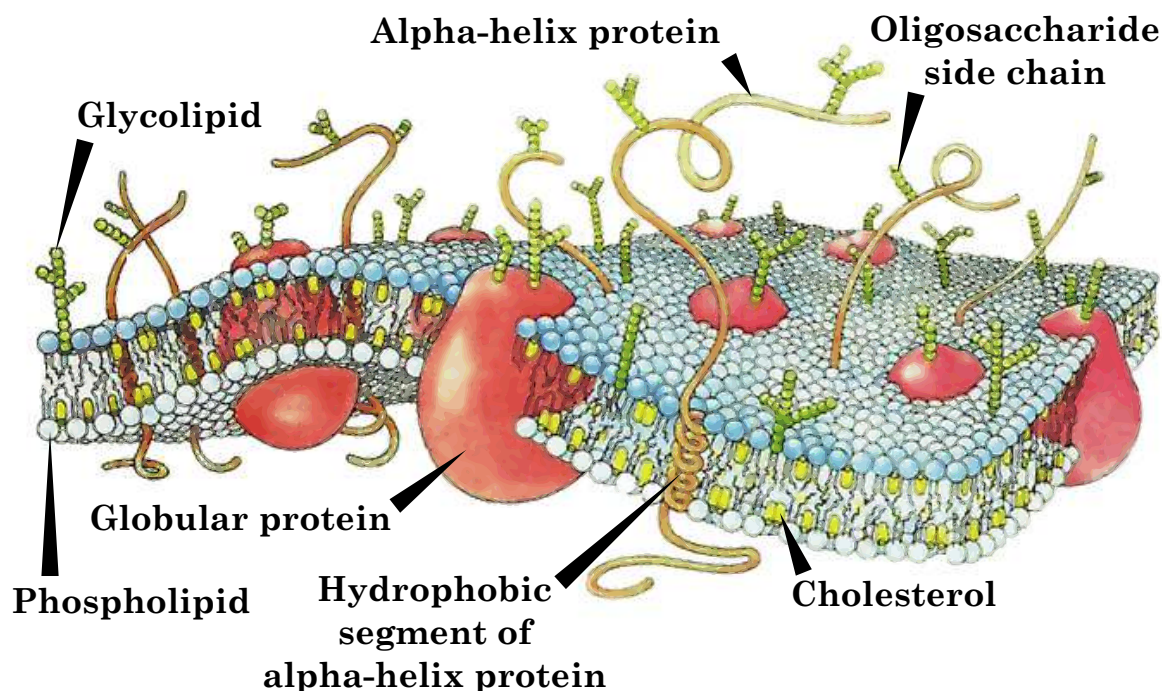
Figure 2: Schematic three dimensional cross section of a cell membrane.

There exists several mechanisms to transport an object into the cell membrane. First, is a passive translocation, which does not require energy, for example by diffusion process, where the molecules such as oxygen cross the membrane driven by the conceration difference between inside and outside of the cell. Many metabolites exit the cell through this mechanism. Especially when the concentration is larger outside, this process i also known as osmosis. However, for the active transport, sometimes toxic substances or needed nutrients must be transported across the membrane against the concentration gradient. For such case, it takes the additional energy from cell to trigger the movement of material conquer the concentration gradient, this process is usually associated with transport proteins. There is still another active way that material get into the cell called vesicular transport also know as cytosis, from the greek for "cell action". When vesicle transport materials outside of a cell, its called exocytosis, which is usually for transportting relatively large material, after the material is systensised of ready prepared by cell, it is packed into vesicles and transport until reaches the membrane, when they come into close, the two bilayer rearrange to fuse into one and in the end the material is released out from cell, reverse the process is also possible and known as endocytosis.[4, 10]

When an nano scale object such as synthetic polymers, proteins, nanoparticles and nanotubes come approach the cell membrane, it has been reported in literature that these nanoparticle can adapt their structure and change selective permeability of substances through the bilayers.[10–17]The understanding and the controling of the interaction between nanoobject and lipid bilayer is key to many applications

in various field such such as nanotoxicology[18–20], anesthesiology[21, 22], drug delivery[10–12], nanotherapy[13, 23], biomedical engineering[24], biosensor development[25, 26], toiletries and cosmetics[27].

1.3 EXPERIMENTAL METHODS

Nowdays, there are a lot of experiments going on in the direction of studying the smart nano scale object interacting with the phophatelipids membranes[11, 28]. There are many experimental techniques have been employed to characterize the structural and dynamical properties of cell membrane. Here we summarize the advantage and disadvantages of several classic techniques.
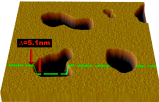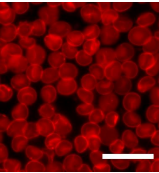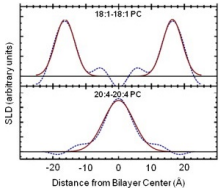
Although the experimental can provide us lots of the properties of the lipid system, however as we summarized above, The resolution of the microscopies we applied is still not high enough to see into all detail of how individually each lipid interacting with themselves or other object. Apart from that, the alternation of the membrane may be introduced during the sample preparation process, which is hard to look into how much the sample is modified from its natural state.

1.4 THEORETICAL METHODS

Processes of membranes derives greatly on time, length and energy scale, which result in a range of models and computational techniques have been created for problems at different scale[35–37]. We roughly summarize and categorize them into Figure 3. The most detail model is the atomistic model, it gives a chemical accuracy to the system by considering the atoms of all moleculars in the system. With enormous work in literature[38–40], atomistic model have been successfully applied to look into specific structural and energetic properties of membrane system.

Although employing atomistic model brings faithful, detailed information of the simulation system, even combined with efficient code and the powerful high performance computer, they are still extremely computationally expensive. When the system comes to require certain time and length scales involved in collective membrane phenomena, the methods may take years. A strategy to solve this problem is to utilize so called coarse grained model which instead of describing the model from atomic length scale but rather grouping certain number of atoms into one effective spherical beads. By this, the degree of freedom of the system is reduced and the interactions are also smoothed on certain coarse grained level respectively with the effect that a larger time and length scale is accessible. Obviously, under the concept of coarse graining, the whole system will be based on certain approximation and the accuracy of the result get lost compared with atomistic simulation. Therefore, even coarse grained model cloud brings us many advantages, one should

Table 1: Optical, chemical and physical probing methods to characterize lipid bilayer

	Advantages	Disadvantages
Atomic Force Microscopy[29] 	• High resolution of 30 nm in lateral 0.1 nm in vertical	• Require the membrane absorbed on a substrate • May stratch or even damage the membrane with AFM-tip
Fluorescent microscopy[30] 	• High resolution around 100 nm	• Can only observe fluorescent labeled samples • Fluorescent tag may induce artefacts
Electron microscopy [31] 	• High resolution of nanometer or higher	• EM require the samples to be under vacuum causing the difficulties in sample preparation
Neutron [32] and X-ray scattering[33] 	• Suitable for studying the structural properties of membrane due to that microscopy is typically two-dimensional and cannot visualize a thick sample. • Do not require staining process as usually in microscpy, the sample is untouched • Interpret and quantify disorder system in microscopy	• Relatively large amounts of samples are needed
Electrical measurements[34] 	• To directly study the transportation of chemicals through membrane • Can be used to detect nanometer size objects penetration and pore formation	• Unlike the microscopy images the data of electrical measurements can hardly be directly understood

pay enough attention when they try to apply and make sure that it maintains the balance between the efficiency and the accuracy simultaneously.

Molecular simulation [41–45] makes a good complementation for the experiments way to study lipid membrane composition at molecular level. It build a bridge between microscopic length and time scales and the macroscopic world of the laboratory. Microscopic behavior of molecular motion can be accessed with theoretical and simulation methods. A detailed equilibrium structure of lipid membrane can be achieved, as well as the essential thermodynamic properties. In addition, the microscopic details may give a better grasp of membrane active molecules such as anesthetics, nanoparticles, peptides membrane active polymers associated with the membrane. Standard simulation technique for study lipid membranes is Molecular Dynamics [23, 41, 46–48] and Monte Carlo simulations [42, 48–51].

Molecular Dynamics simulation method is a classic method which has been widely applied into studying the physical properties of many body systems. The time revolution of the atoms and moleculars are calculated by numerically solving Netween equations of motion, the energy and trajectories profile obtained from the simulation can then be used to characterize most important physical principals of the system and give a detail look into the explanation hidden behind the macroscopic world in the lab. However, despite the gaining popularity of molecular dynamics, the computer efficiency has always been a difficult problem, although the microprocessors based on Central Processing Unit (CPU) has gained a rapid performance increases and cost reduction in the past century, the computational time remains to be a challenge for the sake of the balance between the accuracy of system and efficiency. Besides, depending on the size of the simulation system and the coarse grained level, the relaxation time can also be quite long.
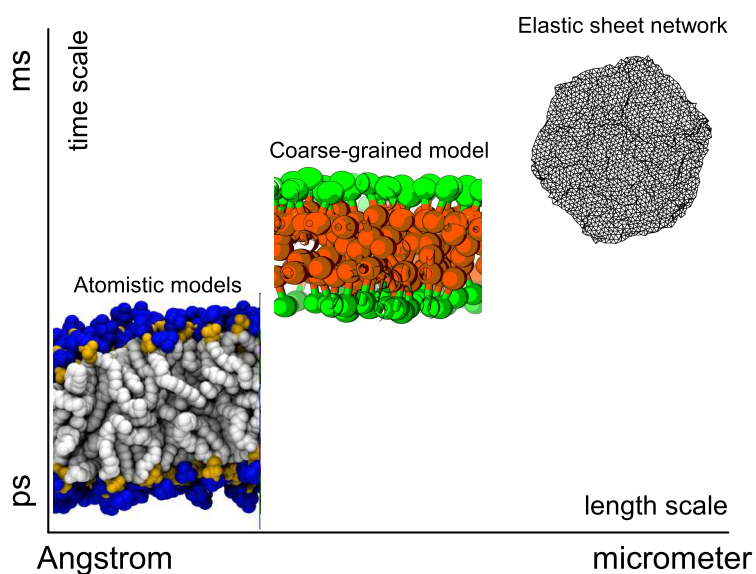
Figure 3: Coarse grained level of membrane models depending on time, length and energy scale

Monte Carlo method, compared with molecular dynamics, the configuration of the system is neither continuous nor connected in time and each configuration is only depending on its current state. New configuration can be generated randomly, weather to accept or not of this new generated configuration is judged by certain probability associated with the energy between the new and old configuration. This judging process is more properly refereed to as the Metropolis monte carlo process. Furthermore, the monte carlo simulation can be divided into two categories: the static and the dynamic.

Althrough the capability and popularity of MD and MC are growing fast,, Additional there are many hybrid techniques which integrate the features from both MD and MC, many other method, have been developed and used for a more specific task and mission, can also look into the detail of the physical system perspectively. One of a recent work is called Single Chain Mean Field (SCMF) theory, has been applied to study the equilibrium composition of lipid membranes. Different types of coarse-grained model (3-bead-type, 10-bead-type, 44-bead-type) of the cell membrane lipid (DMPC) were introduced. Based on the result, essential equilibrium properties of the phospholipid bilayer such as compressibility constant, volume fraction, the free energy and the area per lipid can be obtained with good precision and in accordance with experimental data. The best results are shown for 3-bead model, which is good enough to reproduce the essential mechanic and thermodynamic properties of lipid membranes. However, such model is too coarse-grained to describe the difference between different types of lipids and more detailed, more beads model is necessary to describe their mixtures. With more beads and more detailed structure, we can gain access to more detailed microscopic information.

Due to the large length scale and large time scale in reaching equilibrium state, they are computational expensive.

1.5 GOALS OF THE PROJECT AND OVERVIEW

The major work of this PHD is focused on doing simulation with theoretical approach to analyze the thermodynamic and mechanical properties of cell membrane through biopolymers and small solute molecules such as anesthetics or neurotransmitters. The hypothesis is the assumption based on SCMF theory which will be mentioned in next part.

There are several scientific goals were set in the beginning of this work:

- Optimization and equilibrium properties of the lipid based on SCMF

- Equilibrium properties of bilayer with oxidized lipids

- Equilibrium properties of bilayer with nanoparticles

- Optimization of translocational polymer through membrane with GPU technique

- Characterize the surface properties of micro blades killing bacteria

We introduce the Coarse-grained model for saturated phospholipids: 1,2-didecanoyl-sn-glycero-3-phosphocholine (DCPC), 1,2-dilauroyl-sn-glycero-3-phosphocholine (DLPC), 1,2-dimyristoyl-sn-glycero-3-phosphocholine (DMPC), 1,2-dipalmitoyl-sn-glycero-3-phosphocholine (DPPC), 1,2-distearoyl-sn-glycero-3-phosphocholine (DSPC) and unsaturated phospholipids: 1-palmitoyl-2-oleoyl-sn-glycero-3-phosphocholine (POPC), 1,2- dioleoyl-sn-glycero-3-phosphocholine (DOPC) within the single chain mean field theory. We reproduce[52] the thickness of the bilayer and its hydrophobic core, the compressibility, and the equilibrium area per lipid correspond to experimentally measured values for each lipid and compare them with the existing results, this work can be found in the Chapter 2.

Further the influence of different size of nanoparticles on the translocation through the membrane was explored. We demonstrate theoretically how hydrophobic nano particles with diameters larger than 6 nm can cross lipid bilayers with almost no energy barrier, while smaller hydrophobic nanoparticles stay trapped in the bilayer. This size-dependent translocation of individual nanoparticles was also directly observed in situ by optical uorescence microscopy and electrophysiological measurements in a micro fluidic device. The kinetic pathway of a single nanoparticle passive translocation event was directly measured and analyzed. Chapter 3 describe the results of this part of the work

Also on the model scale, We present here an original model for coarse-grained peroxidized lipid membrane simulations, and compare our findings with the experimental available data of ref. [53]. Our approach provides new insight on the lipid reorganisation following peroxidation[54]. The normal-oxidized lipid mixing properties will also be briefly discussed. All the work is summarized in Chapter 4.

We present a CUDA-platform-based parallel implementation of the Rosenbluth molecular generation methods that outperform by a factor of up to 1900 times compared with an equivalent implementation on single CPU processor. This boost will greatly shorten the simulation time in static Monte Carlo simulation related with Rosenbluth algorithm. With growing popularity and performance of GPU structure, our method can be applied on different platforms and operating system serve a huge benefits in simulation efficiency with the same accuracy compared with CPU calculation. The present invention break the performance bottleneck of existing molecular conformation generating methods, significantly improving the parallel performance, and has broad application prospects in the static Monte Carlo simulation of high resolution. The work is summarized in Chapter 5.

In this project, based on the previous simulation, a project based on Optimization of membrane is proposed. we report a computational tool providing relatively fast and stable solution of the equations of the SCMF theory in different geometries and different molecule structures. With a given volume fraction of particles inside the membrane, we can generate a large sampling of configurations, a optimization can be occupied to get a ideal configuration of particles. However, limiting factor

restraining the use of the SCMF theory is the computational realization of a high speed code that can efficiently solve self-consistent equations which both a problem in code and hardware platform. The results are reported in Chapter 6

In the last part of the work, a new method of studying the surface pattern is proposed. AFM topographical profiles were analysed using original statistical method based on computational vision detection algorithm and helps in understanding the pattern effect. Both the experiments data and our analysis is presented in the Chapter 7.

2

GENERAL MODEL OF PHOSPHOLIPID BILAYERS WITHIN SCMF APPROACH
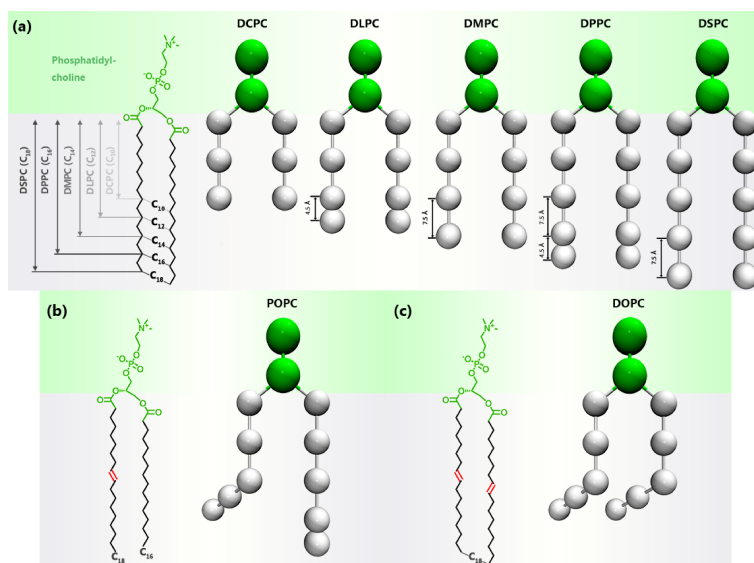
General model of phospholipid bilayers in fluid phase within the single chain mean field theory

Yachong Guo,[1] Sergey Pogodin,[2] and Vladimir A. Baulin[1]

[1]*Departament d'Enginyeria Química, Universitat Rovira i Virgili, Av. dels Paisos Catalans 26, 43007 Tarragona, Spain*
[2]*Institute of Chemical Research of Catalonia, ICIQ, Av. Paisos Catalans 16, 43007 Tarragona, Spain*

Coarse-grained model for saturated phospholipids: 1,2-didecanoyl-*sn*-glycero-3-phosphocholine (DCPC), 1,2-dilauroyl-*sn*-glycero-3-phosphocholine (DLPC), 1,2-dimyristoyl-*sn*-glycero-3-phosphocholine (DMPC), 1,2-dipalmitoyl-*sn*-glycero-3-phosphocholine (DPPC), 1,2-distearoyl-*sn*-glycero-3-phosphocholine (DSPC) and unsaturated phospholipids: 1-palmitoyl-2-oleoyl-*sn*-glycero-3-phosphocholine (POPC), 1,2- dioleoyl-*sn*-glycero-3-phosphocholine (DOPC) is introduced within the single chain mean field theory. A single set of parameters adjusted for DMPC bilayers gives an adequate description of equilibrium and mechanical properties of a range of saturated lipid molecules that differ only in length of their hydrophobic tails and unsaturated (POPC, DOPC) phospholipids which have double bonds in the tails. A double bond is modeled with a fixed angle of 120°, while the rest of the parameters are kept the same as saturated lipids. The thickness of the bilayer and its hydrophobic core, the compressibility, and the equilibrium area per lipid correspond to experimentally measured values for each lipid, changing linearly with the length of the tail. The model for unsaturated phospholipids also fetches main thermodynamical properties of the bilayers. This model is used for an accurate estimation of the free energies of the compressed or stretched bilayers in stacks or multilayers and gives reasonable estimates for free energies. The proposed model may further be used for studies of mixtures of lipids, small molecule inclusions, interactions of bilayers with embedded proteins. © *2014 AIP Publishing LLC*. [http://dx.doi.org/10.1063/1.4873586]

I. INTRODUCTION

Cell membranes represent thin and flexible layers separating the interior of the cells from the environment.[1] Specific structure of the cell membrane[2] provides the cell with numerous physiological functions: membranes maintain a stable metabolism of the intracellular environment, modulate and select small molecules and bio-molecules that can penetrate inside the cell.[2] Functional and structural properties of cell membranes are strongly related to the structure of lipid molecules.[3] Cell membranes are composed of a mixture of different types of lipids including saturated and unsaturated phospholipids, cholesterol molecules, fatty acids, proteins, and other inclusions.[2] Membrane properties and biological functions provided by cell membranes are ensured by tuned balance of membrane composition. When this balance is altered, the cell function can be modified and can even lead to certain diseases.[4]

Many functional properties of lipid membranes are determined by collective phenomena, where many molecules interact with each other and self-assemble in complex arrangements with internal structure and order.[3] In particular, a detailed microscopic description of collective phenomena in lipid bilayers may require the study of very large systems comprising of large number of lipid molecules, where atomistic Molecular Dynamics (MD) simulations are not yet practical.[5] Thus, theoretical description of large lipid systems is usually limited to coarse-grained models,[5–7] where groups of atoms are represented by effective beads, thus

reducing number of degrees of freedom in simulated systems. It is usually accepted that the coarse-graining provides an adequate and consistent description of equilibrium and structural properties of lipid bilayers.[6–8] Since lipid molecules are rather short and their conformation space is limited, the resulted equilibrium structures are determined by amphiphilic structure of molecule and thus the bilayer composition is not sensitive to details of coarse-graining.[7]

Combination of coarse-grained molecular models with mean field theories is the next step towards description of even larger lipid systems. The mechanical and structural properties of lipid bilayers can be successfully modeled within the Single Chain Mean Field (SCMF) theory.[9] The SCMF theory was originally proposed[10–12] to describe the self-assembly of surfactants into spherical micelles.[10, 12–14] Computationally expensive calculation of interactions between molecules is replaced by calculation of interactions of a single molecule in different conformations with a mean field, created by other molecules. In this approach correlations between molecules and fluctuations are neglected, while the output of the theory is equilibrium structures. This theory gives detailed molecular structure of nanoscale objects self-assembled from relatively short molecules. Since SCMF theory describes the systems in equilibrium, the free energy of different self-assembled structures can be obtained directly,[10–12] easier than in MD and Monte Carlo (MC) simulations. In addition, modifications of this theory, for example, single chain in mean field simulations,[15] can describe long-wavelength fluctuations.

In this work we propose a general coarse-grained model for the SCMF theory of most common lipids[16] found in nature that have the same polar head and differ only in the length of their aliphatic tails. This model is similar in spirit to 10-beads model described in Ref. 9, but is more accurate in description of equilibrium properties of the bilayers and can be applied to a wider range of lipids. To test the performance of our model we compare the free energy of compressed bilayers with MD simulation results[17] obtained within MARTINI force field.

II. GENERAL MODEL OF SATURATED AND UNSATURATED PHOSPHOLIPIDS

SCMF theory of lipid bilayers[9,18] describes lipid molecules in a coarse-grained approximation as a group of connected beads interacting via effective pairwise potentials. Each bead represents several atoms while the number of atoms in the bead depends on the level of coarse-graining. In contrast to widely used Self-Consistent Field (SCF)[19,20] theories, there is no *a priori* assumption on the probability distribution of conformations of molecules; instead, representative sampling[10] of conformations is generated using Monte Carlo or Rosenbluth methods.[21] Thus, this method provides more adequate description for short molecules which have non-Gaussian probability distribution of conformations, which is the case for lipids. Explicit generation of the sampling allows to split the interactions of the molecules into intra- and intermolecular parts. Intra-molecular interactions can be calculated explicitly for each conformation during the generation of the sampling, while intermolecular interactions are replaced by interactions of each conformation with mean-fields created by other molecules or external fields. Thus, the probability of each conformation Γ is fixed by a given distribution of mean fields, while the mean fields are calculated as averages over all conformations with their probabilities, hence closing the self-consistency loop. Such strategy allows to write a set of self-consistent non-linear algebraical equations, which can be solved numerically.

SCMF method applied to lipid bilayers is summarized in Ref. 9, here we list the resulting expressions. The probability of each conformation Γ,

$$\rho(\Gamma) = \frac{1}{Z} e^{-\frac{H_{eff}(\Gamma)}{kT}}, \tag{1}$$

normalized by the normalization constant Z, is given by the effective Hamiltonian, $H_{eff}(\Gamma)$, which is determined by distributions of the mean fields,[9,18]

$$\begin{aligned}
\frac{H_{eff}(\Gamma)}{kT} &= U_0(\Gamma) + (N-1)\left(\int u_T(\Gamma, \mathbf{r}) \langle c_T(\mathbf{r}) \rangle \, d\mathbf{r} \right. \\
&\quad \left. + \int u_H(\Gamma, \mathbf{r}) \langle c_H(\mathbf{r}) \rangle \, d\mathbf{r} \right) \\
&\quad + \int u_S(\Gamma, \mathbf{r}) c_S(\mathbf{r}) d\mathbf{r} - \int \lambda(\mathbf{r}) \phi(\Gamma, \mathbf{r}) d\mathbf{r}, \quad (2)
\end{aligned}$$

where N is the number of molecules in the system; $U_0(\Gamma)$ is the contribution from intra-molecular interactions of a particular conformation Γ; u_T, u_H, u_s, and ϕ are the contributions of each conformation to the fields of interactions of two types of beads, tails (T), heads (H), solvent molecules

(s), and excluded volume, in a particular point in space **r**. The corresponding mean fields created by the molecules are the averages over all conformations with the corresponding probability $\rho(\Gamma)$ are denoted by angular brackets. Hence,

$$\langle c_T(\mathbf{r}) \rangle = \int \rho(\Gamma) c_T(\Gamma, \mathbf{r}) d\Gamma, \tag{3}$$

$$\langle c_H(\mathbf{r}) \rangle = \int \rho(\Gamma) c_H(\Gamma, \mathbf{r}) d\Gamma, \tag{4}$$

$$\langle \phi(\mathbf{r}) \rangle = \int \rho(\Gamma) \phi(\Gamma, \mathbf{r}) d\Gamma, \tag{5}$$

$$v_S c_S(\mathbf{r}) = \phi_0 - N \langle \phi(\mathbf{r}) \rangle, \tag{6}$$

where v_s is the volume of the solvent bead and ϕ_0 is the maximum volume fraction, allowed in the system.[9] These equations are accompanied by the incompressibility condition,

$$v_S \lambda(\mathbf{r}) = \ln(v_S c_S(\mathbf{r})) + N \int \rho(\Gamma) u_s(\Gamma, \mathbf{r}) d\Gamma, \tag{7}$$

where $\lambda(\mathbf{r})$ is related to lateral pressure inside the bilayer. The interactions between the beads of lipids and the solvent are described by potential square well, which includes hard-core repulsion at the distances smaller than the sum of radii of the interacting beads and attraction or repulsion within the interaction range. This repulsion between the beads of different molecules is determined by the excluded volume field.

These nonlinear equations give distributions of lipids and solvent molecules at equilibrium and the corresponding total free energy of the system. In addition to the global minimum of the system, the solution of equations may also lead to metastable solutions with higher free energy, which may, in principle, inform on possible metastable states as well as the transition path between stable states.

Phospholipid molecules are modeled as a sequence of beads of two types, heads (H) and tails (T), as shown in Figure 1. All studied lipid molecules have the phosphatidylcholine head which is represented by two H-beads of radius equal to 3.3 Å (Figure 1(a)), which are the same for all studied lipids.

The saturated lipids differ only in length of the tails of aliphatic chains (Figure 1(a)). Thus, the coarse grained model represents the tails of lipids with hydrophobic T-beads of radius 2.5 Å, effectively grouping two or four carbon atoms according to the following rules: (i) the first T-bead, connected to the head, represents one carboxylate and one carbon group; (ii) next non-terminal T-beads represent four carbon groups; (iii) the terminal T-bead of the tail represents two or four carbon groups, depending on the length of the terminal bond (4.5 Å or 7.5 Å, correspondingly). The length of the rest of bonds is 7.5 Å, and there is no restrictions on the angles between them, i.e., the beads are freely jointed. The molecules are generated by self-avoiding walk using Rosenbluth algorithm, i.e., the beads in the resulting conformations do not intersect. The solvent molecules are represented by S-beads of radius 2.5 Å. The parameters of the model are summarized in Table I. Two types of beads tails (T) and heads (H) and solvent (S) interact through square well potentials: the interaction is equal to zero if the distance between the center of bead is larger than the interaction range, while if the
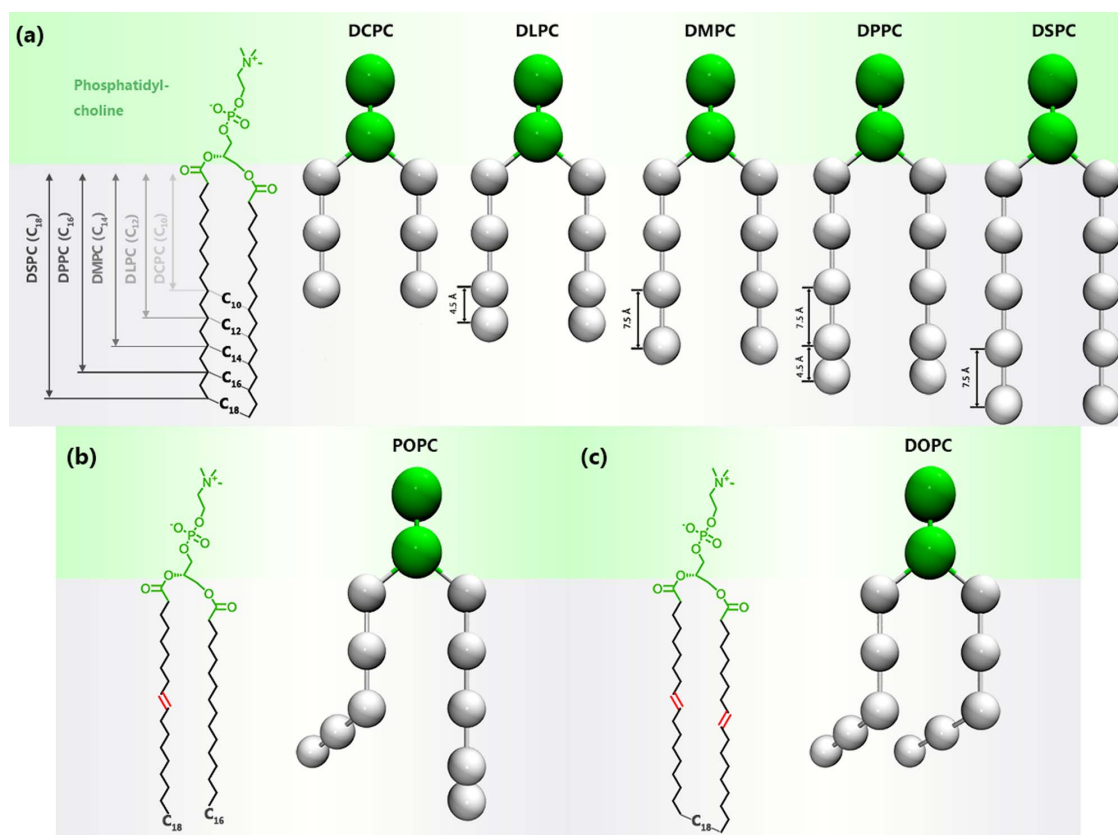
FIG. 1. (a) Chemical structure (left) and the corresponding coarse grained model (right) of saturated phospholipids 1,2-didecanoyl-*sn*-glycero-3-phosphocholine (DCPC), 1,2-dilauroyl-*sn*-glycero-3-phosphocholine (DLPC), 1,2-dimyristoyl-*sn*-glycero-3-phosphocholine (DMPC), 1,2-dipalmitoyl-*sn*-glycero-3-phosphocholine (DPPC), 1,2-distearoyl-*sn*-glycero-3-phosphocholine (DSPC) (from left to right). (b) and (c) Chemical structure and the coarse grained model of unsaturated phospholipids 1-palmitoyl-2-oleoyl-*sn*-glycero-3-phosphocholine (POPC) and 1,2- dioleoyl-*sn*-glycero-3-phosphocholine (DOPC). Green beads correspond to hydrophilic (H) and grey beads correspond to hydrophobic (T) groups (see parameters in Table I). Unsaturated lipids have a kink of a fixed angle $120°$ at the double bond.

centers of beads are within the interaction range, the interaction between the beads has a constant value listed in the table. There are only two types of interactions: between two hydrophobic beads TT and between one hydrophilic bead and solvent HS. Since the molecules are modeled as sequence of hard spheres, close packing is achieved for occupied volume fraction ϕ_0 smaller than 1, which is, in fact, a parameter of the system controlling the excluded volume interactions. In the model it is set to 0.685. The parameters of the model are adjusted through series of simulations with large sampling (7×10^7) and resolution. The simulation box (Width × Length × Height) is set to 100.0 Å × 100.0 Å × 62.7 Å and the periodic boundary conditions in lateral directions are used.

The constructed model for saturated lipids can further be extended to unsaturated lipids of a similar structure, POPC and DOPC, which have exactly the same head group and similar to saturated lipids DPPC and DSPC chemical structure (Figure 1). However, there are important differences in the molecule structure that should be reflected in the model. (i) One of the tails of POPC is shorter than the other; (ii) POPC molecule has one and DOPC molecule has two double-bonds in the middle of the fatty acid tails. Therefore,

tails of POPC have different lengths, but tails of DOPC are of the same length. As a result, in our model (Figures 1(b) and 1(c)) the lipid tail with no double bond in POPC has the same structure as the tails of DPPC, while the tail with hydrogen

TABLE I. Parameters of the coarse-grain model of saturated and unsaturated phospholipids. Phospholipids of each group differ only in the length of the hydrophobic tail (Figure 1) while the interaction parameters are the same.

Lipid model parameters	Saturated
H-bead radius (Å)	3.3
T-bead radius (Å)	2.5
S-bead radius (Å)	2.5
Interaction range (Å)	7.5
T-T contact energy (kT)	1.20
H-S contact energy (kT)	-0.15
Bond length (Å)	7.5
Terminal group bond length (Å)	4.5
Occupied volume fraction ϕ_0	0.685
Simulation parameters	
Sampling (number of configurations)	7×10^7
Simulation box size (Å)	$100.0 \times 100.0 \times 62.7$
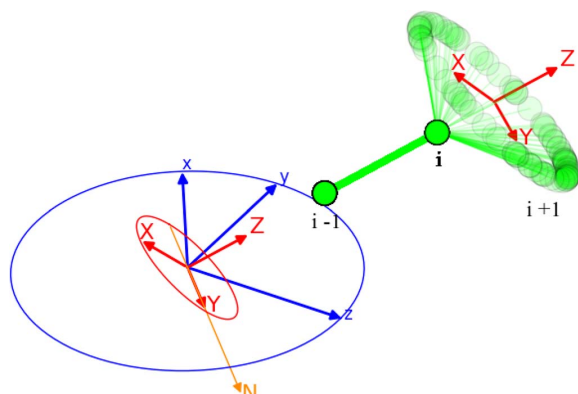
FIG. 2. Implementation of a fixed angle of a double bond in the unsaturated lipid model.

bond in POPC and both tails of DOPC have similar structure as DSPC. In addition, the bead in the middle of the tail corresponding to double bound has a fixed angle of 120°.

The implementation of fixed angle is illustrated in Figure 2. A rotated coordinate system XYZ (red) centering on the unsaturated bead i is defined with respect to a fixed coordinate system xyz, where z-axis is oriented along the extended line of the bond connecting bead i with the bead $i - 1$. xy plane is perpendicular to z-axis. The line of nodes-N (orange) is defined as the intersection of the xy and XY coordinate planes. α is the angle between x-axis and N-axis, β is the angle between the z-axis and the Z-axis. Random position of the next bead $i + 1$ is generated first in the rotated coordinate system XYZ and then transferred with rotated matrix,

$$\begin{bmatrix} \cos\alpha & -\cos\beta\cos\alpha & \sin\beta\sin\alpha \\ \sin\alpha & \cos\beta\cos\alpha & -\sin\beta\cos\alpha \\ 0 & \sin\beta & \cos\beta \end{bmatrix}, \quad (8)$$

to the original coordinate system xyz.

III. EQUILIBRIUM PROPERTIES OF LIPID BILAYERS

The equilibrium properties of unconstrained bilayers at 30 °C are calculated and compared with the experimental data for saturated DCPC, DLPC, DMPC, DPPC and unsaturated POPC, DOPC lipids, see Table II. The calculated equilibrium properties include area per lipid, volume per lipid, membrane thickness (defined by the bilayer distance between midpoint of the total volume fraction), hydrophobic core thickness (defined by the bilayer distance between midpoint of the tail beads volume fraction), distance between heads (defined by the peak value of the slopes of the head beads volume fraction), and the compressibility constant which describes the rigidity of membrane in lateral direction. It is calculated as a second derivative of the free energy versus area per lipid around the minimum of the free energy (see Ref. 9).

The experimental data are collected from different sources of X-ray scattering and corresponds to fully hydrated fluid phase. The temperature of all experimental data is 30 °C, which makes possible the comparison with simulation data. However, the main transition temperature of DPPC (Ref. 24) and DSPC is around[28] 41 °C and 54 °C correspondingly. This means that these lipid bilayers should be in a gel phase at 30 °C, at which the bilayer has completely different equilibrium and mechanical properties. In order to consider systematically all lipids with different tail lengths in the same framework, it was proposed to use experimental estimates for the effective values that lipid bilayers would have at 30 °C if they would not have undergone the transition into gel phase. To do so, the averaged molecular area expansion $k_{DPPC} = 0.190$ Å^2/deg, $k_{DSPC} = 0.167$ Å^2/deg[27] was introduced[27] to extrapolate experimental area per lipid to 30 °C. Similarly, averaged molecular thickness expansion $k_{DPPC} = 0.090$ Å/deg was used to extrapolate the membrane thickness. However, the compressibility modulus of DPPC is not accessible at such temperature.

TABLE II. Equilibrium thermodynamic and mechanical properties of saturated and unsaturated lipids obtained with the SCMF model of lipids and compared with experimental data. Theoretical data for unsaturated lipids correspond to corrected for volume data denoted by a star in Figure 3.

Lipid		DCPC	DLPC	DMPC	DPPC	DSPC	POPC	DOPC
Equilibrium area per lipid	Expt.	-	63.2[a]	60.6[b]	59.96[c]	58.79[c]	68.3[b]	72.4[b]
A_0 (Å^2)	Theor.	61.9	62.5	61.5	60.1	59.0	65.4	69.9
Volume per lipid	Expt.	-	991[a]	1101[b]	-	-	1256[b]	1303[b]
V_L (Å^3)	Theor.	978	1025	1098	1196	1283	1306	1389
Membrane thickness	Expt.	-	38.9[a]	44.2[b]	-	-	45.1[b]	44.8[b]
D_M (Å)	Theor.	35.7	39.7	43.8	45.7	48.3	45.8	45.2
Hydrophobic core thickness	Expt.	-	20.9[a]	25.4[d]	27.3[c]	-	27.1[b]	26.8[b]
D_T (Å)	Theor.	19.0	23.2	25.2	27.6	30.7	27.8	27.7
Distance between heads	Expt.	-	30.8[a]	35.3[b]	-	-	37.0[b]	36.7[b]
D_H (Å)	Theor.	27.3	30.9	34.8	37.5	40.1	37.8	37.5
Compressibility constant	Expt.	-	302[e]	257[e]	-	-	278[e]	251[e]
K_C (dyn/cm)	Theor.	313	295	272	264	248	292	279

[a]Experimental data by Kučerka et al.[22]
[b]Experimental data by Kučerka et al.[23]
[c]DPPC and DSPC are in gel phase at 30 °C and these data are extrapolated values by Kučerka et al.[27] to fluid phase values.
[d]Experimental data by Feig.[25]
[e]Experimental data by Mathai et al.[26]
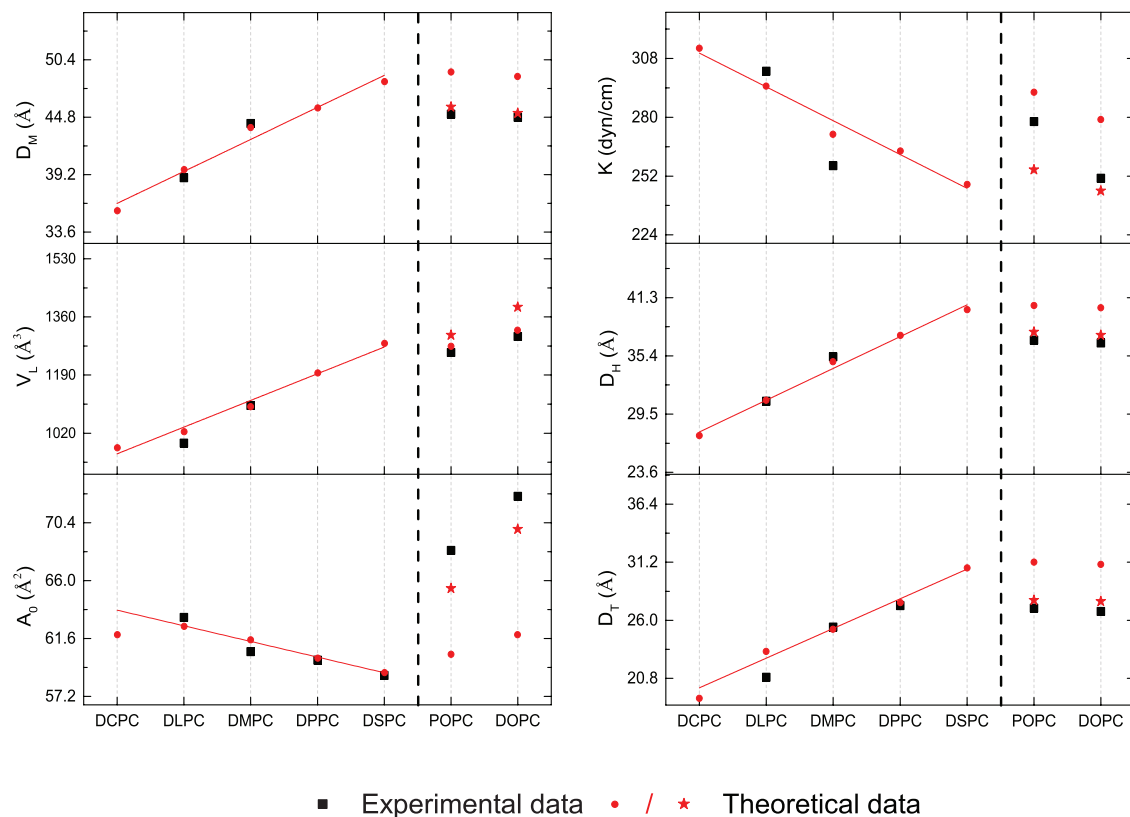
FIG. 3. Equilibrium thermodynamic and mechanical properties of saturated and unsaturated lipids obtained with the general model of lipids in SCMF theory and compared with experimental data. Solid squares represent the experimental data of DCPC, DLPC, DMPC, DPPC, DSPC, POPC, DOPC. Solid spheres represent the simulation data obtained with coarsed grained model with SCMF theory. Solid stars denote the simulation data of POPC, DOPC after considering the effect of excluded volume. A fitting curve is generated as red line based upon the simulation data of saturated lipids.

A. Saturated lipids

Good agreement between experimental and theoretical predictions of the general model is shown in Figure 3. Our model reproduces almost perfectly the equilibrium properties of bilayers assembled from saturated lipids with different tail lengths using the single set of interaction parameters. The calculated equilibrium properties for liquid phase show linear dependance with the length of the tail. The statistical error of SCMF calculations is of the order of 1% for thickness and area and 5.4% for compressibility constant, since it is a second derivative of the free energy and thus it requires large sampling to achieve a high accuracy. The thickness of the bilayers and the hydrophobic core thickness and the distance between heads increase linearly with the length of the tails, which corresponds to the increased molecular volume of the lipids. The compressibility constant and area per lipid decrease with the length of the tails. This is attributed to the increase of the TT contact energy per lipid with increased number of T beads. To analyze such behavior, we use one of the advantages of the SCMF theory, namely, the direct access to components of the total free energy at equilibrium. Figure 4 shows the dependence of the dominant terms in the total free energy: the energy of TT contacts and the entropy of lipids as a function of the lipid tails length. Other terms to the free

energy, the intra-molecular internal energy, and the energy of head-solvent (HS) interactions are small and almost constant, thus not shown. Main contribution to the free energy per lipid is the energy of TT contacts, which increases with the num-
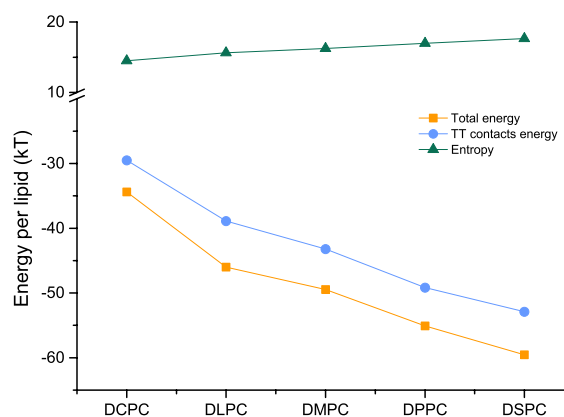
FIG. 4. Contributions to the total free energy (squares) of equilibrium saturated fatty acid liquid PC bilayers calculated within SCMF theory: the energy of TT contacts (circles) and entropy (triangles). Other contributions (intra-molecular energy and the energy of Hs contacts) are small.

ber of T beads in the tails, making the lipid more hydrophobic and thus leading to closer packing in the bilayer core region.

The average volume fraction profile of the equilibrium lipid bilayer is shown in Figure 5. It shows the total volume fraction in the bilayer as well as the distribution of heads and tails in the bilayer for three saturated lipids. Increased length of the tail leads to the increase of the thickness and increase of the head-to-head distance as reflected in Table II.

B. Unsaturated lipids

Our model of unsaturated DOPC and POPC lipids is based on the structure of saturated DPPC or DSPC lipids which have similar tail length and molecular volume, Figure 1. The only difference between saturated and unsaturated lipids is the hydrogen bonds in the middle of the tails. One possibility is to model double bounds in the tails is to fix the angle as shown in Figure 2 and keep all other parameters of saturated lipids model shown in Table I. Such model with no fitting or additional parameters gives reasonable estimates for the structure of the bilayer, thickness of the membrane and hydrophobic core, molecular volume and gives reasonable compressibility constant (red circles in Figure 3). However, the resulting area per lipid is significantly lower experimental values. This can be explained by underestimated crowding effect induced by disordered packing of tails with fixed angles. But this packing effect relies on strong correlations between neighboring lipid tails and this effect definitely goes beyond mean field and hence is not present in SCMF theory. In addition, these tails with fixed angle in the middle of the tail are difficult to align in parallel arrays, thus, impeding unsaturated lipids from phase transition to gel phase, observed for saturated lipids of the same structure and same temperature.

Fixed angle induces the distortion in the conformations of lipids which results in slightly increased average excluded volume of conformations. According to our numerical estimations based on averaging of the excluded volume of each generated conformation, the increase of the excluded volume is about 5.1% for DOPC and 2.6% for POPC. This effect was indirectly incorporated into the model of unsaturated lipid by increasing the volume of the beads by this amount. This increase of the volume of the beads has led to significantly better correspondence with experimental results as shown in Figure 3 and Table II. The consequences on the lipid bilayer structure induced by the replacement of DSPC by DOPC lipid is depicted in Figure 6. The thickness of the bilayer of unsaturated lipid is lower than that of saturated lipid because the number of lipids in the equilibrium is smaller.

IV. BILAYERS UNDER COMPRESSION

General model for saturated phospholipids is shown to be successful in description of equilibrium thermodynamic properties of single unconstrained bilayers. In order to test this model further, we consider compressed bilayers.

Double bilayer systems can be formed in two distinct experimental situations: (i) dehydration of the water layer between the bilayers, when the distance between the bilay-
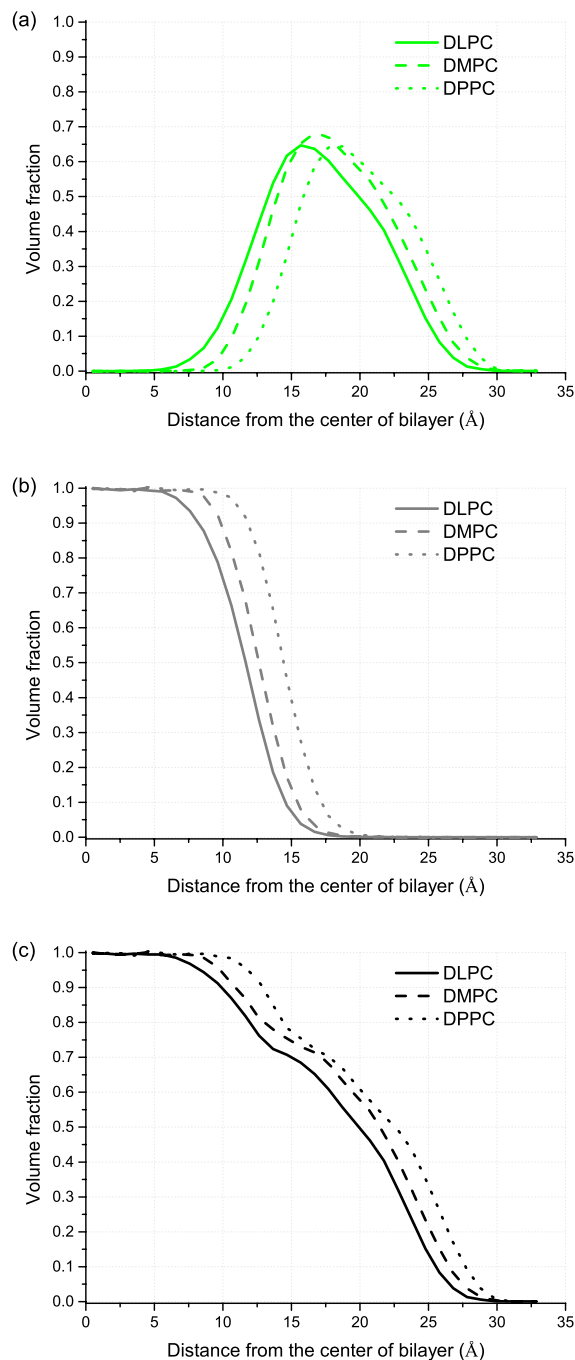
FIG. 5. Volume fraction profiles of (a) hydrophilic bead H, (b) hydrophobic bead T, and (c) total volume fraction profile of three saturated lipids given by SCMF model.

ers is controlled by hydration level (the number of water molecules per lipid)[17,29] and (ii) mechanical compression of two bilayers,[17] for example, squeezed between two parallel walls; in this case the control parameter is the distance between the centers of mass of the bilayers.
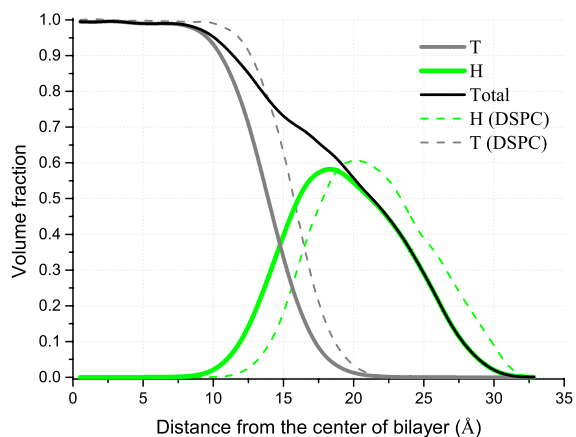
FIG. 6. Average volume fraction profile of unsaturated DOPC lipid bilayer (solid) as compared with the saturated DSPC lipid bilayer of similar structure (dashed). T represents hydrophobic and H hydrophilic heads.

FIG. 8. Disjoining pressure between two compressed POPC bilayers as a function of water layer thickness D_w in a logarithmic scale. Solid and open squares denote experimental and simulation data by Smirnova et al.,[17] solid triangles are experimental data by Varma et al.,[30] solid stars are our simulation results with SCMF model.

We choose two POPC lipid bilayers placed between non-interacting walls in order to compare with the existing experiment and simulation data. The height of the box is decreased and the number of lipids in the box is adjusted to find the minimum of the free energy. The number of lipids corresponding to the minimum of the free energy then corresponds to equilibrium area per lipid. This is similar in spirit to simulations in Grand canonical ensemble, while mechanical and thermodynamic properties of the bilayers are calculated the same way as discussed in Sec. III. Figure 7 shows a typical volume fraction profile of two compressed bilayers. In addition, another important property of the bilayer can be calculated, the disjoining pressure at a certain water layer thickness D_w which is given by[17]

$$P = \frac{2K_C}{D_{com} - D_w}\left(\frac{A_{D_{com}}}{A_0} - 1\right), \qquad (9)$$

where D_{com} is the distance between the centers of the bilayers, K_C is the compressibility modulus,[9] and A_0 is the area per lipid of a unperturbed POPC bilayer at equilibrium. In turn, $D_{com} - D_w$ denotes the thickness of single bilayer.[17] It is equal to the distance between heads of single bilayer at equilibrium, D_{hh}. Since our method can directly measure both D_{hh} and D_w, they are directly obtained from the volume fraction

profile as will be mentioned later. $A_{D_{com}}$ is the area per lipid at a given membrane thickness (D_{hh}). The initial height of box is 120 Å and decreased to 60 Å by step 5 Å. The number of lipids, free energy per lipid, and area per lipid at equilibrium state of compressed bilayers are changed with decreasing volume of the box.

Figure 8 shows a comparison of disjoining pressure corresponding to water layer thickness, collecting data from both experiments and simulations. The experimental results[30] are calculated from osmotic pressure at room temperature.[31,32] Open square represents the simulation data obtained from compressed double bilayer system using Eq. (9). Solid star represents the simulation results with SCMF theory for POPC and calculated from Eq. (9). Here the value of K_C is taken from Table II as 237 dyn/cm. It is important to note that the way to define the thicknesses D_w and D_{hh} has a great impact on the result. Several methods of definition have been explored in the literature in both experiment and simulation. Most common definition comes from X-ray scattering is the distance between the maxima in the electron density profile[23] which it often related to phosphate peaks. Here we use the same method to define D_{hh} in order to compare with

FIG. 7. Typical volume fraction profile of two compressed bilayers between two walls for POPC lipid bilayer. Green line corresponds to heads, grey line corresponds to tails, and black line is the total volume fraction.
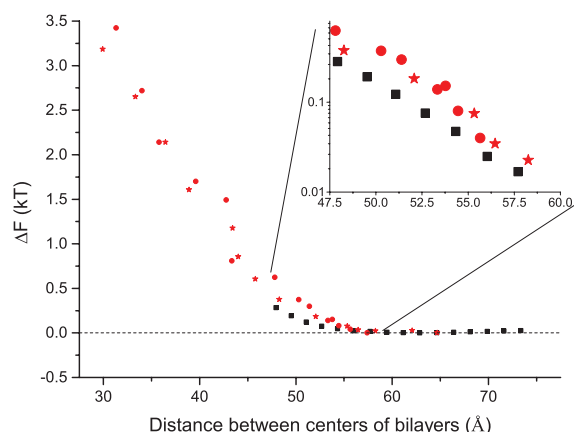
FIG. 9. Free energy cost ΔF versus the center of mass between 2 bilayers. Solid squares represent the MD simulation data obtained by Smirnova *et al.*[17] for POPC lipid bilayer with MARTINI model, stars are SCMF simulation results for POPC lipid bilayers, and solid circles are SCMF simulation for DMPC lipid bilayers.

experiment results. Since our model does not distinguish phosphate groups but has only a general hydrophilic head group, D_{hh} is defined as the head-to-head distance of a single unperturbed bilayer, D_H in Table II. The water interface of D_w is defined at the half density of solvent in our simulation. Figure 8 shows a good agreement with both experiment and simulation of our model in a compressed two-bilayer system.

The free energy cost of the equilibrium state of compressed double bilayers as a function of the distance between the centers of mass of the bilayers is shown in Figure 9. The free energy difference per lipid is calculated as a function of the free energy of unperturbed single bilayer $\Delta F = (F - F_{eq})$. We compare our simulation results (red stars and circles) with a similar double bilayer system within MD simulations using MARTINI model[17] (black squares). In highly compressed
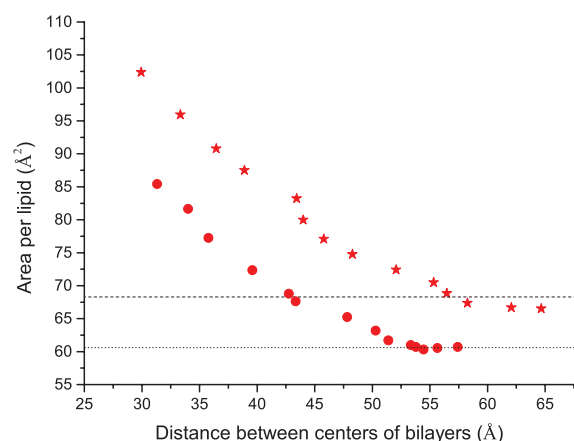
FIG. 10. Area per lipid versus centers of mass between two bilayers D_{com}, solid circle (DMPC) and star (POPC) represent the simulation results with SCMF theory. Dashed (DMPC) and dotted (POPC) lines denote the experimental value for unperturbed single bilayers for reference at infinite distances.

state, $D_{com} < 45$ Å, we find linear dependence between the free energy and the distance between centers of bilayers. For small compressions, $D_{com} > 45$ Å, our simulations show a very good agreement with molecular dynamics simulation.

Figure 10 shows the area per lipid as a distance between the centers of bilayers calculated with SCMF theory. Dashed lines correspond to equilibrium areas per lipid in unperturbed single bilayers of DMPC and POPC membranes, which correspond to two bilayers that do not feel each other. With increasing distance between bilayers the area per lipid decreases with in a similar way for saturated DMPC and unsaturated POPC lipid bilayers.

V. CONCLUSION

We propose a general model for saturated, DCPC, DLPC, DMPC, DPPC, DSPC, and unsaturated, POPC and DOPC, phospholipids which differs only in hydrocarbon chains. The lipid molecule is represented by two hydrophilic beads which are the same for all studied lipids and 6–10 beads in the tail and correspond to different number of carbons. Essential equilibrium properties of the phospholipid bilayer such as compressibility constant, volume fraction, and the area per lipid can be obtained with good precision and in accordance with experimental data. This general model is able to describe most of equilibrium properties of phospholipid bilayers such as the thickness of the bilayer and the hydrophobic core, position of hydrophilic and hydrophobic groups in the bilayer, the mechanical properties of the bilayer, and the corresponding compressibility constant. The performance of the model was tested in a two-bilayer system, where non-adsorbing membrane is compressed and the force–distance profile is measured. The model gives results, which are in good agreement with experimental data as well as with molecular dynamics simulations. The proposed model can further be used for modeling thermodynamic and mechanical properties of mixtures of lipids and interactions with nano-objects.

[1]B. Alberts, *Molecular Biology of the Cell*, 5th ed. (Garland Science, New York, 2008).
[2]P. L. Yeagle, *The Structure of Biological Membranes*, 2nd ed. (CRC Press, 2005).
[3]A. M. Dopico and G. J. Tigyi, Methods Mol. Biol. **400**, 1 (2007).
[4]B. Halliwell and J. M. Gutteridge, *Methods in Enzymology* (Elsevier, 1990), Vol. 186, pp. 1–85.
[5]M. Müller, K. Katsov, and M. Schick, J. Polym. Sci. B: Polym. Phys. **41**, 1441–1450 (2003).
[6]M. Müller, K. Katsov, and M. Schick, Phys. Rep. **434**, 113 (2006).
[7]M. Venturoli, M. M. Sperotto, M. Kranenburg, and B. Smit, Phys. Rep. **437**, 1 (2006).
[8]A. P. Lyubartsev, Eur. Biophys. J. **35**, 53 (2005).
[9]S. Pogodin and V. A. Baulin, Soft Matter **6**, 2216 (2010).
[10]A. Ben-Shaul, I. Szleifer, and W. M. Gelbart, J. Chem. Phys. **83**, 3597 (1985).
[11]I. Szleifer, A. Ben-Shaul, and W. M. Gelbart, J. Chem. Phys. **83**, 3612 (1985).
[12]A. Ben-Shaul, I. Szleifer, and W. M. Gelbart, J. Chem. Phys. **85**, 5345 (1986).

[13] Z. A. Al-Anber, J. Bonet-Avalos, and A. D. Mackie, J. Chem. Phys. **122**, 104910 (2005).

[14] A. G. Daful, V. A. Baulin, J. B. Avalos, and A. D. Mackie, J. Phys. Chem. B **115**, 3434 (2011).

[15] K. C. Daoulas and M. Muller, J. Chem. Phys. **125**, 184904 (2006).

[16] O. G. Mouritsen, *Life-as A Matter of Fat: The Emerging Science of Lipidomics* (Springer, 2005).

[17] Y. Smirnova, S. Aeffner, J. Risselada, T. Salditt, S. J. Marrink, M. Mueller, and V. Knecht, Soft Matter **9**, 10705 (2013).

[18] S. Pogodin and V. Baulin, Curr. Nanosci. **7**, 721 (2011).

[19] *Polymers at Interfaces*, 1st ed. (Chapman & Hall, London/New York, 1993).

[20] R. B. Thompson, T. Jebb, and Y. Wen, Soft Matter **8**, 9877 (2012).

[21] M. N. Rosenbluth and A. W. Rosenbluth, J. Chem. Phys. **23**, 356 (1955).

[22] N. Kučerka, Y. Liu, N. Chu, H. I. Petrache, S. Tristram-Nagle, and J. F. Nagle, Biophys. J. **88**, 2626 (2005).

[23] N. Kučerka, S. Tristram-Nagle, and J. F. Nagle, J. Membr. Biol. **208**, 193 (2006).

[24] J. F. Nagle, R. Zhang, S. Tristram-Nagle, W. Sun, H. I. Petrache, and R. M. Suter, Biophys. J. **70**, 1419 (1996).

[25] M. Feig, *Molecular Modeling of Proteins* (Springer, 2008), pp. 181–196.

[26] J. C. Mathai, S. Tristram-Nagle, J. F. Nagle, and M. L. Zeidel, J. Gen. Physiol. **131**, 69 (2007).

[27] N. Kučerka, M.-P. Nieh, and J. Katsaras, Biochim. Biophys. Acta **1808**, 2761 (2011).

[28] D. Gauger, C. Selle, H. Fritzsche, and W. Pohle, J. Mol. Struct. **565–566**, 25 (2001).

[29] E. Schneck, F. Sedlmeier, and R. R. Netz, Proc. Natl. Acad. Sci. U.S.A. **109**, 14405 (2012).

[30] V. Varma, M. Taalbi, J. Collins, W. Tamura-Lis, and L. Lis, J. Colloid Interface Sci. **133**, 426 (1989).

[31] D. M. Leneveu, R. P. Rand, and V. A. Parsegian, Nature (London) **259**, 601 (1976).

[32] C. F. McCabe and G. J. Cole, Brain Res. Dev. Brain Res. **70**, 9 (1992).

3

PASSIVE TRANSLOCATION OF LIPID-COVERED SUPERHYDROPHOBIC NANOPARTICLES
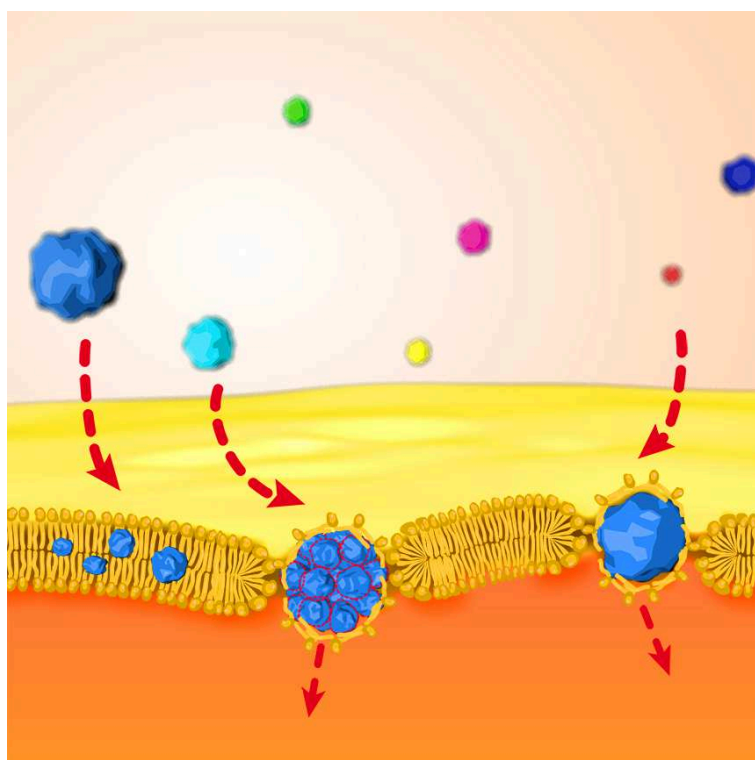
Direct Proof of Passive Translocation of Lipid-Covered Superhydrophobic Nanoparticles Through a Phospholipid Bilayer

Yachong Guo,[1] Emmanuel Terazzi,[2] Ralf Seemann,[3,4]

Jean Baptiste Fleury,[3,*] and Vladimir A. Baulin[1,†]

[1]*Departament d'Enginyeria Quimica, Universitat Rovira i Virgili,*

26 Av. dels Paisos Catalans, 43007 Tarragona, Spain

[2]*Department of Inorganic and Analytical Chemistry, University of Geneva,*

30 quai E. Ansermet, CH-1211 Geneva 4, Switzerland

[3]*Universitat des Saarlandes, Experimental Physics, 66123 Saarbruecken, Germany*

[4]*Max Planck Institute for Dynamics and Self-Organization, Goettingen, Germany*

(Dated: January 26, 2016)

Hydrophobic nanoparticles introduced into living systems may lead to increased toxicity, can activate immune cells or can be used as nano-carriers for drug or gene delivery. This generalized behavior of hydrophobic nanoparticles can be linked to their great ability to interact with cell membranes and, in particular, their affinity to the hydrophobic cores of membranes and bilayers. It is generally accepted that small hydrophobic nanoparticles can insert into a lipid bilayer and accumulate in the bilayer core, representing a potential well. However, escaping the bilayer is unlikely for these nanoparticles. In this work we demonstrate theoretically how hydrophobic nanoparticles with diameters larger than 6 nm can cross lipid bilayers with almost no energy barrier, while smaller hydrophobic nanoparticles stay trapped in the bilayer. This size-dependent translocation of individual nanoparticles was also directly observed *in situ* by optical fluorescence microscopy and electrophysiological measurements in a microfluidic device. The kinetic pathway of a single nanoparticle passive translocation event was directly measured and analyzed.

Keywords: lipid bilayers, nanoparticles, microfluidics, translocation dynamics

2

I. INTRODUCTION

Nanoparticles (NPs) of different sizes and shapes are involved in many biomedical applications because of their ability to insert into membranes and to internalize into cells.[1,2] These applications range from microscopy imaging[3,4] and cell manipulation[5,6] to diagnostics and therapeutics.[7–10] Apart from numerous practical applications, NPs may also result in increased cytotoxicity.[11] In particular, gold nanoparticles (AuNPs) may induce death of human endothelial and epithelial cells[12] and show increased cytotoxicity for other types of cells even at low concentrations.[11,13–15] Cytotoxicity of AuNPs increases with concentration and depends on the size of NPs.[15,16] In general, the surface properties of NPs have great effect on their binding capacity, membrane activity, and on their cytotoxicity.[16–19] Hydrophobic NPs can *e.g.* trigger immune response by activation of immune cells:[20] immune response increases with increasing hydrophobicity.

Despite the large variety of effects on cells, chemically inert neutral nanoparticles may be characterized by only a few parameters *e.g.* shape, size and surface properties. This may be an indication of an universal interaction behavior of nanoparticles with cell membranes, which, in turn, can be classified according to these parameters into groups with similar or exactly the same effect on cells. The difference in cell reaction on different types of nanoparticles may be attributed to different interaction mechanisms with cell membranes.

Nanoparticles of large sizes (diameter > 10 nm) usually penetrate into cells by active processes such as different types of endocytosis.[1,2,21,22] Active translocation through cell membranes is energy-dependent and requires collective action of membrane proteins and involves cytoskeleton.[21] As a result, this mechanism is slow with a characteristic time of order of seconds.[23] In contrast, small solute molecules, ions, protons, hormones,[24,25] as well as fullerenes[26,27] can translocate directly through lipid bilayer by passive diffusion. This process is energy-independent and usually takes only hundreds of nanoseconds.[24] Thus huge difference in internalization time may affect dramatically how cells respond to the presence of external substances, whereas one of the critical factors controlling the uptake mechanism is the size of these substances interacting with lipid membranes.

In turn, small hydrophobic NPs (diameter < 10 nm) can penetrate and accumulate in bilayer cores.[28] it is commonly assumed that once they are trapped in the bilayer they cannot escape from the bilayer core, which, in fact, represents a potential well. Several studies,

3
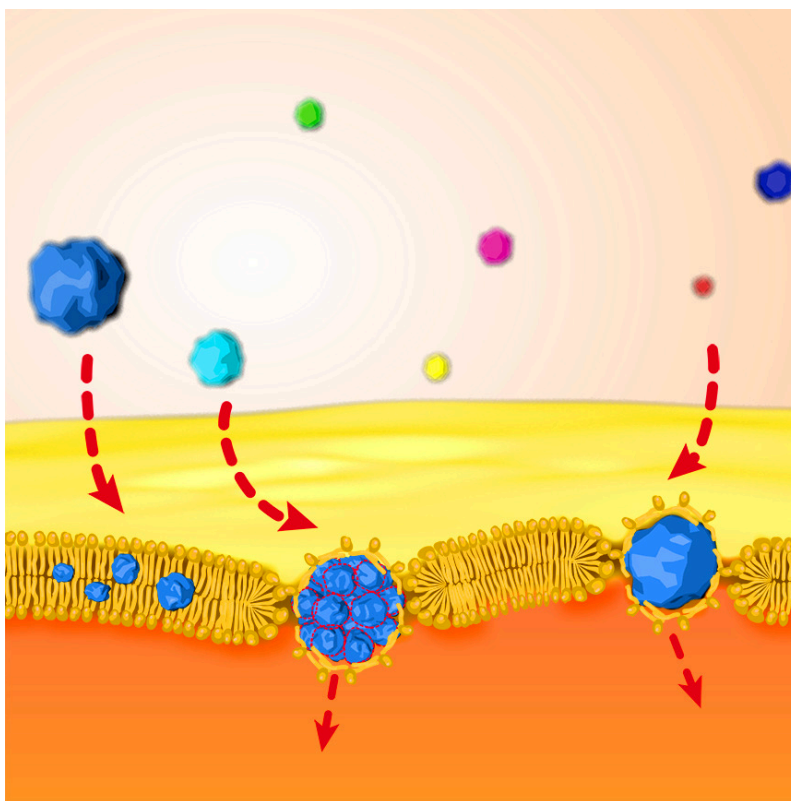
FIG. 1. **Suggested translocation mechanism of hydrophobic NPs** through lipid bilayer shown schematically. Small hydrophobic NPs are always trapped in the bilayer core while large superhydrophobic NPs and clusters of small superhydrphobic NPs get wrapped by a lipid layer. The wrapped objects destabilize the bilayer by generating pores and potentially pass through the bilayer.

mainly based on numerical simulations, proposed interesting strategies to enable these NPs to translocate.[2,29,30] These strategies are suggesting to manipulate the NP shapes,[29] the NP surface charges[2] or the NP coating by using peptides,[31] disposable ligands[30] or stripped nano-patterns with a controllable symmetry.[18,32–34] Some of these NP could be internalized into cell membrane, nevertheless none of them were shown to translocate experimentally through a simple phospholipid bilayer and the possible translocation pathway remained obscure.

In this work we demonstrate theoretically and experimentally the possibility of direct translocation of hydrophobic NPs and their aggregates through lipid bilayers, cf. Fig. 1. Using the Single Chain Mean Field (SCMF) theory[35–37] a mechanism of direct transloca-

4

tion through lipid bilayers is proposed. Observing individual translocation events of AuNPs covered with 1-dodecanethiol chains[38,39] through DMPC bilayers we confirm the particle translocation and characterize the kinetic pathway in agreement with our numerical predictions. The translocation mechanism relies on spontaneous pore formation in the lipid bilayer induced by insertion of superhydrophobic NPs. The observed universal interaction behavior of neutral and chemically inert NPs with bilayer can be classified according to size and surface properties. Due to size differences, small NPs are trapped in the cores of bilayers, while big clusters of NPs can translocate through lipid bilayers. These results might further suggest that the difference in cell reaction on different types of NPs may be similarly attributed to different universal interaction mechanisms with cell membranes.

II.   MECHANISM OF DIRECT TRANSLOCATION

The interaction between NPs with different sizes and a lipid bilayer was modeled using the Single Chain Mean Field (SCMF) theory for lipid bilayers.[37] Previously, this method was successfully applied to study the energy barrier during insertion of carbon nanotubes into lipid bilayer and small nano-objects into lipid bilayer.[40–42] A similar technique is used here to study the translocation of NPs through phospholipid bilayer. Details of the applied simulation setup are described in Section IV.

Nanoparticles are modeled as hydrophobic spheres[41] with diameters ranging from 2 to 10 nm. Oligomers grafted to the surface of NPs alter the surface chemistry and are modeled through their interaction with the phospholipid tails by an interaction parameter, ε. This interaction parameter is varied from -5.0 kT to -7.0 kT where a crossover between two regimes is observed. An interaction parameter $\varepsilon = -5.0$ kT corresponds to a weakly hydrophobic particle and represents relatively weak attraction between NP and bilayer while $\varepsilon = -7.0$ kT corresponds to a strong hydrophobic interaction and the NPs can be termed superhydrophobic.

The different insertion regimes found in simulations are presented in Fig. 2A) for different NP diameter and interaction parameter. When NPs with $\varepsilon = -5.0$ kT and -6.0 kT interact with lipid bilayer they insert into the core. The tails of the lipids are in direct contact with the NPs but the interaction is not strong enough to fully cover the surface of the NPs with lipids and to significantly disturb the bilayer structure. For diameters < 4 nm, a NP is

5

fully integrated into the bilayer and covered by continuous lipid leaflets. A deformation of the lipid bilayer is observed in the vicinity of a NP due to its hydrophobic interaction with the lipid tails. For large diameters, ranging from 6.0 to 10.0 nm, an inserted NP disrupts the bilayer creating a "hydrophobic pore"[43] while the tails of lipids are closely attached to the surface of the NP. In contrast, a strong hydrophobic interaction of $\varepsilon = -7.0$ kT, leads to structural rearrangement of lipids in the vicinity of a NP, wrapping a lipid monolayer around the entire surface of a NP. Due to the strong binding of lipids to the NP surface in this regime, the size of the NPs determines two possible scenarios of NP-bilayer interaction: (i) small NPs, with diameter ≤ 5 nm, can be fully inserted into the bilayer without significant disruption of the bilayer; (ii) large NPs, with diameter > 5 nm, do not fit into the core of the bilayer, and thus, their presence alter significantly the bilayer structure wrapping the NP with a lipid monolayer. Since the lipids are oriented towards the surface of the NPs, there is a possibility to form a "hydrophilic pore" of size slightly larger than the radius of the NP. This scenario is similar to experimentally reported pores in a bilayer due to inserted proteins.[43] The crossover between the two scenarios is controlled by the thickness of the bilayer, ~ 5 nm, which represents a characteristic length of the bilayer. This length determines the NP size when two possible solutions coexist simultaneously. Noteworthy, that if small NPs aggregate into clusters of larger size, they can behave similar as NPs with larger diameters. These possible scenario are indicated in Fig. 1.

To quantify the interaction of NPs with a bilayer, we calculated the free energy difference per lipid molecule for the equilibrium insertion of a NP, where ΔF^{40} is calculated with respect to the free energy of an unperturbed lipid bilayer without any NP. The free energy difference, ΔF, for different interaction parameters ε is plotted in Fig. 2B as a function of NP diameter. These calculations correspond to the thermodynamic equilibrium, thus there is no constrains on the distribution of lipids between NP and the bilayer, thus the number of lipids covering the NPs is the equilibrium coverage of NPs and the free energies correspond to the equilibrium. The more hydrophobic and the larger a NP, the more favorable its insertion into a bilayer. A lipid bilayer thus represents a potential well for hydrophobic NPs, and one could expect a NP, once trapped in the core of a bilayer, cannot escape spontaneously. In fact, we found that this is true for small NPs with diameter < 5 nm and for relatively weak attractions to lipid tails, when the topology of a lipid bilayer is not perturbed by the presence of NPs, cf. Fig. 2A.

6
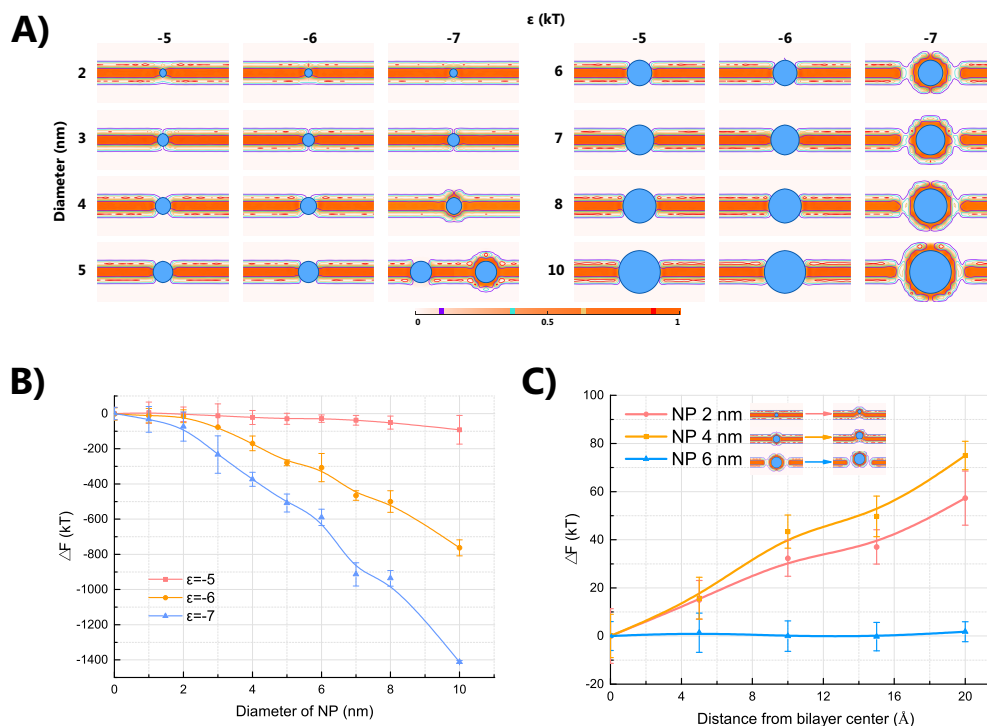
FIG. 2. **Interaction of hydrophobic NPs with lipid bilayers** obtained from SCMF theory. A) Density profiles of lipid heads and tails around embedded NPs. The NP diameter is varied between 2 nm $\leq D \leq$ 10 nm, the interaction parameter is varied between -5 kT $\geq \varepsilon \geq -7$ kT. B) Free energy difference ΔF as a function of the NP diameter for different interaction parameters ε. C) Free energy difference ΔF as function of the distance between the bilayer center and the core of a nanoparticle for $\varepsilon = -7$ kT.

However, in case of large NPs, with diameter > 5 nm, and strong attraction, $\varepsilon = -7$ kT, the structural rearrangement of lipid tails around NPs lead to a bilayer rupture with the formation of a hydrophilic pore. In this regime, the energy gain mainly results from covering the NPs with lipids, whereas the lipid-coated NPs are only weakly connected to the lipid bilayer.

To further explore this phenomenon, we calculated the free energy cost per lipid for a NP to escape from a bilayer, ΔF, which is defined as the energy cost of moving a NP out of the center of the bilayer in perpendicular direction. The result for $\varepsilon = -7$ kT is shown in Fig. 2C. Small NPs with diameters of 2.0 and 4.0 nm remain trapped in the bilayer and would

7

require large energies to be extracted from the bilayer since considerable deformation and rupture of the bilayer would be needed. In contrast, there is almost no free energy barrier to extract NPs with diameter of 6 nm from a bilayer. In consequence, superhydrophobic NPs $\geq$ 6 nm can escape from the bilayer by virtually pulling out lipids from the hole in the bilayer. The transition between an "closed" and "open" pore may be triggered by thermal motion with relatively small free energy cost.

Having found that large and strongly hydrophobic NPs with interaction parameter $\varepsilon = 7$ kT can leave a bilayer with negligible cost of energy, which can be easily overcome by thermal noise, we additionally explored the full translocation process across a bilayer for the interaction parameter of $\varepsilon = 7$ kT. This includes the insertion of a fully lipid-coated superhydrophobic NP into the bilayer, as present in the considered experimental realization. It turns out that the insertion of large hydrophobic NPs into a lipid bilayer is a multi-step process. The free energy difference as a function of the distance from the center of the bilayer is plotted in Fig. 3 with reference to an unperturbed bilayer and a NP in solution covered with lipids. First, lipid-coated NPs approach a bilayer and touch its surface. The deformation of the lipid bilayer without rearrangements of lipids leads to an increase of the free energy and is not taken into account. However, NPs in contact with the bilayer can spontaneously embed into a bilayer (Fig. 3, embedding regime); this process is energetically favorable and leads to a considerable decrease of the free energy. The transition between approaching and embedding is accompanied by a topological change in the structure of the bilayer and thus this transition is a first order transition, leading to an abrupt jump from one solution to another. Fully embedded NPs can then rearrange lipids and form pores with almost no energy cost and leave the bilayer as previously discussed. Note that the free energy values corresponding to escape regime in Fig. 3 (blue) is the same curve as Fig. 2C blue. The constant energy shift between the curves is due to the choice of the reference state of the free energy of a NP embedded in the center (Fig. 2) and the unperturbed bilayer with non-interacting NP (Fig. 3) .

8
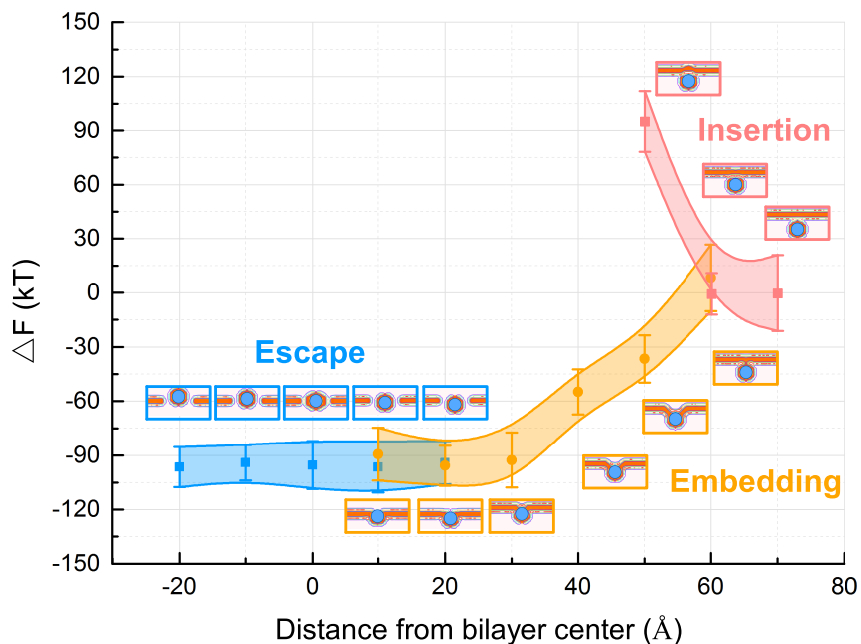
FIG. 3. **Interaction regimes during translocation** of superhydrophobic 6 nm NPs with $\varepsilon = -7.0$ kT given by three solutions of SCMF equations. (purple) Insertion: NP touches the upper leaflet without structural rearrangement; (yellow) Embedding: NP fuses with the upper leaflet and exchanges the lipids; (blue) Escape: NP formes a pore in the bilayer and is free to leave.

III.   EXPERIMENTAL STUDY OF A SINGLE PASSIVE TRANSLOCATION EVENT

A variant of the Droplet Interface Bilayer (DiB)[44,45] technique was used to produce a free standing lipid membrane in a microfluidic chip.[44,46,47] Using a volume controlled system with syringe pumps, two fingers of an aqueous phase (100 mM NaCl) were injected face-to-face into microchannels with a cross-geometry, cf. fig. 4A), which were previously filled with squalene containing a phospholipid mixture of 99% DMPC and 1% of fluorescent NBD-DPPE (see materials section IV). After a few seconds, the water-oil interface of each finger is covered with a monolayer of phospholipid molecules. Once two liquid fingers are brought in contact, the two lipid monolayers interact forming a lipid bilayer within a short time.[45,46] The bilayer is stable and can be analyzed simultaneously by optical microscopy and by electrophysiological experiments.[47] The capacitance of the formed particle free bilayer in this

geometry is measured as $C \approx 140$ pF for a pure DMPC bilayer, cf. fig. 5. Knowing the optically measured bilayer area, the specific capacitance can be calculated, $C_s \approx 4.46$ mF/m^2. From that, the corresponding bilayer thickness can be calculated as $d = \varepsilon_L \varepsilon_\circ / C_s \approx 4.4$ nm, where $\varepsilon_L = 2.2$ is the dielectric constant of the lipid membrane[45] and $\varepsilon_\circ = 8.85 \cdot 10^{-12}$ F/m is the vacuum permittivity. These estimates are in good agreement with literature values.[45–47] Monodisperse AuNPs of 2 nm, 4 nm and 6 nm diameter are rendered superhydrophobic by a covalent 1-dodecanethiol coating and are additionally covered with a DMPC monolayer to allow their dispersion in an aqueous phase (see methods section IV). These NPs can be added to either of the aqueous fingers.

For the first set of experiments, AuNPs, are dispensed in only one of the aqueous fingers at a concentration of ≈ 0.1 μg/ml sufficiently large for the NPs to form small clusters in solution. The other finger just contains buffer solution without any lipids or NPs. These two aqueous fingers in contact are just separated by a DMPC bilayer containing 1% of fluorescent lipids.

Once the DMPC bilayer was formed and equilibrated for 20–30 min, NPs of 2 nm diameter covered with DMPC were added into one of the aqueous fingers. After a few minutes a reduction of the capacitance is observed from $C \approx 140$ pF as observed for the pure bilayer to 127 pF for the same membrane area, cf. Fig. 5. The resulting effective bilayer thickness $d \approx 4.85$ nm is larger that of a pure lipid bilayer. The increased effective bilayer thickness indicates either insertion or accumulation of individual NPs in the bilayer. The capacitance signal is constant in time, similar to the pure bilayer, and excludes significant exchange of NPs or their clusters with the surrounding liquid. This suggests that the particles are either partially or completely inserted into the bilayer and are unable to escape. Repeating the same experiment with 4 nm and 6 nm AuNP's, the capacitance is further reduced with increasing particle size corresponding to an effective bilayer thickness of $d \approx 5.3$ nm and $d \approx 5.8$ nm, respectively. However, in case of the larger NPs, the capacitance signal fluctuates on the millisecond scale. This might result from direct contacts between lipid bilayer and AuNP's continuously trying to insert into and to escape from the bilayer.

The capacitance measurements discussed above were complemented by optical fluorescence measurements. The DMPC coated NPs initially added on one side of the bilayer are non-fluorescent and become visible by fluorescence microscopy only when taking up fluorescent lipids from the lipid bilayer. 20–30 min after adding lipid-coated NPs to only one
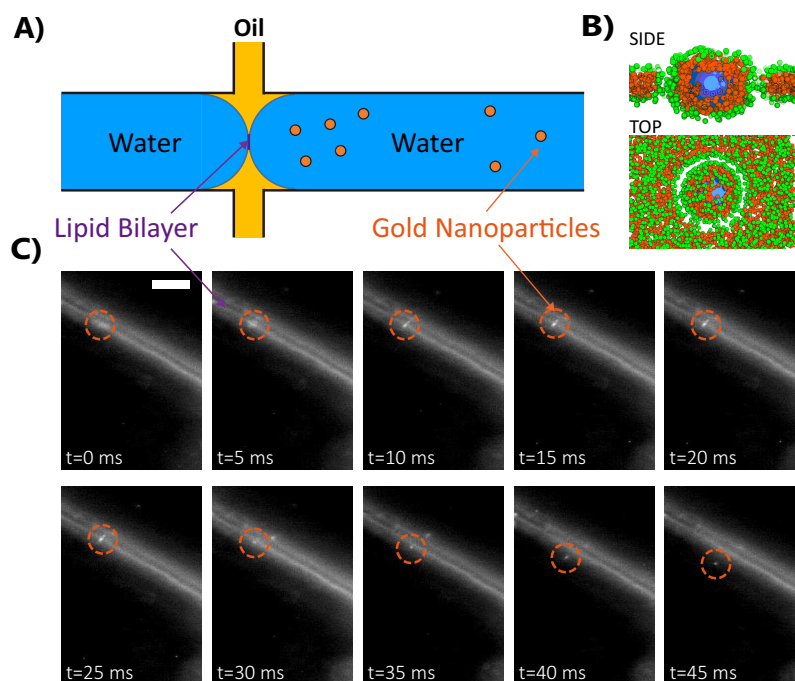
FIG. 4. **Microfluidic setup.** A) Two aqueous fingers surrounded by squalene-lipid solution form a bilayer at their contact area. Nanoparticles can be added to the aqueous phase of either of the aqueous fingers. B) Visualisation of most probable conformations of lipids around a pore formed by big hydrophobic NP, $D = 6.0$ nm and $\varepsilon = -7$ kT modelled within SCMF theory. C) Optical fluorescence microscopy time series demonstrating a single NP translocating through a lipid bilayer. AuNPs were added to the aqueous finger at the right. The NP leaving the bilayer (bright spot) to the initially particle free side of the bilayer is indicated by a dashed circle. Another NP leaving the membrane to the side of the bilayer, which initially contains NPs is visible from $t = 30$ ms.

side of the bilayer, we observe a similar number of fluorescent AuNP's on both sides of the lipid bilayer. Conducting the same type of experiments with non-fluorescing bilayer and NPs coated with fluorescent lipids, the presence of fluorescent lipids in the bilayer is observed 20–30 min after adding the NP's, cf. Supplemental Information (SI). This suggests that lipid-coated NPs can insert into the lipid bilayer and exchange lipid molecules with the bilayer. After insertion, the NPs can leave the bilayer to either side with equal probability, as predicted by the numerical results. From individual trajectories of NPs or clusters of NPs, the respective diffusion coefficient and the corresponding cluster or particle size can be
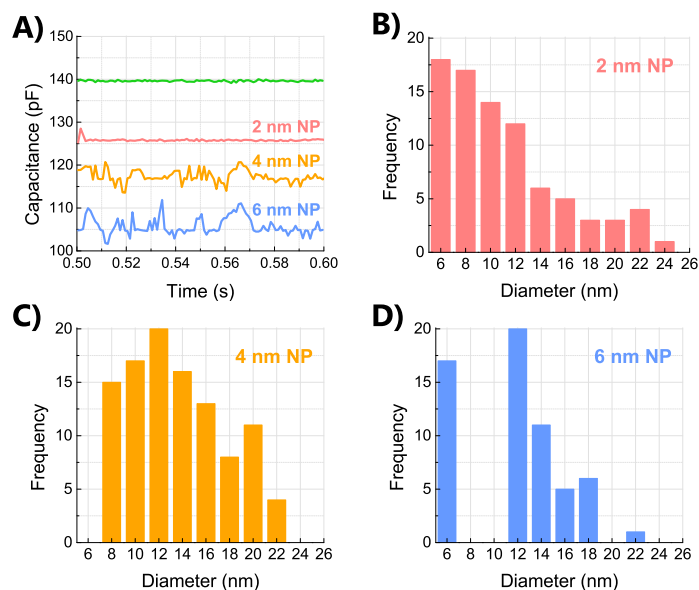
FIG. 5. **Experimental interaction of NPs with bilayer.** Measurements were performed for lipid coated AuNPs with diameter of 2 nm (rose), 4 nm (orange), and 6 nm (blue) at a concentration of $c \approx 0.1$ μg/ml. A) Capacitance measurements as function of time of a pure DMPC bilayer (green) and for DMPC bilayer in the presence of NPs dispersed in the aqueous phase. B)-D) Size distribution of NPs, respectively NP-cluster, that crossed the bilayer as analyzed from their Brownian motion. For the sake of clarity, the histograms are plotted as function of the particle core diameter without the 1-dodecanethiol and the DMPC coating.

estimated (conversion of diffusion coefficient to size, see SI). Using this strategy, we analyze the Brownian motion of lipid-coated NPs in the initially NP-free aqueous phase, *i.e.* the NPs that crossed the bilayer, see Fig. 5B-D. In case of 2 nm NPs no individual particles could be detected, and only clusters of NPs can cross the bilayer. The smallest cluster size that able to cross the bilayer had the diameter of 6 nm, while the largest particle diameter was 24 nm. A similar behavior was observed in case of 4 nm NPs, individual particles could not cross the bilayer and the smallest cluster able to cross the bilayer had the diameter of 8 nm. The largest cluster crossing the bilayer was 22 nm. The behavior observed for 6 nm NPs is remarkably different, for this particle size also individual particles could cross the bilayer, while the largest cluster crossing the bilayer was again 22 nm. The ability of lipid coated particles or clusters $d \geq 6$ nm to cross the bilayer, while smaller particles and

12
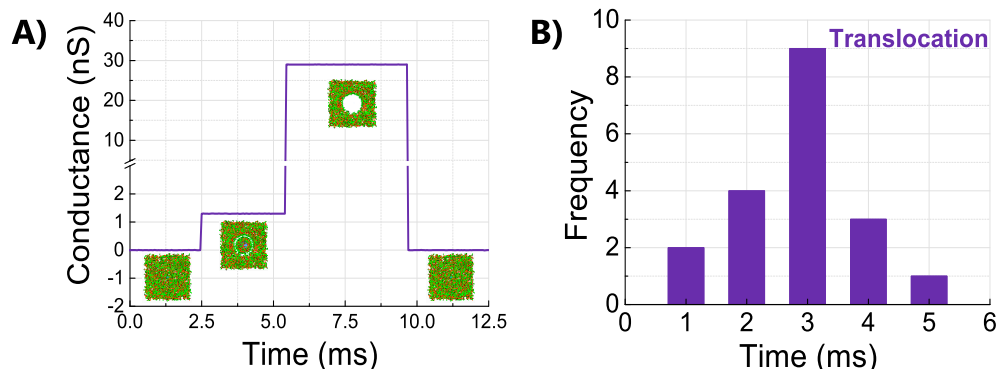
FIG. 6. **Kinetic Translocation pathway.** A) x of a translocation event from a 6 nm AuNP recorded at low particle concentration of $c \approx 0.01$ ng/ml. The insets represents the different stages of the translocation pathway as found by numerical simulation. B) Translocation times measured from several individual translocation events.

dye molecules (see SI) are unable to cross the bilayer, excludes spontaneous poration as the governing effect. Together with the previous electrophysiological results this clearly suggest passive translocation as the mechanism that allows NPs to cross the bilayer.

To also explore the pathway of the translocation, the experiments from above were repeated for 6 nm AuNP that can cross the bilayer as individual particles by the mechanism as suggested by simulations, Figure 4B). The experiments were conduced at an extremely low particle concentrations of 0.01 ng/ml making clustering of particles very unlikely, so the translocation of individual 6 nm AuNP can be observed. Moreover, due to the resulting low frequency of translocation events, a particle translocation observed by fluorescence microscopy can be unambiguously correlated to a simultaneously measured electrophysiological signal. Figure 4C) shows a single NP with 6 nm diameter leaving the bilayer to the initially NP free side; the size of the NP is confirmed by the Brownian motion analysis. The corresponding membrane conductance during the translocation is presented in Fig. 6A showing a three step process. Starting at $t = 0$, the membrane conductance G is equal to the control value, which confirms that the membrane is impermeable to ionic charges. At $t = 2.5$ ms, the conductance increases to $G = 1.3$ nS. At $t = 5.2$ ms (*i.e.* 2.7 ms later) a second jump in conductance is observed to $G \approx 30$ nS. At $t = 9.3$ ms (*i.e.* another 4.1 ms later) the conductance drops again down to the control value.

13

Let us interpret the conductance measurements of Fig. 6A in view of the numerical results that describe the entire translocation event as a three-steps process: insertion, embedding and escape, cf. Fig. 3. The insertion and embedding should not be seen with conductance measurements as no pores are associated to these steps. However, the previous fluorescence measurements showed a lipid exchange between a lipid-coated NP and a bilayer, demonstrating the insertion and embedding steps as predicted by the numerical results. Accordingly, the first jump can be understood as the formation of a hydrophilic pore being the first part of the escape process. The second jump corresponds to the particle leaving the pore, while the return of the conductance to the control value corresponds to the pore closure.

The formation of a hydrophilic pore results in a gap size d_g between the lipid coated NP and the bilayer and can be estimated as:

$$d_g \approx \frac{Gd}{2\pi k R_{NPL}} \approx 0.1 \, \text{nm} \tag{1}$$

where $k = 1.15$ S/m is the bulk electrolyte conductivity (measured for 100 mM NaCl at 30° C), $d \approx 4.4$ nm is the bilayer thickness and $R_{NPL} \approx 6$ nm is the radius of the used NPs with a core diameter of 6 nm functionalized with 1-dodecanethiol with length of 1.6 nm and a DMPC monolayer coating of ≈ 2.5 nm. The obtained gap size is in good agreement with the numerical model and large enough to allow NPs to escape the bilayer by thermal motion. The typical lifetime of the hydrophilic pore can be considered as translocation time and was found to be on the order of a few milliseconds, cf. Fig. 6B. We suppose that the gap is not uniform during its lifetime and thin lipid bridges might rather maintain the contact of the NP to the bilayer. This might explain that the process of lipid extraction and reorganization of the bilayer is not instant.

When the lipid-covered NP finally escapes the hydrophilic pore, the bilayer conductance is expected to increase massively and the experimentally measured conductance can be used to calculate the radius of the pore,

$$R_{NPL} = \sqrt{\frac{Gd}{k\pi}} \approx 6 \, \text{nm}. \tag{2}$$

This value is again in good agreement with the used NPs. The lifetime of such a open pore without particle is found to be also on the order of a few milliseconds. Surprisingly, the pore created during translocation does not lead to bilayer rupture, despite the fact that the transiently occurring pore is larger than the pore critical radius $R_c = \sigma/\Gamma \approx 1.2$ nm,

14

calculated from the membrane free energy. The membrane rupture is likely prevented by the short pore lifetime. Similarly, there are experimental measurements demonstrating non-destructive presence of large NP clusters in vesicles.[28]

IV.   MATERIAL AND METHODS

Single Chain Mean Field (SCMF) theory:

The SCMF[40–42] can reproduce equilibrium and mechanical properties and free energies of self-assembled objects with different geometries and molecular structures. Phospholipids are modeled at a coarse-grained level within the three-beads model[37] which provides accurate equilibrium and mechanical properties of DMPC lipid bilayers. NPs are modeled as hard spheres fixed in the center of the bilayer. More precisely, a NP represents a spherical region in the simulation box which is not accessible for phospholipids. We assume that the sphere can interact with hydrophobic tails of phospholipids but lipids cannot go inside this region. The interaction parameter with NPs varies between $\varepsilon = -5.0, -6.0, -7.0$ kT, while the interaction range is fixed and equal to 8.1 Å. The lipid molecule is modeled as three freely joint spherical beads of equal radius 4.05 Å and connected by the stiff bond of 10 Å.[37] The beads interact through square well potentials: between two hydrophobic beads, $\varepsilon_{TT} = -2.1$ kT with the interaction range $r = 12.15$ Å; between one hydrophilic bead and implicit solvent, $\varepsilon_{HS} = -0.15$ kT with interaction range $r = 12.15$ Å. The solvent molecule is considered to be of the same radius as the spherical beads. The simulation box of size $300 \times 300 \times 150$ Å is divided into 2D cylindrical layers around the z-axis in the center of the simulation box. The conformational sampling of lipid molecules is 4 000 000 conformations.

To calculate the free energy we assume that the simulation box represents a part of an extensive system with a NP located inside the simulation box, where the rest of the extensive system is a continuous repetition of the NP perturbed membrane, used as a reference state for the free energy. This allows to calculate the free energy F of a large system from the calculation of the simulation box. It can be written as a sum of the free energy of the simulation box F_{box} and the free energy of the equilibrium system out of the box F_{out}. If we assume there is no NP inside the simulation box as a reference state, F can be denoted through the total volume V and the total number of lipids N of the large system, the free energy per lipid of the bilayer, f_A, and the free energy of pure solvent, $f_s = (\phi_0/V_{sol}) \ln(\phi_0/V_{sol})$, where

15

V_s is the volume of the solvent and ϕ_0 is the bulk solvent volume fraction.

$$F = F_{box} + F_{out} = V f_s + N f_A \tag{3}$$

The free energy per lipid difference due to the insertion of a NP (Fig. 2C) yields the form

$$\Delta F = F_{box} - N f_A - (V_{box} - V_{obj}) f_s \tag{4}$$

where N is the equilibrium number of lipids in the box, V_{box} is the volume of the box, and V_{obj} in is the part of the NP inside the box.

Lipid Molecules and Solutions: All phospholipid molecules were purchased from Avanti Polar Lipids. To prepare the lipid solutions, 20 mg of DMPC (1,2-ditetradecanoyl-sn-glycero-3-phosphocholine) were dissolved in 1 ml Squalene (Sigma) with 1% NBD fluorescent labelled lipids (DPPE-NBD, 1,2-dimyristoyl-sn-glycero-3-phosphoethanolamine-N-(7-nitro-2-1,3-benzoxadiazol-4-yl) (ammonium salt)). The electrolyte for electrophysiological measurements consist of 100 mM solution of NaCl (Sigma-Aldrich) in Milli-Q water. All experiments were conducted at 30° C, where the lipid bilayer is in a fluid phase.

Microfluidics: Microchannels with rectangular cross section were fabricated using typical soft lithography protocols. Channel dimensions were 300 μm in width and 140 μm in height. The device was mold in Sylgard 184 (Dow Corning, USA) from a SU-8 photoresist structure on a silicon wafer. The surface of the Sylgard 184 devices was exposed to oxygen plasma (Diener electronic GmbH, Germany) and sealed with a plasma treated glass cover slide. The sealed device was rendered hydrophilic by heating it to 135° C over night. The liquids were dispensed from syringes (Hamilton Bonaduz AG, Switzerland), which were connected to the microuidic device by Teon tubing. Custom made computer controlled syringe pumps were used to control the injection of the water and the oil phase, respectively. For the fluorescent microscopy experiments a commercial micro-PIV setup from LaVision (Germany) was used with an illumination wavelength of 473 nm and a sensitive CCD-camera (Imager proX).

Patch Clamping: Ag/AgCl electrodes were prepared by inserting a silver chloride wire in a borosilicate glass pipette (outer diameter 1.5 mm, inner diameter 0.86 mm, Vendor) containing an electrolyte agarose solution. Lipid membrane capacitance was measured using the Lock-In function provided by the patch clamp amplifier EPC 10 USB (Heka-Electronics). A 10 mV sinusoidal wave with a frequency of 20 kHz was used as excitation signal. The

16

electrodes are carefully introduced into the aqueous compartment of the Sylgard 184 device using a micromanipulator.

Nanoparticles: NPs were synthesized from the one-step process described by N. Zheng *et al.*[48] They were characterized by standard methods and a transmission electron microscopy analysis and showed a size dispersion around ± 0.5 nm for the used NPs with average diameters of 2, 4 and 6 nm. To disperse these particles in an aqueous phase, we added a mixture of NPs and DMPC lipids on top of the aqueous phase. Subsequently, the system is sonicated for a few days. The formation of a stable dispersion of single NPs into the aqueous phase was confirmed by a Dynamic Light Scattering analysis.

V.   CONCLUSIONS

In a combined numerical and experimental study using the Single Chain Mean Field theory and a microfluidic approach we investigated a process of passive translocation of single superhydrophobic AuNPs through a lipid bilayer. It was found that the interaction of NPs with the lipid bilayer depends on the size of NPs. We could clearly identify the translocation of single NPs with diameters $d > 5$ nm, while individual NPs with $d < 5$ nm are trapped in the bilayer. These small NPs can leave the bilayer only when forming clusters exceeding 5 nm. This threshold particle size of 5 nm is comparable to the thickness of a bilayer and thus denotes the crossover between the permanent insertion of nanoparticles in the lipid bilayer and passive translocation.

The translocation pathway numerically predicted by the Single Chain Mean Field theory could be clarified studying single translocation events time resolved by optical fluorescence and electrophysiological measurements in a microfluidic setting. After the insertion of a superhydrophobic NP into a bilayer, the lipid molecules reorganize and flip their tails towards the NP completely wrapping the NP. Such a lipid wrapped NP is only weakly bound to the lipid bilayer and forms a spontaneous pore that can open with thermal energies enabling passive translocation of NPs. The measured lifetime of such a spontaneous pore during translocation was found to be on the order of very few milliseconds and closes again without rupturing the bilayer. During the insertion process of a lipid coated NP into the bilayer, the NP inserts at least parts of its lipid coating into the bilayer and in turn extracts lipid molecules from the bilayer during a translocation event, similar to the reported lipid

17

extraction by graphene nano-sheets.[49]

The observed and described mechanism allows for translocation of homogeneously coated NPs without the need of any nano-patterning, as reported in Refs. 17,18. The simplicity of the mechanism suggest its universality, similarly valid also for other types of hydrophobic NPs which may play an important role in numerous physiological processes and biomedical applications like membrane binding capacity, cytotoxicity, uptake efficiency, activation of an immune reaction. The presented experimental approach allows to explore the cytotoxic properties of a single NP while measuring if a pore formation is associated with a translocation process.

Furthermore, understanding this phenomenon can shed light on several biologically and environmentally relevant questions, such as dangers related to uptake of tiny hydrophobic NPs by aquatic animals and potential harm of NPs present in cosmetics and skin creams.

---

[*] jean-baptiste.fleury@physik.uni-saarland.de

[†] vladimir.baulin@urv.cat

[1] Mailänder, V. & Landfester, K. Interaction of Nanoparticles with Cells. *Biomacromolecules* **10**, 2379–2400 (2009).

[2] Lin, J., Zhang, H., Chen, Z. & Zheng, Y. Penetration of Lipid Membranes by Gold Nanoparticles: Insights into Cellular Uptake, Cytotoxicity, and Their Relationship. *ACS Nano* **4**, 5421–5429 (2010).

[3] Schatten, H. *Scanning Electron Microscopy for the Life Sciences* (Cambridge University Press, 2012).

[4] Korzeniowska, B., Nooney, R., Wencel, D. & McDonagh, C. Silica nanoparticles for cell imaging and intracellular sensing. *Nanotechnology* **24**, 442002 (2013).

[5] Pan, Y., Du, X., Zhao, F. & Xu, B. Magnetic nanoparticles for the manipulation of proteins and cells. *Chemical Society Reviews* **41**, 2912–2942 (2012).

[6] Varadan, V. K., Chen, L. & Xie, J. *Nanomedicine: Design and Applications of Magnetic Nanomaterials, Nanosensors and Nanosystems* (John Wiley & Sons, 2008).

[7] Choi, J. & Sun, N. Nanoparticles in Biomedical Applications and Their Safety Concerns. In Fazel, R. (ed.) *Biomedical Engineering - From Theory to Applications* (InTech, 2011).

18

[8] Prasad, G. L. Biomedical Applications of Nanoparticles. In Webster, T. J. (ed.) *Safety of Nanoparticles*, Nanostructure Science and Technology, 89–109 (Springer New York, 2009).

[9] Li, Y. *et al.* A smart and versatile theranostic nanomedicine platform based on nanoporphyrin. *Nature Communications* **5** (2014).

[10] Kang, J. H. *et al.* An extracorporeal blood-cleansing device for sepsis therapy. *Nature Medicine* **20**, 1211–1216 (2014).

[11] Johnston, H. J. *et al.* A review of the in vivo and in vitro toxicity of silver and gold particulates: Particle attributes and biological mechanisms responsible for the observed toxicity. *Critical Reviews in Toxicology* **40**, 328–346 (2010).

[12] Freese, C. *et al.* Uptake and cytotoxicity of citrate-coated gold nanospheres: Comparative studies on human endothelial and epithelial cells. *Particle and Fibre Toxicology* **9**, 23 (2012).

[13] Alkilany, A. M. & Murphy, C. J. Toxicity and cellular uptake of gold nanoparticles: what we have learned so far? *Journal of Nanoparticle Research* **12**, 2313–2333 (2010).

[14] Paino, I. M. M., Marangoni, V. S., de Oliveira, R. d. C. S., Antunes, L. M. G. & Zucolotto, V. Cyto and genotoxicity of gold nanoparticles in human hepatocellular carcinoma and peripheral blood mononuclear cells. *Toxicology Letters* **215**, 119–125 (2012).

[15] Coradeghini, R. *et al.* Size-dependent toxicity and cell interaction mechanisms of gold nanoparticles on mouse fibroblasts. *Toxicology Letters* **217**, 205–216 (2013).

[16] Shang, L., Nienhaus, K. & Nienhaus, G. U. Engineered nanoparticles interacting with cells: size matters. *Journal of Nanobiotechnology* **12**, 5 (2014).

[17] Verma, A. *et al.* Surface-structure-regulated cell-membrane penetration by monolayer-protected nanoparticles. *Nature Materials* **7**, 588–595 (2008).

[18] Verma, A. & Stellacci, F. Effect of Surface Properties on Nanoparticle–Cell Interactions. *Small* **6**, 12–21 (2010).

[19] Chu, Z. *et al.* Unambiguous observation of shape effects on cellular fate of nanoparticles. *Scientific Reports* **4** (2014).

[20] Moyano, D. F. *et al.* Nanoparticle Hydrophobicity Dictates Immune Response. *Journal of the American Chemical Society* **134**, 3965–3967 (2012).

[21] Doherty, G. J. & McMahon, H. T. Mechanisms of Endocytosis. *Annual Review of Biochemistry* **78**, 857–902 (2009).

[22] McMahon, H. T. & Boucrot, E. Molecular mechanism and physiological functions of clathrin-

19

mediated endocytosis. *Nature Reviews Molecular Cell Biology* **12**, 517–533 (2011).

[23] Liu, J., Sun, Y., Drubin, D. G. & Oster, G. F. The Mechanochemistry of Endocytosis. *PLoS Biol* **7**, e1000204 (2009).

[24] Orsi, M. & Essex, J. W. Permeability of drugs and hormones through a lipid bilayer: insights from dual-resolution molecular dynamics. *Soft Matter* **6**, 3797 (2010).

[25] Paula, S., Volkov, A. G., Van Hoek, A. N., Haines, T. H. & Deamer, D. W. Permeation of protons, potassium ions, and small polar molecules through phospholipid bilayers as a function of membrane thickness. *Biophysical Journal* **70**, 339–348 (1996).

[26] Bedrov, D., Smith, G. D., Davande, H. & Li, L. Passive Transport of C60 Fullerenes through a Lipid Membrane: A Molecular Dynamics Simulation Study. *J. Phys. Chem. B* **112**, 2078–2084 (2008).

[27] Qiao, R., Roberts, A. P., Mount, A. S., Klaine, S. J. & Ke, P. C. Translocation of C60 and Its Derivatives Across a Lipid Bilayer. *Nano Lett.* **7**, 614–619 (2007).

[28] Bonnaud, C. *et al.* Insertion of Nanoparticle Clusters into Vesicle Bilayers. *ACS Nano* **8**, 3451–3460 (2014).

[29] Yang, K. & Ma, Y.-Q. Computer simulation of the translocation of nanoparticles with different shapes across a lipid bilayer. *Nature Nanotech.* **5**, 579–583 (2010).

[30] Ding, H.-m., Tian, W.-d. & Ma, Y.-q. Designing Nanoparticle Translocation through Membranes by Computer Simulations. *ACS Nano* **6**, 1230–1238 (2012).

[31] Davies, A., Lewis, D. J., Watson, S. P., Thomas, S. G. & Pikramenou, Z. pH-controlled delivery of luminescent europium coated nanoparticles into platelets. *Proceedings of the National Academy of Sciences* **109**, 1862–1867 (2012).

[32] Van Lehn, R. C. *et al.* Effect of Particle Diameter and Surface Composition on the Spontaneous Fusion of Monolayer-Protected Gold Nanoparticles with Lipid Bilayers. *Nano Letters* **13**, 4060–4067 (2013).

[33] Van Lehn, R. C. *et al.* Lipid tail protrusions mediate the insertion of nanoparticles into model cell membranes. *Nature Communications* **5** (2014).

[34] Li, Y., Li, X., Li, Z. & Gao, H. Surface-structure-regulated penetration of nanoparticles across a cell membrane. *Nanoscale* **4**, 3768–3775 (2012).

[35] Ben-Shaul, A., Szleifer, I. & Gelbart, W. M. Chain organization and thermodynamics in micelles and bilayers. i. theory. *J. Chem. Phys.* **83**, 3597–3611 (1985).

20

[36] Ben-Shaul, A., Szleifer, I. & Gelbart, W. M. Chain statistics in micelles and bilayers: Effects of surface roughness and internal energy. *J. Chem. Phys.* **85**, 5345–5359 (1986).

[37] Pogodin, S. & Baulin, V. A. Coarse-Grained Models of Phospholipid Membranes within the Single Chain Mean Field Theory. *Soft Matter* **6**, 2216–2226 (2010).

[38] Carré, A. & Mittal, K. L. (eds.) *Superhydrophobic surfaces* (VSP, Leiden ; Boston, 2009).

[39] Decher, G. & Schlenoff, J. B. (eds.) *Multilayer thin films: sequential assembly of nanocomposite materials* (Wiley-VCH, Weinheim, 2012), 2nd, compl. rev. and enl. ed edn.

[40] Pogodin, S. & Baulin, V. A. Can a carbon nanotube pierce through a phospholipid bilayer? *ACS Nano* **4**, 5293–5300 (2010).

[41] Pogodin, S. & Baulin, V. Equilibrium Insertion of Nanoscale Objects into Phospholipid Bilayers. *Current Nanoscience* **7**, 721–726 (2011).

[42] Pogodin, S., Slater, N. K. H. & Baulin, V. A. Surface patterning of carbon nanotubes can enhance their penetration through a phospholipid bilayer. *ACS Nano* **5**, 1141–1146 (2011).

[43] Mosgaard, L. D. & Heimburg, T. Lipid Ion Channels and the Role of Proteins. *Accounts of Chemical Research* **46**, 2966–2976 (2013).

[44] Funakoshi, K., Suzuki, H. & Takeuchi, S. Lipid Bilayer Formation by Contacting Monolayers in a Microfluidic Device for Membrane Protein Analysis. *Analytical Chemistry* **78**, 8169–8174 (2006).

[45] Bayley, H. *et al.* Droplet interface bilayers. *Molecular BioSystems* **4**, 1191–1208 (2008).

[46] Thutupalli, S., Fleury, J.-B., Steinberger, A., Herminghaus, S. & Seemann, R. Why can artificial membranes be fabricated so rapidly in microfluidics? *Chemical Communications* **49**, 1443–1445 (2013).

[47] Vargas, J. N., Seemann, R. & Fleury, J.-B. Fast membrane hemifusion via dewetting between lipid bilayers. *Soft Matter* **10**, 9293–9299 (2014).

[48] Zheng, N., Fan, J. & Stucky, G. D. One-Step One-Phase Synthesis of Monodisperse Noble-Metallic Nanoparticles and Their Colloidal Crystals. *Journal of the American Chemical Society* **128**, 6550–6551 (2006).

[49] Tu, Y. *et al.* Destructive extraction of phospholipids from Escherichia coli membranes by graphene nanosheets. *Nature Nanotechnology* **8**, 594–601 (2013).

4

GENERAL MODEL OF PEROXIDISED PHOSPHOLIPID WITHIN MD SIMULATIONS
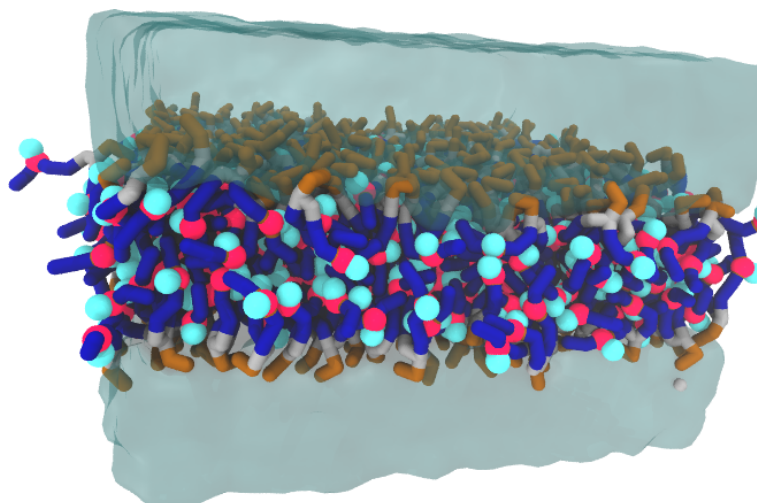
Soft Matter

PAPER

Peroxidised phospholipid bilayers: insight from coarse-grained molecular dynamics simulations

Yachong Guo,[a] Vladimir A. Baulin[a] and Fabrice Thalmann*[b]

An original coarse-grained model for peroxidised phospholipids is presented, based on the MARTINI lipid force field. This model results from a combination of thermodynamic modelling and structural information on the area per lipid, which have been made available recently. The resulting coarse-grained lipid molecules form stable bilayers, and a set of elastic coefficients (compressibility and bending moduli) is obtained. We compare the compressibility coefficient to the experimental values [Weber *et al.*, *Soft Matter*, 2014, **10**, 4241]. Predictions for the mechanical properties, membrane thickness and lateral distribution of hydroperoxide groups in the phospholipid bilayer are presented.

1 Introduction

Oxidative stress[1] plays an important role in regulating vital processes in living organisms: defense against bacteria, cell apoptosis, immune response, cell maturation and differentiation. Free radicals or reactive oxygen species (ROS)[1] may react chemically with cell constituents, leading to irreversible damage. The first line of defense of cells is the cell membrane[2] where lipids, proteins, cholesterol, vitamins and fatty acids first interact with the external environment of the cell.

It is generally accepted[3,4] that the protection of cell membranes from oxidation stress is due to the incorporation of molecules containing weak chemical bonds (anti-oxidants): vitamins, unsaturated fatty acids, and unsaturated lipids that can break and deactivate free radicals. In particular, oxygen radicals damage the weak double bond in the tails of unsaturated lipids and fatty acids, provoking changes in their conformations and disturbing the bilayer. A balanced amount of free radicals and anti-oxidants is essential for normal function of living organisms.[5] However, when this balance is altered, it can lead to a series of diseases ranging from cancer and diabetes to several ageing diseases[6] such as Parkinson and Alzheimer diseases.

Lipid peroxidation is a major consequence of oxidative damage to cell membranes due to various external factors[1,3] such as reactive oxygen species (ROS), inflammation, catalysis by peroxisomal oxidases, virus phagocytosis, and ultraviolet and ionic irradiation. Photooxidation of giant lipid vesicles allows quantification of the effect of oxidation on lipid bilayers.[7–11] In particular, with a careful choice of photosensitizer, it becomes possible to generate specifically lipid peroxides.[9] This approach allows control of the rate of oxidation and the total area of the vesicle, providing information on the rigidity of the lipid bilayer and the variation of the area per lipid with the degree of oxidation.

In turn, lipid bilayer structure modifications due to oxidised lipids can be directly assessed using all-atom molecular dynamics (MD) simulations,[12] including peroxidised poly-unsaturated lipids.[13–15] The coarse-grained (CG) model of oxidised species[16] and single chain mean field (SCMF) approaches have been introduced only recently.[9,17] According to these simulations, the increase of area per lipid, the decrease of bilayer thickness and the shift of the peroxidised group towards the surface of the bilayer are general manifestations of oxidation.

In this paper we introduce a coarse-grained molecular model of hydroperoxidised lipids based on recent experimental data.[9,11] Using this model we evaluate the effect of peroxidation on the thermodynamic and mechanical properties of fully peroxidised lipid bilayers.

Coarse-grained models have been widely used to describe the structure and dynamic properties of lipid bilayers, providing good pictures of the self-assembly of lipid bilayers and collective phenomena.[18] One of the most widely employed coarse-grained models of lipid bilayers for molecular dynamics simulations is the MARTINI force field,[19] which gives realistic structure and elastic properties of lipid bilayers. Thus, we use this model as a starting point for peroxidised phospholipid molecules.

2 Coarse-grained models of hydroperoxidised lipids

We construct oxidised lipid models based on the original MARTINI models[19] for 1-palmitoyl-2-oleoyl-*sn-glycero*-3-phosphocholine

[a] *Departament d'Enginyeria Quimica, Universitat Rovira i Virgili 26 Av. dels Paisos Catalans, 43007 Tarragona, Spain*

[b] *Institut Charles Sadron, CNRS and University of Strasbourg, 23 rue du Loess, F-67034 Strasbourg, France. E-mail: thalmann@ics.u-strasbg.fr; Fax: +33 388414099; Tel: +33 388414097*
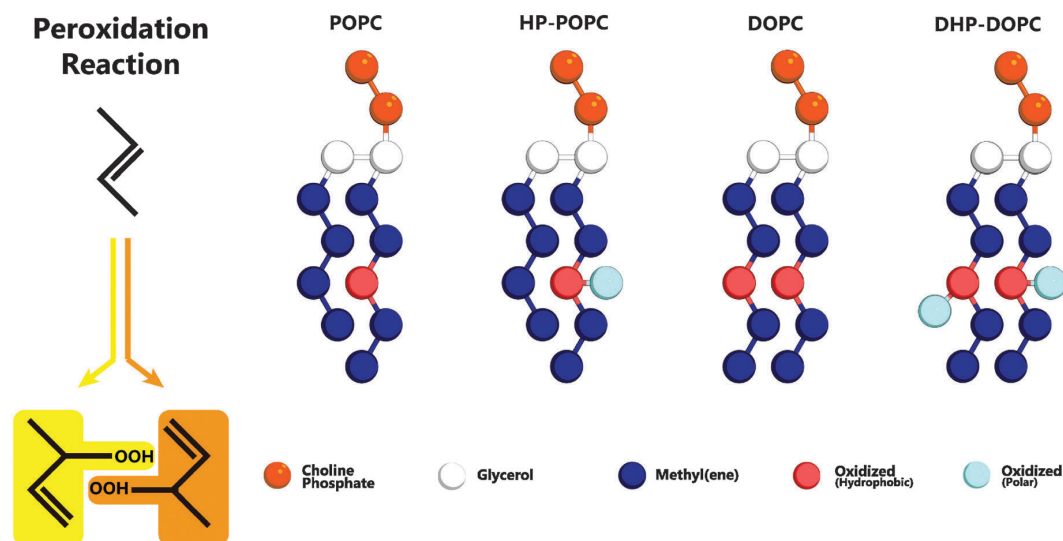
Fig. 1 Left: addition of reactive singlet oxygen to a chain unsaturation. Right: oxidised lipid molecules based on MARTINI coarse-grained models for POPC and DOPC phospholipids: HP-POPC and DHP-DOPC, respectively. Bead types without exception are already present in the MARTINI model,[19] without change in the mutual interaction parameters.

(POPC) and 1,2-dioleoyl-*sn-glycero*-3-phosphocholine (DOPC) phospholipid molecules. We assume that hydroperoxidation acts on the double bond in the tail, C=C, resulting in a shift of its position and the addition of a side –OOH group. Further oxidation damage to lipids may cause chain cleavage and severe lipid degradation, which we do not consider in the present study.

The MARTINI coarse-graining strategy is based on a 4 atom to 1 bead correspondence,[19] with effective potentials between beads accounting for the thermodynamic mixing properties of the underlying molecular sub-groups. Hydroperoxidation has the effect of adding two oxygens atoms to an existing group of 4 carbons (Fig. 1) as a result of so-called Type II photooxidation reactions.[22,23] The CG model must therefore account for 6 atoms with amphipathic properties.

We consider that the two peroxidised products are indistinguishable at the coarse-grained level adopted here, and assume that both can be suitably represented by a single assembly of beads with average properties. The hydrophobic part retains an unsaturated C=C bond, as in the original target. The hydrophilic part OOH is without doubt a polar group with donor and acceptor hydrogen bonding character. The 6 atom group C_4OOH is bulkier than the original unoxidised group C_4. One could imagine introducing for that a larger bead, but it would then be necessary to reimplement all the pairwise Lennard-Jones interactions with the other existing coarse-grained beads. Then, a bead of intermediate polarity can only poorly reproduce the two-sided (hydrophobic-polar) character of C_4OOH. In contrast, a set of two beads (dimer) can optimally traduce the intrinsic amphipathy of the group. By adjusting the separation between beads, as in the case of the glycerol backbone, the bulkiness of the pair can be set to a reasonable value, 50% higher than the original C_4 group (6 atoms instead of 4).

Our systematic investigations lead us to the conclusion that an optimal choice is the adjunction of a MARTINI C3 (hydrophobic) bead to a MARTINI P2 (polar, H-bonding donor and acceptor) bead, separated by 0.33 nm, smaller than the standard lipid bonding distance (0.47 nm). Note that the structural properties of the resulting bilayer depend quite sensitively on this separation. This choice, as explained in Section 4, comes from a comparison with the experimental change in area per lipid resulting from the complete hydroperoxidation of the unsaturated pure POPC and DOPC lipid bilayers. The average increase in area per lipid following complete peroxidation is reported to be +15.6% for POPC bilayers, and +19.1% for DOPC bilayers, respectively.[9] Similar area changes were also obtained by monitoring giant vesicles adhering onto specially prepared adhesive surfaces,[11] then leading to relative area changes of +14.3% and +18.4% for oxidised POPC and DOPC vesicles, respectively. These values are fairly consistent, given the practical difficulties inherent to these experimental techniques. This combination of results puts stringent constraint on the CG candidate models.

Mapping to this structural quantity, however, is no substitute for performing a thermodynamic mixing assay of the C_4OOH target group. For this purpose, knowing the chemical structure of the oxidised lipid, we selected *tert*-butyl hydroperoxide (TBHP, CAS 75-91-2, a commercial bleaching agent)[24] as the best analogue to the peroxidised functional group C_4O_2. The values of water solubility and octanol/water partitioning $\log P_{ow}$ data of TBHP that we could find are scattered between 0.6 and 1.23, while simulations of the C3–P2 dimer alone suggest a numerical, coarse-grained $\log P_{ow} = 1.4$. Finally, the acidic constant of TBHP, $pK_a = 12.8$, suggests a predominantly protonated, neutral hydroperoxide group, for neutral or slightly acidic pH solutions.

Soft Matter   **Paper**
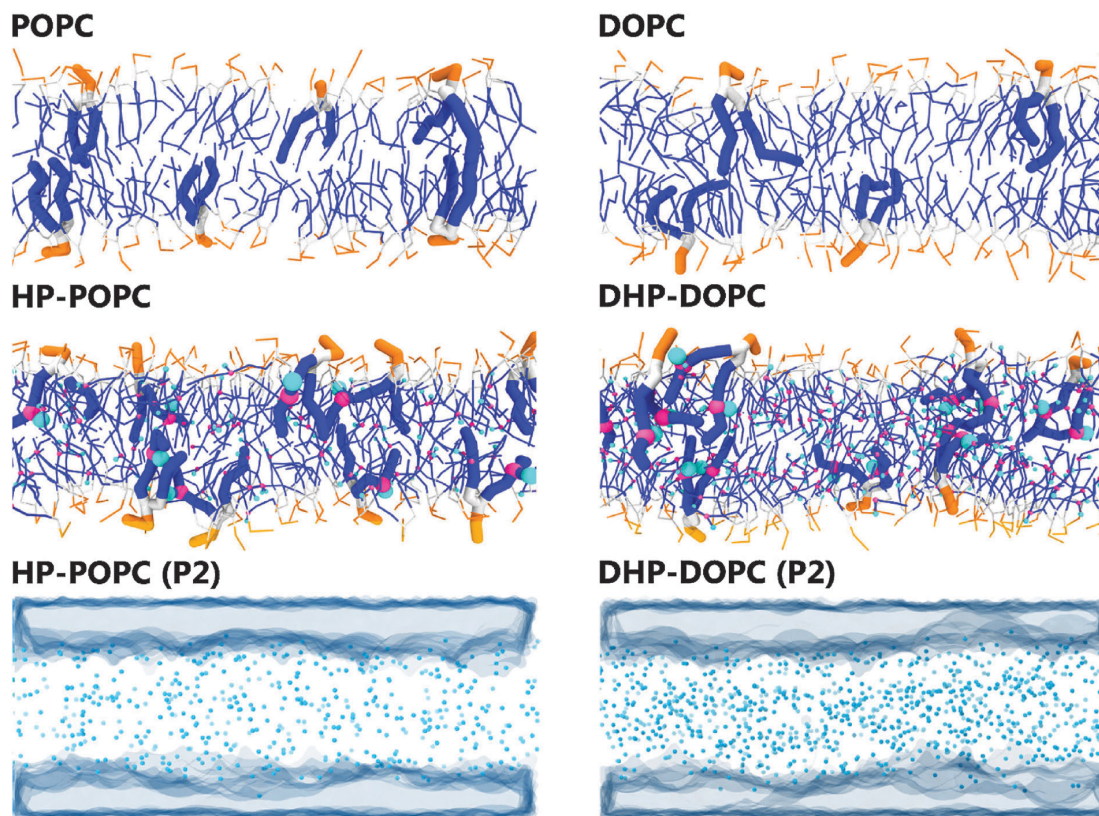
Fig. 2 Snapshots of the 512 lipid samples: top and middle rows. Distribution of the polar oxidised beads and water regions in HP-POPC bilayers (bottom left) and DHP-DOPC (bottom right).

In what follows, we designate by HP-POPC the hydroperoxidised POPC molecule, and by DHP-DOPC the doubly hydroperoxidised DOPC (Fig. 1). We find that bilayers formed with pure HP-POPC and DHP-DOPC are stable, and provide a set of numerically estimated structural and mechanical parameters, associated with these two lipid bilayers. Snapshots of bilayers formed with POPC, DOPC, HP-POPC and DHP-POPC are provided in Fig. 2.

3 Results and discussion

3.1 Structural changes upon peroxidation

Pure HP-POPC and DHP-DOPC bilayers appear to be numerically stable and lend themselves to the determination of fairly precise structural properties. The main structural data are summarized in Table 1. The area per lipid was used to set up CG models.

Assuming that these values are correct, resulting CG models provide a quantitative estimate of membrane thickness and membrane specific volume changes due to peroxidation. If one assumes that membranes are quasi-incompressible media, the volume change is entirely due to the added hydroperoxide groups, and it becomes possible to split the increase in area per lipid into two contributions: homogeneous increase and structural reorganisation. The homogeneous increase of area is directly proportional to the relative volume change $(\Delta A/A)_{\text{hom}} = 2/3(\Delta V/V_{\text{b}})$, as if the bilayer was an homogeneous fluid with volume V_{b}. The second contribution is due to the membrane reorganisation due to changes in chemical affinity and polarity following the addition of the hydroperoxide groups. The corresponding "structural" relative increase of area is $(\Delta A/A)_{\text{str}} = \Delta A/A - (\Delta A/A)_{\text{hom}}$.

Lipids were simulated in a box with lateral x,y directions and the transverse z direction, at a temperature of 300 K. An anisotropic Parinello-Rahman barostat was applied to simulate a tensionless bilayer (all three directions being subject to a 1 bar compressive stress), and the average lateral size $L_x = L_y$ of the system provides the desired bilayer area $A = \langle L_x L_y \rangle$. Changes in the membrane volume and the membrane thickness upon peroxidation are obtained by monitoring the changes in the average simulation box volume $\langle L_x{}^2 L_z \rangle$ and extension $\langle L_z \rangle$.

Table 1 Simulation box properties for symmetric bilayers with 512 lipids and 3072 CG water beads, at 1 bar and 300 K

Lipid	Box area (nm²)	Box thickness (nm)	Box volume (nm³)
POPC	163.9 ± 0.2	6.551 ± 0.004	1072.04 ± 0.04
HP-POPC	190.8 ± 0.3	5.821 ± 0.006	1110.63 ± 0.04
DOPC	171.48 ± 0.13	6.576 ± 0.005	1127.67 ± 0.04
DHP-DOPC	204.92 ± 0.4	5.87 ± 0.02	1203.55 ± 0.05

Table 2 Equilibrium bilayer thickness, area, volume, area per lipid and volume per lipid of POPC and DOPC phospholipids, and corresponding oxidised analogs HP-POPC and DHP-DOPC (512 lipids systems)

	POPC	HP-POPC	DOPC	DHP-DOPC
Thickness (nm)	4.318 ± 0.006	3.90 ± 0.01	4.442 ± 0.007	4.08 ± 0.03
Area (nm^2)	163.9 ± 0.02	190.8 ± 0.3	171.48 ± 0.13	204.9 ± 0.4
Volume (nm^3)	706.02 ± 0.08	744.61 ± 0.08	761.65 ± 0.08	837.53 ± 0.09
Area/lipid (nm^2)	0.6402 ± 0.0008	0.7453 ± 0.0012	0.6698 ± 0.0006	0.8005 ± 0.0016
Volume/lipid (nm^3)	1.3789 ± 0.0002	1.4542 ± 0.0002	1.4875 ± 0.0002	1.6357 ± 0.0002

The area of the simulation box and the area of the bilayer can be considered equal, as the excess area caused by undulations is small, especially for systems comprising only 512 lipids. There is however a significant difference between the volume and the thickness of the box compared with the volume and the thickness of the bilayer only. Let us denote by V_b and L_b the volume and the thickness of the bilayer, and by V and L_z the volume and the thickness of the simulation box mentioned in Table 1. The simplest way to relate V and V_b or L_z and L_b consists of removing the volume of the homogeneous solvent taken at the same pressure and temperature. The volume of the 3072 CG fluid water system is $V_s = 366.04 \pm 0.07$ nm^3. The bilayer volume and thickness follow from the expressions

$$V_b = V - V_s; \; L_b = L_z - \frac{V_b}{A}. \quad (1)$$

Such an approximation means that the change in the water structure in the vicinity of bilayers is disregarded, and is known as the Luzzati approximation.[25]

The resulting bilayer volumes and thicknesses are summarised in Table 2 below. Upon peroxidation, the volume change of the bilayer coincides with the volume change of the simulation box. Relative volume, thickness and area changes are summarised in Table 3. We notice in particular that the structural area variations $(\Delta A/A)_{str}$ are almost identical for both oxidised lipids. The higher density of hydroperoxide groups in DHP-DOPC compared with HP-POPC does not lead to an increase in area per lipid beyond a trivial change in bilayer volume V_b.

3.2 Hydroperoxide group distribution

The CG models give also a prediction for lateral density profiles, and in particular for the hydroperoxide group distribution. The partitioning of C$_4$OOH between the water interface and the inner hydrophobic region maintains a subtle statistical balance. On the one hand the group must show affinity for the interfacial water, on the other hand, the h-bonding donor and acceptor character promotes self-interaction.

The density distribution of an equilibrated coarse grained DHP-DOPC bilayer and HP-POPC bilayer is shown in Fig. 3.

Both density distributions were obtained from a simulation of a bilayer patch containing 512 DHP-DOPC/HP-POPC lipids at full hydration (6 CG water beads equivalent to 24 water molecules per lipid) at room temperature ($T = 300$ K) with the lateral and normal pressures independently coupled to a pressure of 1 bar. The local center of the bilayer was calculated and used in the present work to determine the density as follows: the xy plane of the simulation box was divided into 8×8 regions, and the local positions of the bilayer center were calculated as $\bar{z} = \langle z \rangle$, where the averaging was performed over all lipid monomers in the given region. This position was further used in binning the density profile to shift the bilayer center.
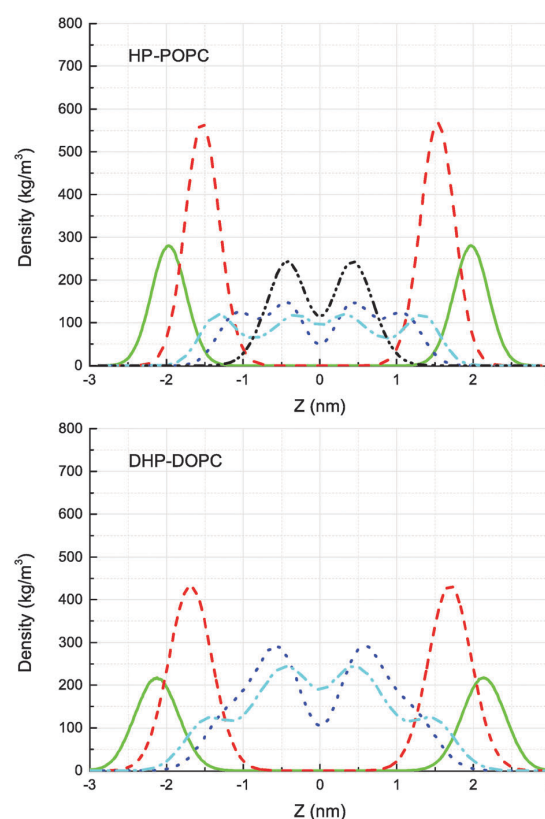
Fig. 3 Partial mass densities for HP-POPC (top) and DHP-DOPC (bottom) phosphate groups (green/full line), glycerol (red/dashed line), Hydrophobic Oxidised (blue/dotted line), Polar Oxidised (cyan/dash-dotted line), and 3rd hydrophobic group (C3A in the Martini model of POPC) of the opposite saturated tail of POPC (black/dash-dot-dotted line). The bilayer center lies at $z = 0$ nm.

Table 3 Relative structural changes of the bilayer following peroxidation of POPC and DOPC molecules. The last column represents the experimental changes in area per lipid reported by Weber et al.[9]

Lipid	Volume (%)	Area (%)	Thickness (%)	$(\Delta A/A)_{str}$ (%)	Weber et al.
POPC	5.46	16.4	−9.6	12.8	15.6%
DOPC	9.96	19.5	−8.1	12.9	19.1%

Soft Matter

The hydroperoxide group is represented by two connected beads, one is hydrophobic (C3) referred to as hydrophobic oxidised and the other is hydrophilic (P2) referred to as polar oxidised, kept at a relative distance of 0.33 nm. The distribution of the polar oxidised beads, representing the OOH side group, is naturally wider than their hydrophobic counterpart which belongs to the lipid tail backbone. A bimodal distribution is seen in both cases. Roughly half of the polar oxidised beads overlap with the glycerol group in the case of HP-POPC, with the other half remaining "buried" at the same place as the corresponding beads of the opposite saturated lipid tails (Fig. 3 above). By comparison, only a quarter of the polar oxidised beads in DHP-DOPC occupy a region close to the glycerol part, the other three quarters staying deep into the hydrophobic region (Fig. 3 below). As DHP-DOPC has twice as many oxidised groups as HP-POPC, it seems that all the extra oxidised beads go into the hydrophobic core of the bilayer, and that the interfacial glycerol region cannot take more oxidised groups than it has in the HP-POPC case. This is consistent with the data in Table 3 suggesting that the structural increase in area per lipid is similar for both species.

Fig. 4 depicts the orientational distribution of the packing angles: the angle between the oxidised tail and the z-axis α and the angle between two tails of the lipid β. Both DHP-DOPC and HP-POPC have a similar distribution of α, though, judging from the wider distribution, HP-POPC has a larger averaged angle than DHP-DOPC. Peroxidised lipids are therefore significantly tilted with respect to the bilayer normal.

The angle β is defined as the angle between the oxidised bead, the glycerol bead and the mirror alkyl bead in the opposite tail. We find a wide distribution of β for DHP-DOPC with a peak value of around $68°$. In turn, the angle distribution

of β for HP-POPC is narrower with its peak value being around $51°$. The packing angle β is closely related to the effective shape of a lipid molecule and thus it determines the ability of lipids to form a stable bilayer. Wide angles correspond to larger deviations from the cylindrical shape, possibly resulting in less stable bilayers.

3.3 Elasticity of hydroperoxidised bilayers

The membrane compressibility (or stretching modulus) K_A gives the relative area (A) variation consecutive to applied tension (σ), according to the definition:[25]

$$K_A = \frac{1}{A}\left(\frac{dA}{d\sigma}\right)_{T,P}. \tag{2}$$

The stretching modulus can be experimentally determined by micropipette aspiration.[26] Values of K_A for DHP-DOPC and HP-POPC were published first by Weber *et al.*[9] and are summarised in Table 4.

The elastic coefficients K_A associated with our coarse-grained numerical models come from an area fluctuation analysis, according to the equilibrium statistical relation

$$K_A = \frac{k_B T \langle A \rangle}{\langle A^2 \rangle - \langle A \rangle^2} = \frac{k_B T}{4(\langle L_x^2 \rangle - \langle L_x \rangle^2)}, \tag{3}$$

with $\langle A \rangle$ and $\langle A^2 \rangle$ being the mean value and the quadratic fluctuation of the sample monolayer area $A = L_x L_y$, and $\langle L_x \rangle$ and $\langle L_x^2 \rangle$ being the mean value and the quadratic fluctuation of the lateral size of the anisotropic simulation box. The fluctuations of area result from coupling the system to a semi-isotropic Parrinello–Rahman barostat,[28] known to generate the adequate constant pressure box size fluctuations. It can be shown that the elastic coefficient determined in this way is consistent with the one obtained by exerting a change in lateral stress (tension) on the membrane. The uncertainties quoted in Table 4 are associated with the precision to which $\langle L_x^2 \rangle - \langle L_x \rangle^2$ is determined.

Numerical estimates of K_A notoriously depend on the sample size.[20] According to den Otter, larger samples appear softer due to long wavelength undulation modes, whose contributions can be accounted for analytically in the relevant limit.[21] Using this analytical relation (*cf.* Section 4) a better, undulation-free estimate of the membrane compressibility can be inferred, based on the apparent K_A corresponding to two different sample sizes.

We report in Table 4 our values obtained for 512 (small) and 8192 (large) lipid samples, along with the undulation free extrapolation.
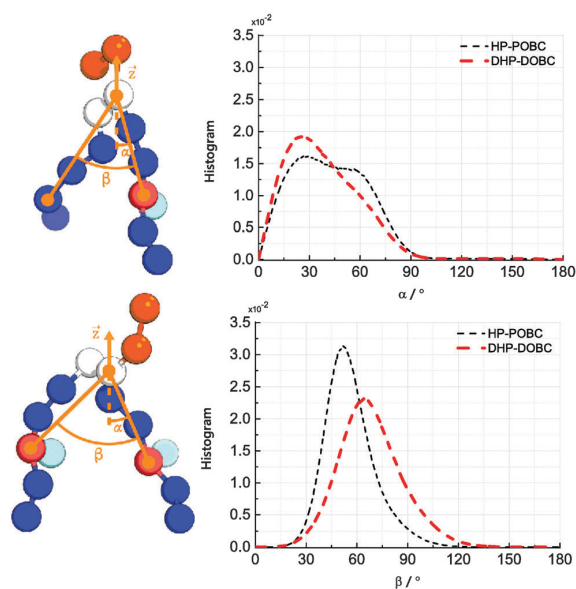
Fig. 4 (left) Definition of the tilting and opening angles α and β. (right) Distribution of orientations of α and β for HP-POPC and DHP-DOPC.

Table 4 Stretching moduli of POPC, HP-POPC, DOPC, and DHP-DOPC. Experimental results for POPC and DOPC bilayers are taken from the report of Rawicz *et al.*,[26] and for HP-POPC and DHP-DOPC from the report of Weber *et al.*[9]

	K_A (mN m^{-1})			
	512 CG model	8192 CG model	Undulation free	Experimental
POPC	379 ± 21	245 ± 42	393 ± 25	230 ± 10
HP-POPC	211 ± 11	104 ± 25	227 ± 16	~ 50
DOPC	357 ± 19	230 ± 27	371 ± 22	265 ± 18
DHP-DOPC	103 ± 12	73 ± 7	106 ± 14	~ 50

Paper

Soft Matter

For DOPC and POPC bilayers, the MARTINI CG model over-estimates the accepted experimental values, while large samples (*e.g.* 8192 lipids in our case) show a (coincidental) better agreement with them. We assume that the same trend holds for the hydroperoxidised bilayers. Our investigations suggest that hydroperoxidation leads to a significant decrease of K_A in both POPC and DOPC cases, whether the simulated system is small or large. This decrease of K_A upon peroxidation appears therefore like a robust and significant trend.

The membrane bending modulus coefficient κ_b controls the out-of-plane bending deformation of a membrane in the Canham–Helfrich elastic model.[29] It can be determined experimentally by a number of techniques, including micropipette vesicle aspiration, vesicle flicker motion and nanotube pulling, but unfortunately we are not aware of any published values of κ_b to date. We therefore take our values as predictions.

The numerical determination of the bending modulus requires to deal with simulated systems of sufficient size corresponding to a small ratio L_b/L_x between the membrane thickness and the lateral extension. Only under these conditions does the continuous Helfrich elastic model bring a reasonable description of the out-of-plane membrane fluctuations. Our determination of κ_b is based on the equilibrium fluctuation analysis of samples comprising 8192 lipids. Larger systems would approach better the Helfrich continuous limit, but equilibration times tend to increase sharply due to a combination of weak restoring forces and hydrodynamic effects, in spite of the parallel computation capabilities of the simulation tools.

In the continuum model, the bending modulus appears in the quadratic out-of-plane fluctuation spectrum $\langle u(q)u(-q)\rangle$, where q is the wavevector parallel to the membrane plane, and $u(x,y)$ the out-of-plane displacement in the Monge representation (elevation of the continuous surface):

$$\langle u(q)u(-q)\rangle = \frac{k_B T}{\kappa_b}\frac{1}{\langle A\rangle q^4}. \tag{4}$$

Numerical simulations do not provide $u(x,y)$ directly, and there is a certain arbitrariness when it comes to determining $u(x,y)$ from the discrete bead representation of the lipid molecules.

At the molecular scale, each lipid fluctuates around the average bilayer position, due to tilt, protrusion and other possible movements. This gives extra-contributions to the structure factor of the bilayer, and eqn (4) is not expected to hold exactly.[30] At smaller q, however, eqn (4) should hold for tensionless bilayers.

We derive our numerical estimate of the bending moduli by fitting $\langle U(q)U(-q)\rangle$ to a q^{-4} behaviour, where $U(q)$ is a discrete bead estimate of the elevation field $u(q)$[31] (see Fig. 6 and Section 4 for details). Our predictions for κ_b are summarised in Table 5. As for the area compressibility (or stretching) coefficient, hydroperoxidation causes a sharp decrease in the
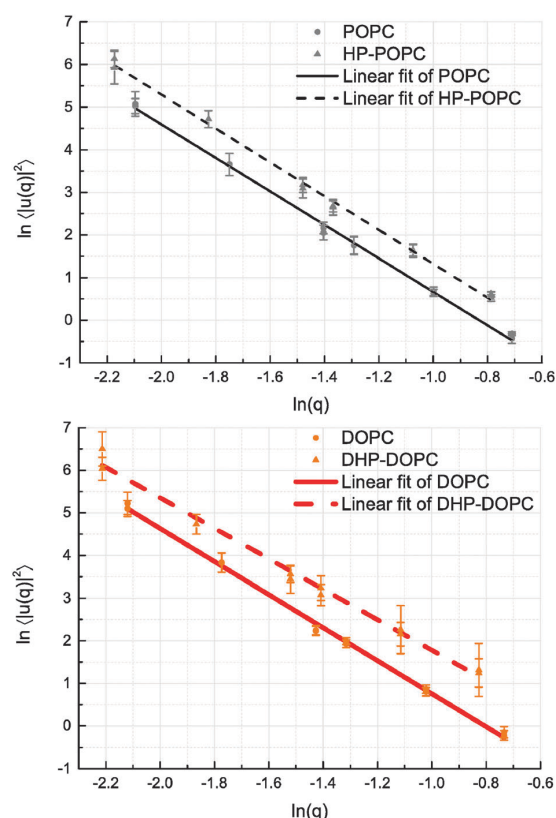
Fig. 6 Log-scale representation of the out-of-plane fluctuations of the bilayers. Only $q < 0.35$ [$\ln(q) < -1.05$] values were used for fitting the q^{-4} behaviour (q in nm^{-1} unit). Deviation from a q^{-4} behaviour can be seen in the DHP-DOPC case, which is the softest among all bilayers.

Table 5 Bending moduli of POPC, DOPC, hydroperoxidised POPC and DOPC molecules. Experimental data are taken from the report of Rawicz *et al.*[26]

	κ_b $(k_B T)$	κ_b (10^{-20} J)	
	CG model	CG model	Experimental
POPC	30.0 ± 1.5	12.4 ± 0.7	9.0 ± 0.6
HP-POPC	15.1 ± 0.9	6.3 ± 0.4	—
DOPC	28.3 ± 1.5	11.7 ± 0.7	8.5 ± 1.0
DHP-DOPC	12.8 ± 1.2	5.3 ± 0.5	—

Fig. 5 Mean lateral displacements $\Delta x^2 + \Delta y^2$ *versus* time, for the four kinds of lipids.

Soft Matter

Table 6 Diffusion coefficients of the numerical CG lipids. Experimental values were taken from ref. 27. Coarse-graining molecular dynamics is always faster than reality by a significant factor. Only relative trends may be of significance

	D (μm^2 s^{-1})	
	CG model	Experimental
POPC	40.2 ± 2.6	4.2 ± 0.4
HP-POPC	32.2 ± 2.2	—
DOPC	34.5 ± 1.5	6.3 ± 0.2
DHP-DOPC	24.4 ± 2.2	—

bending modulus value. As a result, the elastic bending forces are weaker, and the bilayer undulation dynamics is slower.

The POPC, HP-POPC and DOPC undulation spectra all follow the Helfrich q^{-4} behaviour, while DHP-DOPC undulations do not comply with it so well, showing a weaker appearent exponent. This might be due to DHP-DOPC molecules not fitting perfectly into the bilayer structure.

3.4 Relative changes in diffusion coefficients

We have estimated the diffusion coefficient of each lipid, at 300 K, using the MARTINI coarse-grained dynamics. It is known that coarse-graining predicts faster diffusion than experimentally observed. The extent of the acceleration factor, depending on temperature, may lie between 4 and 10. We observe that the hydroperoxidised lipids diffuse slower than the non-oxidised molecules by roughly 25%. This suggests an increased cohesion between peroxidised molecules, but only by a modest amount.

The lateral diffusion coefficient was calculated from the mean-square displacement (MSD) of lipid centres of masses with time. The resulting MSD curves are linear, to a good approximation, over a time interval between 20 and 50 ns (simulation time). Lateral diffusion coefficients were obtained from linear fits of these MSD curves between 20 and 50 ns.

According to Table 6 and Fig. 5, the lateral diffusion coefficient decreases due to lipid oxidation, and we observe that the diffusion coefficient ratio between the oxidised and the non-oxidised species is similar in both cases: 0.77 for HP-POPC/POPC and 0.76 for DHP-DOPC/DOPC. The decrease in diffusion coefficient could arise from a larger friction at the water–bilayer interface, or from stronger lipid–lipid interaction, due to attractive patches in the tails at the position of the peroxide groups. The former interpretation is more consistent with the common 25% drop in value.

Two experimental values, based on fluorescent probe diffusion, are provided to show the expected order of magnitude of the ratio between CG simulated and experimental time scales.[27] This choice is somewhat arbitrary, as a large number of experimental diffusion coefficient values are available, which differ greatly depending on the technique and system preparation. Coarse-grained models do not perform very well as far as reproducing dynamics and transport properties.[32] We see a reduction of lipid mobility upon peroxidation that seems to be due to increased friction between peroxidized groups and interfacial water. It might be that important dynamical changes, which are not be accounted for in our approach, alter the overall picture.

4 Simulation and analysis details

4.1 Parameterisation of the CG hydroperoxidised lipids

A first attempt was made by substituting one hydrophobic bead with an hydrophilic bead. Based on $\log P_{ow}$, we find that a moderately hydrophilic bead does not account for the observed area change. Conversely, a significant area increase can only be obtained for strongly hydrophilic beads which violate the log P_{ow} requirement. The partition coefficient and the increase in area per lipid can be reconciled by modelling the hydroperoxide group as two partially overlapping beads. A systematic screening was performed with pairs of beads with different polarities (C1 till C3, and P1 till P4) and separations (0.3 till 0.4 nm) and compared to the experimental area per lipids of both HP-POPC and DHP-DOPC. Two dimers (C2–P2) and (C3–P2) emerged as the best contenders based on both partitioning and area per lipid criteria. Both could be used with little changes in the results and we picked-up C3–P2 as a reference dimer. To give an idea on how much bead separation affects the area per lipid, we note that a distance of 0.32 nm would give area changes of +15.8% (HP-POPC) and +17.7% (DHP-DOPC), as compared with values in Table 3, obtained for 0.33 nm.

Most MARTINI CG beads have a Van der Waals radius $\sigma = 0.47$ nm, so that a dimer made up of two beads at distance $r = 0.33$ nm gives an excluded volume 50% larger than a single bead. More precisely, if the beads were hard spheres, the combination of two hard spheres of radius 0.47 separated by 0.33 gives a total excluded volume equal to 1.505 times the excluded volume of a single sphere. A direct consequence is that the volume per lipid increases by, respectively, 5.5% and 10% for POPC and DOPC. No bending potential was added between the C3–P2 bond and the remaining of the lipid chain. Steric interactions ensure that the polar moiety P2 remains at a distance from the chain, and additional structural information is lacking to improve over the current parameterisation. One must remember also that our CG model stands for a chemical mixture of at least two chemical compounds, for which the *cis* or *trans* nature of the unsaturated double bond is not established even though a majority of *trans* bonds is expected.

Partitioning of the corresponding C3–P2 dimers was carried out by studying a slab of 1920 octanol molecules (MARTINI "OCO" dimers) surrounded by 2000 "water molecules" (one CG water representing 4 real water molecules), in which 40 dimers were inserted. The concentration ratio was found to be $P_{ow} =$ [C3P2]$_{oct}$/[C3P2]$_w = 26$, or equivalently $\log P_{ow} = 1.4$. This can, for instance, be compared with the estimated $\log P_{ow} = 0.9$ of *tert*-butyl hydroperoxide ((CH_3)$_3$COOH, CAS-75-91-2), obtained using a $\log P_{ow}$ predicting software (VCCLab[33]). This indicates that our residue C3–P2 has a realistic hydrophilic–hydrophobic balance.

4.2 Stability of peroxidised bilayers

Bilayers composed of single components HP-POPC and DHP-DOPC are stable, to the extent that systems composed of pure HP-POPC and DHP-POPC exhibit stationary properties and show no significant evolution over the simulated times. In practice,

Paper

initial configurations are obtained by starting from thermalized POPC and DOPC bilayers, inserting the extra beads and reequilibrating the systems again.

4.3 Simulation details

This CG model of peroxidised lipids is built on version 2.0 of MARTINI lipid molecule topologies and version 2.1 of the bead interaction parameters. Trajectories were produced using Gromacs v-4.6.

Simulations were carried out at constant temperature (300 K) using the Gromacs v-rescale weak coupling scheme, which is an alternative to the Nose–Hoover thermostat (time constant 1 ps).[34] An anisotropic Parrinello–Rahman barostat was used to model a tensionless bilayer (time constant 12 ps, compressibility 3×10^{-4} bar^{-1}). Simulation box size fluctuations are assumed to be consistent with a constant temperature–pressure ensemble, and were used as such for the determination of the membrane area compressibility coefficient.

Short range electrostatics is assumed, with truncation at a radius of 1.2 nm, while the Verlet neighbour list radius was set to 1.4 nm. Time steps of 30 fs and 40 fs were used throughout, in the absence of rigid constraints, without noticeable differences in the output. Simulation times are summarized in Table 7.

4.4 Size dependence of the elastic compressibility coefficient

Eqn (14) in ref. 21 relates the apparent compressibility $K_{A_\parallel}$ to the undulation free compressibility K_A, given the system projected area $A_\parallel$ and the membrane bending modulus κ. It reads

$$K_{A_\parallel}^{-1} = K_A^{-1} + \frac{k_B T}{32\pi^3 \kappa^2} A_\parallel. \tag{5}$$

This expression assumes a Canham–Helfrich elastic behaviour, and accounts for modes of wavelength $2\pi \big/ \sqrt{A_\parallel} < q < 2\pi/\lambda$, with λ being the characteristic length of the size of the membrane thickness. If $K_{A_\parallel,1}$ and $K_{A_\parallel,2}$ are known for two different projected areas $A_{\parallel,1}$ and $A_{\parallel,2}$, one can extract an effective bending modulus κ and derive K_A from eqn (5)

$$\left(\frac{\kappa}{k_B T}\right)^2 = \frac{1}{32\pi^3 k_B T}\left(\frac{A_{\parallel,1} - A_{\parallel,2}}{K_{A_\parallel,1}^{-1} - K_{A_\parallel,2}^{-1}}\right) \tag{6}$$

This is a less accurate estimate of κ than fitting the undulation spectrum to a Helfrich q^{-4} law, as (5) considers modes $q \sim 2\pi/\lambda$ which may deviate from the ideal Helfrich behaviour. The values of κ found in this way are nevertheless reasonably

similar to those determined directly, namely 30 kT (POPC), 28.3 kT (POPC), 15.1 kT (HP-POPC) and 12.8 kT (DHP-DOPC). This is 50% larger than the values in Table 5, except for DHP-DOPC for which the agreement is better. The related undulation free K_A coefficients are shown in the third column of Table 4.

4.5 Fitting and estimation of errors

Averages of the area, simulation box volume and thickness come from the thermodynamic data recorded during the simulations, and Gaussian confidence intervals on the sampled means were obtained by using a bunching/boxing algorithm for time-correlated time sequences.[35] The statistical precision of these quantities is very satisfactory.

The bunching algorithm was also used to estimate the accuracy of the sample variance of the statistical L_x time sequence. This leads to larger uncertainties for the compressibility coefficients K_A. In the case of the undulation free K_A, uncertainties in $K_{A\parallel}$ dominate the final error.

Modes $U(q,t)$ reflect the Fourier transform of the centre of masses density field. Let us denote (x_i, y_i, z_i) as the space coordinates of the centre of mass of each lipid molecule in one of the bilayer leaflet, and N_l as the number of lipids in this leaflet. The density field in reciprocal space is given by

$$
\begin{aligned}
\hat{\rho}_q &= \frac{1}{N_l}\sum_{i=1}^{N_l} \exp\big(iq_x x_i(t) + iq_y y_i(t) + iq_z z_i(t)\big) \\
&= \frac{1}{N_l}\sum_{i=1}^{N_l} \exp\big(iq_x x_i(t) + iq_y y_i(t)\big)[1 + iq_z z_i(t)] \\
&= \hat{\rho}_\parallel(t) + iq_z U(q,t)
\end{aligned} \tag{7}
$$

We therefore simply assume that $u(q_x, q_y) \simeq U(q_x, q_y) = N_l^{-1}\sum_i z_i \exp(iq_x x_i + iq_y y_i)$. The undulation mode spectra $\ln(\langle U(q_x,q_y)U(-q_x,-q_y)\rangle)$ were fitted to straight lines $C - 4\ln(q)$; $q = \sqrt{q_x{}^2 + q_y{}^2}$, with uncertainties resulting from a standard χ_2 least-squares procedure.[36]

A similar estimate of the values and confidence intervals for the diffusion coefficients was used, based on the average and variance of the quadratic displacement time signal $S(t,\tau)$ of the lipid centers of masses, with respect to t, for fixed τ.

$$S(t,\tau) = \frac{1}{N}\sum_i \big(x_i(t+\tau) - x_i(t)\big)^2 + \big(y_i(t+\tau) - y_i(t)\big)^2. \tag{8}$$

5 Conclusions

We presented a coarse-grained model for two hydroperoxidised phospholipids based on the MARTINI force field for POPC and DOPC. The parameters of our coarse-grained molecules were set by combining thermodynamic data (the TBHP partitioning coefficient), molecular packing arguments (the addition of OOH group) and area per lipid changes.

The resulting molecules, HP-POPC and DHP-DOPC, form stable bilayers in accessible simulation times. Our results

Table 7 Trajectories used for the determination of structural parameters

Lipids	MD steps, $\times 10^6$	CG time (ns)
512 POPC	10	400
512 DOPC	10	400
512 HP-POPC	20	800
512 DHP-DOPC	20	800
8192 POPC	20	600
8192 DOPC	20	600
8192 HP-POPC	40	1200
8192 DHP-DOPC	30	900

Soft Matter

suggest that the excess area per lipid caused by peroxidation is common to both species, about 13% in relative value. The hydroperoxidised bilayers are thinner and softer than their non-oxidised counterparts. A significant drop in the compressibility (stretching) coefficient K_A is observed, qualitatively similar to experimental values. A similar drop of the bending coefficient κ_b is predicted. The diffusion coefficient of the coarse-grained hydroperoxidised lipids shows a 25% decrease as compared with the non-oxidised ones.

Using our model, we derive the lateral distribution of peroxide groups in the bilayers, and gain access to various structural data, such as the variation of area per lipid, density profile, compressibility, bending moduli, and diffusion coefficient of lipids. We hope that new experimental results will appear in the close future that can be compared to the picture presented above.

A question of interest concerns mixtures of regular and peroxidised lipid species, and in particular the possible non-ideal features of such systems. The presence of heterogeneities, if established, would be an element to be considered in the understanding of the physiological consequences of lipid peroxidation. We are currently working in this direction, with the help of these newly introduced lipid models.

Acknowledgements

References

1 R. Kohen and A. Nyska, *Toxicol. Pathol.*, 2002, **30**, 620–650.
2 B. Alberts, A. Johnson, J. Lewis, M. Raff, K. Roberts and P. Walter, *Molecular Biology of the Cell*, Garland Science, 4th edn, 2002.
3 M. Repetto, J. Semprine and A. Boveris, *Lipid Peroxidation*, InTech, 2012.
4 B. Frei, *FASEB J.*, 1999, **13**, 963–964.
5 D. J. Betteridge, *Metabolism*, 2000, **49**, 3–8.
6 S. I. Liochev, *Free Radical Biol. Med.*, 2013, **60**, 1–4.
7 K. A. Riske, T. P. Sudbrack, N. L. Archilha, A. F. Uchoa, A. P. Schroder, C. M. Marques, M. S. Baptista and R. Itri, *Biophys. J.*, 2009, **97**, 1362–1370.
8 O. Mertins, I. O. Bacellar, F. Thalmann, C. M. Marques, M. S. Baptista and R. Itri, *Biophys. J.*, 2014, **106**, 162–171.
9 G. Weber, T. Charitat, M. S. Baptista, A. F. Uchoa, C. Pavani, H. C. Junqueira, Y. Guo, V. A. Baulin, R. Itri, C. M. Marques and A. P. Schroder, *Soft Matter*, 2014, **10**, 4241–4247.
10 S. Sankhagowit, S.-H. Wu, R. Biswas, C. T. Riche, M. L. Povinelli and N. Malmstadt, *Biochim. Biophys. Acta*, 2014, **1838**, 2615–2624.
11 P. H. B. Aoki, A. P. Schroder, C. J. L. Constantino and C. M. Marques, *Soft Matter*, 2015, **11**, 5995–5998.
12 H. Khandelia and O. G. Mouritsen, *Biophys. J.*, 2009, **96**, 2734–2743.
13 V. Jarerattanachat, M. Karttunen and J. Wong-ekkabut, *J. Phys. Chem. B*, 2013, **117**, 8490–8501.
14 J. Wong-Ekkabut, Z. Xu, W. Triampo, I. M. Tang, D. P. Tieleman and L. Monticelli, *Biophys. J.*, 2007, **93**, 4225–4236.
15 J. Garrec, A. Monari, X. Assfeld, L. M. Mir and M. Tarek, *J. Phys. Chem. Lett.*, 2014, **5**, 1653–1658.
16 H. Khandelia, B. Loubet, A. Olżyńska, P. Jurkiewicz and M. Hof, *Soft Matter*, 2013, **10**, 639–647.
17 S. Pogodin and V. A. Baulin, *Soft Matter*, 2010, **6**, 2216–2226.
18 M. Muller, K. Katsov and M. Schick, *J. Polym. Sci., Part B: Polym. Phys.*, 2003, **41**, 1441–1450.
19 S. J. Marrink, H. J. Risselada, S. Yefimov, D. P. Tieleman and A. H. de Vries, *J. Phys. Chem. B*, 2007, **111**, 7812–7824.
20 S. J. Marrink, A. H. de Vries and A. E. Mark, *J. Phys. Chem. B*, 2004, **108**, 750–760.
21 W. K. den Otter, *J. Chem. Phys.*, 2005, **123**, 214906.
22 H. Sies, *Angew. Chem., Int. Ed.*, 1986, **25**, 1058–1071.
23 S. P. Stratton and D. C. Liebler, *Biochemistry*, 1997, **36**, 12911–12920.
24 J. Sanchez and T. N. Myers, *Kirk-Othmer Encyclopedia of Chemical Technology*, John Wiley & Sons, Inc., 2000.
25 G. Cevc and D. Marsh, *Phospholipid Bilayers: Physical Principles and Models*, Wiley-Interscience, New York, 1st edn, 1987.
26 W. Rawicz, K. C. Olbrich, T. McIntosh, D. Needham and E. Evans, *Biophys. J.*, 2000, **79**, 328–339.
27 D. Marsh, *Handbook of Lipid Bilayers*, CRC Press, Boca Raton, 2nd edn, 2013.
28 M. Parrinello and A. Rahman, *J. Appl. Phys.*, 1981, **52**, 7182–7190.
29 W. Helfrich, *Z. Naturforsch., C: Biochem., Biophys., Biol., Virol.*, 1973, **28**, 693–703.
30 G. Brannigan and F. L. H. Brown, *Biophys. J.*, 2006, **90**, 1501–1520.
31 E. G. Brandt, A. R. Braun, J. N. Sachs, J. F. Nagle and O. Edholm, *Biophys. J.*, 2011, **100**, 2104–2111.
32 W. K. den Otter and S. A. Shkulipa, *Biophys. J.*, 2007, **93**, 423–433.
33 I. V. Tetko, J. Gasteiger, R. Todeschini, A. Mauri, D. Livingstone, P. Ertl, V. A. Palyulin, E. V. Radchenko, N. S. Zefirov, A. S. Makarenko, V. Y. Tanchuk and V. V. Prokopenko, *J. Comput.-Aided Mol. Des.*, 2005, **19**, 453–463.
34 G. Bussi, D. Donadio and M. Parrinello, *J. Chem. Phys.*, 2007, **126**, 014101.
35 M. P. Allen and D. J. Tildesley, *Computer simulation of liquids*, Clarendon Press, 1987.
36 W. H. Press, S. A. Teukolsky, W. T. Vetterling and B. P. Flannery, *Numerical Recipes in C (2Nd Ed.): The Art of Scientific Computing*, Cambridge University Press, New York, NY, USA, 1992.

5

GPU IMPLEMENTATION OF THE ROSENBLUTH CHAIN GENERATION
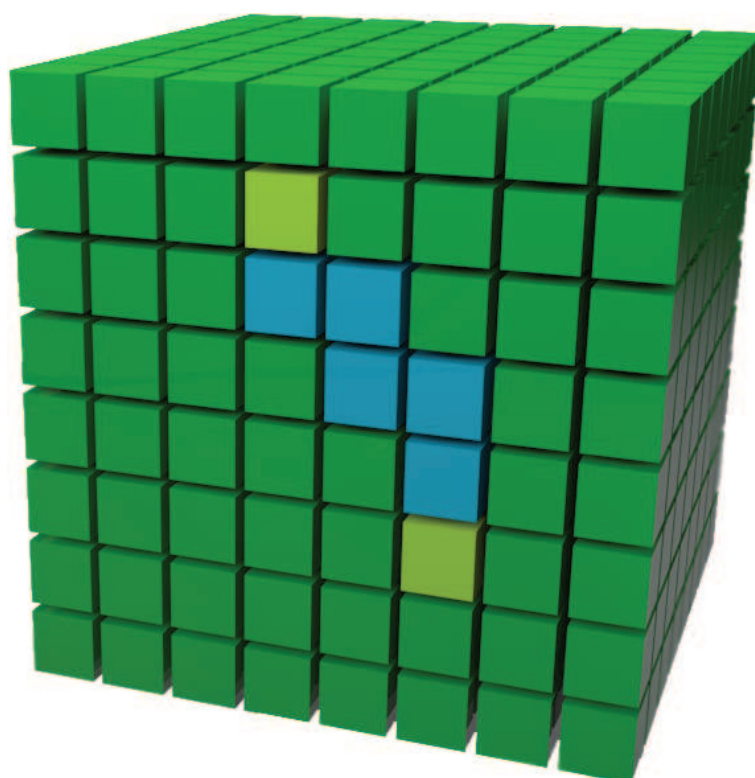
GPU Implementation of the Rosenbluth Generation Method for Static Monte Carlo Simulations

Yachong Guo and Vladimir A. Baulin*

Departament d'Enginyeria Quimica, Universitat Rovira i Virgili 26 Av. dels Paisos Catalans, 43007 Tarragona, Spain

E-mail: vladimir.baulin@urv.cat
Phone: +34 977 55 85 77. Fax: +34 977 55 96 21

Abstract

Highly parallel version of Rosenbluth Self-Avoiding Walk generation method is implemented on GPU using CUDA libraries. The speedup of the method has only hardware restrictions of actual GPU on the market: number of CUDA cores and amount of shared memory. The implemented method runs thousands times faster on NVIDIA GPUs compared to single-core serial CPU implementation. Two realizations of the method are introduced: Rosenbluth method on a lattice and in real space. We performed series of static Monte Carlo simulations of linear polymers such as the end-to-end distance and found good agreement between serial and parallel implementations and consistent results between lattice and real space realizations. The developed GPU implementations of Rosenbluth algorithm can be used in Monte Carlo simulations and other computational methods that require large sampling of molecules conformations.

1 Introduction

Statistical methods and computer simulations play major role in theoretical understanding of many-body interactions in physics and chemistry.[1] In particular, Molecular Dynamics (MD) and Monte Carlo (MC) methods[2] are the main theoretical tools used to describe physical and chemical processes at the molecular level. Increasing computer power and availability of computational recourses contribute in growing popularity of computational methods. Even computationally expensive *ab-initio* calculations become feasible nowadays: the length-scales and time-scales of atomistic simulations increased more than 10 times in a decade.[3]

However, mostly used computational methods such as MD and MC simulations and numerous computational techniques were conceived at the beginning of computer era in the late 1950s,[4] when a rigid architecture of single-core microprocessors imposed on the structure of the theoretical methods in form of a list of instructions for Central Processing Unit (CPU) implemented sequentially. Miniaturization of processors and increase of clock frequency is reaching the limit[5] impeding further increase of computational efficiency. To handle that problem computer industry explores two main paths: multi-core and many-thread processors.[6] Both ways assume parallelization of tasks and synchronous work with data.

Rapidly growing industry of Graphics Processing Units (GPUs) driven by fast-growing video game market provides new dimension in computational resources: a current example is the NVIDIA Tesla K40 that can reach about 5-8 trillion floating-point operations per

second, while a new released Intel Core i7-5960K (Xenon Haswell) processor can only reach 350 billion floating-point operations per second. This makes GPU very attractive for scientific computation[7] and many traditional scientific methods including MD, MC, finite element analysis were adapted for GPU. As a result, GPU versions of the codes are accelerated by factors from 10 to 100 compared to single core CPUs.[8–12]

Nevertheless, the adapted parallel versions of traditional methods cannot use full advantage of GPU architecture, because they were designed conceptually for sequential implementation and thus, contain large portions of non-parallilizible parts and inter-connections that require communication between the cores, for example, to update the list of nearest neighbors. Thus, the development of new generation of methods specially designed for modern highly parallel architecture is necessary.

In the present work we present a highly parallel version of Rosenbluth method which is in the ground of static MC simulations first introduced in 1955.[13] Two parallel implementations on graphics processors units (GPU) of the Rosenbluth method are presented: on the lattice and in real space leading to drastic speed increase in simulation in polymer and soft matter science.

The paper is organized as follows. After brief description of static MC methods in Section 2, we describe the GPU implementation of Rosenbluth sampling method in Section 3. Comparative examples between serial and parallel Rosenbluth implementations for Polymer Chain less than 64 monomers are presented in Section 4. We summarize our results in Section 5.

2   Static Monte Carlo methods

In equilibrium statistical mechanics thermodynamic properties are represented by the ensemble averages over all coordinates of N particles r^N. In the canonical ensemble the classical expression for the partition function Q is given by:[1]

$$Q = C \int dp^N dr^N \exp\left[-\mathcal{H}\left(p^N, r^N\right)/k_B T\right],$$

(1)

where p^N stands for the corresponding momenta, $\mathcal{H}\left(p^N, r^N\right)$ is the Hamiltonian of the system. It describes the whole energy of an isolated system as a function of the momenta and coordinates of the constituent particles: $\mathcal{H} = \mathcal{K} + \mathcal{U}$, where $\mathcal{K}$ is the kinetic energy of the system and $\mathcal{U}$ is the potential energy. C represents the normalization constant . For a system of N identical atoms, $C = 1/(h^{3N} N!)$. The classical equation to compute the thermal average of observable A becomes

$$\langle A \rangle = \frac{\int dp^N dr^N A(p^N, r^N) \exp\left[-\beta \mathcal{H}\left(p^N, r^N\right)\right]}{\int dp^N dr^N \exp\left[-\beta \mathcal{H}\left(p^N, r^N\right)\right]},$$

(2)

where $\beta = 1/k_B T$, in many cases, we are not interested in the configuration part of the partition function itself but in averages of the type:

$$\langle A \rangle = \frac{\int dr^N A(r^N) \exp\left[-\beta \mathcal{U}\left(r^N\right)\right]}{\int dr^N \exp\left[-\beta \mathcal{U}\left(r^N\right)\right]}$$

(3)

In general, the integral cannot be solved analytically. However, MC simulations provide a numerical approach to this problem by generating a random sample of configuration space points $r_1^N, r_2^N ... r_\Gamma^N$, due to the high degree of freedom depending on N, it is in general not possible to gain access to the entire original distribution, we cloud use a similar but smaller sampling distribution $P_s(r^N)$ to replace the original one then correcting for the error introduced by making this switch, such technique is also know as representative sampling.[14] $\langle A \rangle$ is then estimated by

$$\overline{A} = \frac{\sum_{\gamma=1}^{\Gamma} A\left(r_\gamma^N\right) \exp\left[-\beta \mathcal{U}\left(r_\gamma^N\right)\right]/P_s(r_\gamma^N)}{\sum_{\gamma=1}^{\Gamma} \exp\left[-\beta \mathcal{U}\left(r_\gamma^N\right)\right]/P_s(r_\gamma^N)}$$

(4)

Whether $\overline{A}$ represents a good estimate for $\langle A \rangle$

depends on the total number Γ of configurations used and, for a given Γ, on the choice of $P_s(r^N)$.

$P_s(r^N)$ should approximate $\exp\left[-\beta \mathcal{U}\left(r^N\right)\right]$ as closely as possible to obtain meaningful results from MC simulation. MC simulation can be usually distinguished between static MC and dynamic MC method. The methods focus on different perspectives of problems with different advantages. In this paper we mainly focus on the static MC, where a sequence of statistically independent configuration-space points from the distribution $P_s(r^N)$ is generated as basic sampling.

There exists a large class of sampling algorithms based on MC methods. Rosenbluth sampling is a MC method for generating correctly distributed Self Avoiding Walk (SAW) by means of weights calculated on the fly. Rosenbluth sampling method have been widely applied and used due to its efficiency, simplicity to program.

The basic idea of Rosenbluth sampling is to avoid self-intersections by only sampling from the steps that lead to self-avoiding configurations. Hence the algorithm will terminate only when the walk is trapped in a dead end and cannot continue growing. Although this still happens exponentially often for long chain, Rosenbluth sampling can produce substantially longer configurations than simple sampling.

During Rosenbluth generation process,[13] a monomer can be placed to adjacent sites with different possibilities, which can be selected with a probability p. Thus, the weight of the generated configuration is multiplied by $1/p$. An n-step walk grown by Rosenbluth sampling therefore has a weight

$$W_n = \prod_{i=0}^{n-1} \frac{1}{p_i} \qquad (5)$$

where $1/p_i$ is the number of ways in which a configuration can continue to grow after i-th growth step. This walk is generated with the probability $P_n = 1/W_n$. eq 5 shows that configurations with lower p_i have a lower probability of occurring. This bias toward dense configurations in the production of a SAW must be corrected in its analysis by the weight W when

calculating observables, see also eq 4.

3 Gpu Implementation of Rosenbluth algorithm

3.1 Domain decomposition

For the lattice space, we subdivide the full space into $M \times M \times M$ ($M \in \mathbb{N}^+$) lattice units, where each lattice unit can be occupied by only one monomer at a time. Each monomer occupies one lattice site, the bond length equals the lattice constant, and the bond angles are restricted by the lattice geometry and by the repulsive hard-core monomer-monomer interaction. M is set to 64 in this paper. The coordinates of the monomer therefore are stored as numerical integer type.

In the case of off-lattice, domain decomposition is not necessary. The coordinates of the monomer are stored as floating-point type. Double floating-point type could nevertheless be applied here, however, it is not recommended here since the double precision will greatly increase the shared memory consumption leading to push the GPU into the occupancy limitation and increasing bank conflicts. That is why all calculations are performed using single-precision floating-point operations; The performance of GPU with double-precision environment also need to be further improved in the future chip generations.

3.2 Random Number Generator

Generation of a representative sampling conformations of polymers require random numbers with long periods and good statistical properties. Generating pseudo-random numbers on a CPU is a well-studied topic,[15–17] in a GPU Single Instruction Multiple Thread (SIMT) environment, many approaches have been used for the generation of random numbers in different types of applications.[18,19] Designing and testing Random Number Generator (RNG) is a field in itself, and RNGs can be found in the literature for single stream computations,[15,16] or parallel implementations.[20,21] Any RNG chosen should

guarantee that random numbers to be generated and immediately consumed by user kernels without requiring the random numbers to be written to and then read from global memory. It also guarantees that each thread generates their own random number at the same time. In our code we chose the Mersenne twister,[22] which guarantees uncorrelated random number streams of each thread. A detailed implementation of Mersenne twister on GPU can be found, for example, in the SDK library from NVIDIA.[23]

Following the CUDA library, we initialize the RNG with a single seed but a different sequence number for every thread. To initialize the Mersenne twister generator,[15] its necessary to create a RNG[15] status for every thread and pass this status to the $Curand\_init$[23] function with a seed but different sequence number. The distance between the first elements in successive sequence for Mersenne twister is 2^{67}, so that its unlikely that two sequences will overlap even in extensive simulation. In our simulation, we initialize the Mersenne twister once and use the update RNG status for the entire calculation. Once the RNG is initialized, a normally distributed pseudo-random numbers can be generated for all individual threads. In current implementation, the initial seed was given before the starting of the sampling kernel.

3.3 Kernel implementation

3.3.1 Data structure

The proper choice of the data structure is critical for implementation performance. In the present work, all the coordinates of each monomer are stored in a shared memory during the SAW process, the coordinates of each conformation and corresponding Rosenbluth weight will be flushed to the global memory when the chain is successfully generated.

In a parallel perspective, for each block on GPU, D denotes the dimension of the space, $BlockDim.x$ is the block dimension defined by user and $chainlength$ is the total number of conformations to be generated. With this, D arrays with dimensions $BlockDim.x*chainlength$ are allocated in the shared memory to store the coordinates. Same numbers of arrays with dimensions $BlockDim.x$ are allocated in the shared memory to store a temporary position of the subunit during molecule generation. The variables, such as Rosenbluth weight, the increment counter of overlaps depend on the thread index, and are stored in the shared memory; each with the size of $BlockDim.x$ to distinguish between different configurations.

3.3.2 Lattice

The full computational task of parallel random monomer selection and random monomer move can be programmed at once in a single GPU kernel. There are however GPU memory restrictions on coalesced reads and writes, and more importantly on register use, which made this rather challenging. Each polymer confirmation is generated with each CUDA thread.

The number of blocks $NumBlock$ is defined as the total number of molecules to be generated divided by the number of threads per block. In this way each confirmation in each block is tagged by the thread number while generated. All the coordinates and weights associated with each conformation are stored in the shared memory. The first monomer is placed at the center of the coordinate system or it can also be placed at any position in the simulation box depending on realization. The second bond vector is randomly chosen within all $z = 26$ possible lattice space in 3D space and added to the monomer. Starting from the third monomer, a bias is introduced to the position of a new monomer because the new monomer may overlap with the previous monomers. This is taken into consideration in the so called Rosenbluth weight, which is, in detail, to calculate the probability of positioning a new monomer avoiding overlaps with previous bead. In the lattice model, the probability can be easily calculated by looking into the occupancy of previous generated beads in the $z = 26$ possible lattice space.

In the lattice model, we calculate the Rosenbluth weight after the whole chain is generated

---

Algorithm 1 Lattice Rosenbluth chain generation

Require: $BlockDim.x$ is the block dimension defined by user
Require: $seed$ is a random number seed chosen by the user
Require: $chainlength$ is the polymer chain length chosen by the user
Require: Function $rngonlattice$ generates a random position for the next monomer
Require: Function $distance$ calculates the distance between two monomers

1: $x, y, z \leftarrow BlockDim.x * chainlength$
2: $w \leftarrow BlockDim.x$
3: $rng \leftarrow rng(seed)$
4: **function** CHAINGENERATION
5:     **for** $i = 0 \rightarrow chainlength$ **do**
6:         **if** $i == 1$ **then**
7:             $Pos[0] \leftarrow 0$ $\triangleright$ $Pos[i]$ denotes position of monomer i (x_i, y_i, z_i)
8:             $p \leftarrow 1/6$ $\triangleright$ p denotes Rosenbluth weight
9:         **end if**
10:        **for** $k = 0 \rightarrow ptMax$ **do** $\triangleright$ $ptMax$ denotes total trial attempts
11:             $Pos[Temp] \leftarrow rngonlattice$
12:             $Pos[Temp] = Pos[i-1] + Pos[Temp]$
13:             $overlap \leftarrow$ **False**
14:             **for** $j = 0 \rightarrow i - 1$ **do**
15:                 **if** $Pos[j] \wedge Pos[Temp]$ **then**
16:                     $overlap \leftarrow$ **True**
17:                 **end if**
18:             **end for**
19:             **if** $\neg overlap$ **then**
20:                 $Pos[i] = Pos[Temp]$
21:                 $break$
22:             **end if**
23:         **end for**
24:     **end for**
25:     **for** $i = 1 \rightarrow chainlength - 1$ **do**
26:         $KK \leftarrow 0$
27:         **for** $j = 0 \rightarrow i - 1$ **do**
28:             $R2 \leftarrow distance(Pos[i], Pos[j])$
29:             **if** $R2 \leq d_{max}$ **then** $\triangleright$ d_{max} denotes the maximum polymer bondlength
30:                 $KK = KK + 1$
31:             **end if**
32:         **end for**
33:         $p = p * (1.0/(Cod - kk))$
34:     **end for**
35: **end function**

(a)   (b)
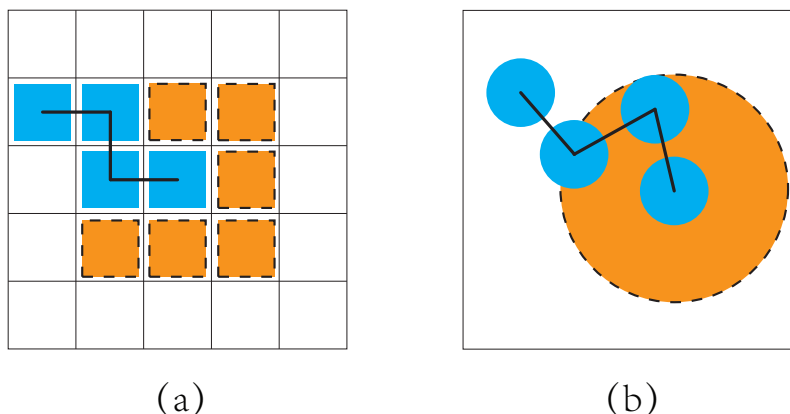
Figure 1: Schematic representation of chain generation in 2 dimension space: (a) on a lattice space (b) in a real space

to avoid the unnecessary calculation. During the chain generation, next monomer position is randomly chosen from the $z = 26$ neighbors of the present bead. This position will be accepted if there is no crossover with all previous generated beads.

The random chain growth process will be continued if the chain is self-avoiding. However, if the chain grow to a dead end when all possible nearby cells are occupied by previous monomers, whole generated sequence, obtained up to this point, must be discarded, and we have to start at the first step again. To repeat these steps we can get the SAW of a desired length N.

Also, a more computational expensive MC process can be applied by randomly place a new monomer and determine if it is overlapped with previous monomers until one gets enough accuracy for the probability to position a new monomer. Figure 1 illustrates this process for both lattice (a) and off-lattice (b) model. Blue stands for the monomers already generated while orange represents the space available for positioning the next monomer. The second realization is significantly more computationally expensive.

3.3.3 Off-Lattice

Off-lattice realization of the method is in in spirit similar to the lattice version as descriped in. The major difference lies in the probably

definition of the Rosenbluth weight. More precisely, to quantify the probability of positioning of a new monomer during chain generation. The Rosenbluth weight is proportional to the volume available for the placement at a next monomer.

The volume is estimated within a MC process introduced here. A bead is randomly placed N_{trial} attempts at a fixed distance from the previous bead and the number $N_{allowed}$ of successful positions is counted, taking into account the self-avoidance condition. If $N_{allowed} > 0$, a new position is accepted with the weight $1/N_{allowed}$, the weight of the conformation W_a is multiplied by the factor $1/N_{allowed}$. If there is no possibility to place a monomer, $N_{allowed} = 0$, the generation restarts from the beginning.

Figure 2a is a block diagram illustrating a GPU in accordance with the scope of this paper. Computation is performed by sets of streaming multiprocessors, each containing several computer units. Code is executed as a block of threads on a particular multiprocessor. Blocks of threads are grouped into a grid. Each multiprocessor contains a small shared memory store that can be accessed by all threads in a given block. For current implementation we define the size of the block. The total number of blocks or the grid will automatically be defined as the total number of chains dividing the block dimension. On a single block, each thread simultaneously and synchronously generates its

---

Algorithm 2 Off-Lattice Rosenbluth chain generation

Require: $BlockDim.x$ is the block dimension defined by user
Require: $seed$ is a random number seed chosen by the user
Require: $chainlength$ is the polymer chain length chosen by the user
Require: Function $rngonsphere$ generates a random position for the next monomer
Require: Function $distance$ calculates the distance between two monomers

1:    $x, y, z \leftarrow BlockDim.x * chainlength$
2:    $w \leftarrow BlockDim.x$
3:    $rng \leftarrow rng(seed)$
4: **function** CHAINGENERATION
5:      **for** $i = 0 \rightarrow chainlength$ **do**
6:        **if** $i == 1$ **then**
7:          $Pos[0] \leftarrow 0$ $\triangleright$ $Pos[i]$ denotes position of monomer i (x_i, y_i, z_i)
8:          $p \leftarrow 1$ $\triangleright$ p denotes Rosenbluth weight
9:        **end if**
10:       **for** $k = 0 \rightarrow ptMax$ **do** $\triangleright$ $ptMax$ denotes total trial attempts
11:          $Pos[Temp] \leftarrow rngonsphere$
12:          $Pos[Temp] = Pos[i-1] + Pos[Temp]$
13:          $overlap \leftarrow$ **False**
14:          **for** $j = 0 \rightarrow i - 1$ **do**
15:            $R2 \leftarrow distance(Pos[i], Pos[j])$
16:            **if** $R2 \leq d$ **then** $\triangleright$ d denotes the polymer bondlength
17:              $KK = KK + 1$
18:              $overlap \leftarrow$ **True**
19:            **end if**
20:          **end for**
21:          **if** $\neg overlap$ **then**
22:            $Pos[i] = Pos[Temp]$
23:          **end if**
24:        **end for**
25:       $p = p * (1.0 - kk/ptMax)$
26:      **end for**
27: **end function**
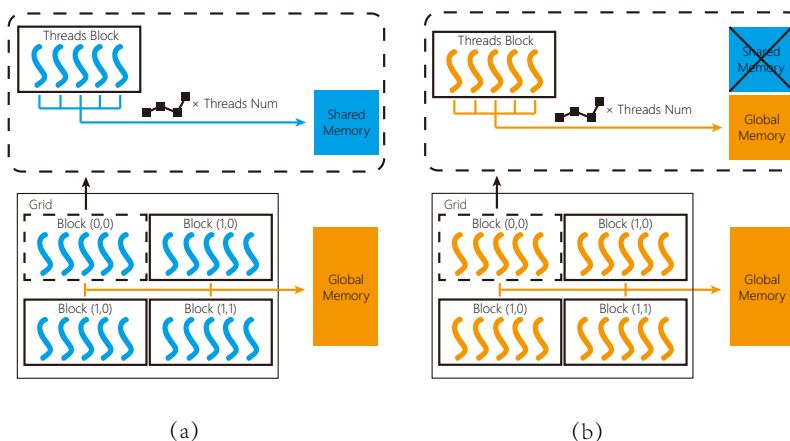
Figure 2: Memory structure and data flow between global memory, shared memory and threads of GPU.

own statistically uncorrelated conformation of the molecule using the Rosenbluth algorithm. All the data are stored in the shared memory during the generation process. The data in the shared memory can also be used on the fly: data is processed directly and then discarded. Alternatively, It can also be saved to the global memory on GPU and later copied back to CPU.

On the other hand, since all coordinates are stored in shared memory during the SAW process, high consumption of shared memory may greatly affect the occupancy of the program. Therefore, we propose another data flow as shown in Figure 2b where all coordinates are stored not in shared, but in global memory. This is the case for generating relatively long molecules.

4   Result and discussion

4.1   Static properties of polymer melts

As an example of accuracy and efficiency of the method, we investigated classical properties of polymer melts. The averaged squared extension, R^2, of the chain is calculated for all the chains generated and compared as a function of N. R^2 is also known as end-to-end distance[24] which is of importance in calculating the properties such as viscosity of the polymer chains.

For a diluted solution of polymer chains the dependence of this quantity on the number of monomers in the chain is given by:[25]

$$\left\langle R_N^2 \right\rangle = a N^{2\nu} \tag{6}$$

where the proportionality constant a depends on the structure and on external conditions such as the solvent used in the chemical solution or temperature; critical exponent ν is universal, and depends only on the dimension of space.

We calculated R^2 in the case of both lattice and off-lattice versions with various values of N up to 64 in three dimensions. Results are shown in Figure 3, and compared with previous studies. We find that the critical exponent ν for lattice model is 0.601, and 0.588 for off-lattice model. The above results give a remarkably good match in entire range with Ref. 26.

We also performed series of simulation to test our code to calculate the partition function of the linear polymers Z_N with scaling arguments of SAW. A general superscaling expression for partition function of the system of length N is given by[27]

$$Z_N \sim \mu^N N^{\gamma-1} \tag{7}$$

where μ is a model dependent connectivity constant and γ is the universal entropic exponent. Consider a sample of $\aleph$ configurations of polymers with length N, $(s_1, s_2, ..., s_\aleph)$ and corresponding Rosenbluth weights $(W(s_i))$. Then
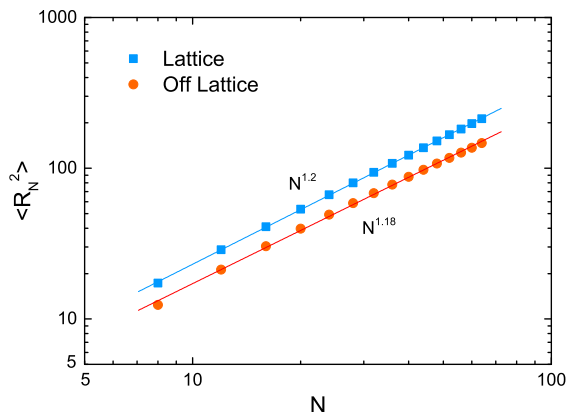
Figure 3: R^2 End-to-end distance of a polymer chain as a function of polymer chain length N.

Z_N is estimated as

$$Z_N \approx \langle W_N \rangle_\aleph = \frac{1}{\aleph} \sum_{i=1}^{\aleph} W(s_i) \qquad (8)$$

Taking logarithm of both sides of eq 7 we can get an estimate for exponent $\gamma - 1$ and constant μ:

$$\log(Z_N) \sim N \log(\mu) + (\gamma - 1)\log(N) \qquad (9)$$

We performed series of simulation in 3D lattice space and find a best estimate $\mu = 4.6856$ and $\gamma = 1.1592$ which is in a good agreement with previous studies[28–30] . The results are summarized in Table 1.

Table 1: Comparison of SAW exponents in 3D lattice space between values from literature and obtained from static MC simulation performed on GPU

	Literature values	Static MC Simulation
γ	1.1608^{28}	1.1592 ± 0.0006
ν	0.5877^{29}	0.5880 ± 0.0001
μ	4.684^{30}	4.6856 ± 0.0001

4.2 Performance

In order to compare the validity and the performance of our GPU implementation, we implemented a sequential CPU version of the same algorithm. Similar to the GPU realization, we use the single precision for the calculations.

Table 2: Comparison of performance between CPU and GPU of generating 1 million conformation in 3D lattice space

N	Time for 10^6 chain / s		Accleration
	GPU	CPU	
4	0.00676	12.848	1900.592
8	0.01789	31.267	1747.736
16	0.06670	88.854	1332.144
24	0.17810	132.406	743.436
32	0.41466	192.643	464.580
48	1.19394	342.454	286.826
64	3.17465	546.526	172.153

Table 3: Comparison of performance between CPU and GPU of generating 1 million conformation in 3D real space

N	Time for 10^6 chain / s		Accleration
	GPU	CPU	
4	0.20985	36.023	171.6607
8	0.5912	94.344	159.5805
16	2.98727	259.478	86.86125
24	8.62754	516.037	59.81276
32	26.19131	655.682	25.03433
48	87.71847	1228.625	14.00646
64	315.14837	1967.912	6.244398

A direct comparison between CPU and GPU of both lattice and off-lattice version is presented in Tables 2 and 3. We define a speed-up factor as follows: tCPU is the execution time on a single CPU core and tGPU is the runtime on the GPU. The run contains one million sampling generated with different number of monomers completed either on NVIDIA Tesla K80 GPU or Intel i5-3320m CPU. For the lattice space, we find that GPU outperforms the single CPU as 1900 times for smallest chain lengths. With growing length, the efficiency gradually decreases. The decrease comes mainly from the increasing consumption of the

Table 4: Hardware configurations for benchmarks test

	K80	K20	GT 730
GPU	K80	K20	GT 730
Stream Processors	2 x 2496	2496	384
Core clock	562 MHz	706 MHz	902 MHz
Memory clock	5 GHz	5.2 GHz	5.0 GHz
DRAM	2 x 12 GB GDDR5	5 GB GDDR5	1 GB GDDR5

shared memory of each block. However, CPU still outperform CPU as a factor of 172 for a polymer with 64 monomers.

The speedup ranges between 171 and 6 for the chain length from 4 to 64 for off-lattice version. This is because MC process of calculating Rosenbluth weight brings a large divergence to the code (for example, "if" statements).

We also tried to test the code on different GPUs for benchmarks. The technique details between different benchmarks are summarized in Table 4 and the comparison of performance is presented in Figure 4. The performance is evaluated as the number of chains generated per second.
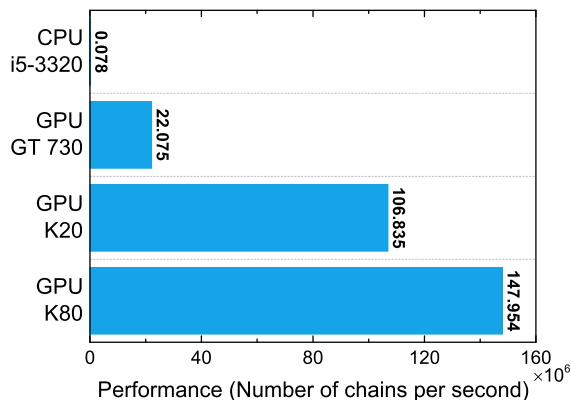
Figure 4: Comparison of the average number of chains generated each second between different benchmarks. The hardware details is presented in Table 4

With new NVIDIA Pascal architecture, the shared memory is increased due to the larger number of Stream Multiprocessor (SM) count, and aggregate shared memory bandwidth is effectively more than doubled. A higher ratio of shared memory, registers, and warps per SM is introduced to the new benchmark GP100 which allows the SM to more efficiently execute code. The bandwidth per-thread to shared memory is also increased. All these features will increase the performance of our implementation.

5   Conculsion

We developed highly efficient parallel GPU implementation of the Rosenbluth Algorithm of generation of self-avoiding random walks on lattice and in real space. Both versions of the code have the same accuracy compared with a single core CPU implementation, but give huge performance improvement in simulation efficiency making the generation process almost perfectly parallelizable. The corresponding patent is filled.[31] As a result, the realization of the algorithm on modern GPUs outperforms a serial CPU implementation at maximum by 1900 times. It is limited by the number of CUDA cores and the size of shared memory, thus one can expect further increase of efficiency with future development of GPU architecture.

The parallel GPU implementation of the algorithm was applied to static MC simulation of polymer chain having the same precision as CPU version.

The implementation breaks the performance bottleneck of existing molecular conformation generating methods, significantly improving the parallel performance, and has broad application prospects in the static MC simulations.

References

(1) Frenkel, D.; Smit, B. *Understanding Molecular Simulation: from Algorithms to Applications*; Academic Press: San Diego, 2002.

(2) Leach, A. R. *Molecular Modelling: Principles and Applications*; Pearson Education, 2001.

(3) Muller, M.; Katsov, K.; Schick, M. *Physics Reports* **2006**, *434*, 113–176.

(4) Alder, B. J.; Wainwright, T. E. *The Journal of Chemical Physics* **1959**, *31*, 459–466.

(5) Sutter, H.; Larus, J. *Queue* **2005**, *3*, 54–62.

(6) Hwu, W.-m.; Keutzer, K.; Mattson, T. G. *IEEE Design & Test of Computers* **2008**, *25*, 312–320.

(7) Owens, J.; Houston, M.; Luebke, D.; Green, S.; Stone, J.; Phillips, J. *Proceedings of the IEEE* **2008**, *96*, 879–899.

(8) Januszewski, M.; Kostur, M. *Computer Physics Communications* **2010**, *181*, 183–188.

(9) Rapaport, D. C. *Computer Physics Communications* **2011**, *182*, 926–934.

(10) Nedelcu, S.; Werner, M.; Lang, M.; Sommer, J. U. *Journal of Computational Physics* **2012**, *231*, 2811–2824.

(11) Komura, Y.; Okabe, Y. *Journal of Computational Physics* **2012**, *231*, 1209–1215.

(12) Anderson, J. A.; Lorenz, C. D.; Travesset, A. *Journal of Computational Physics* **2008**, *227*, 5342–5359.

(13) Rosenbluth, M. N.; Rosenbluth, A. W. *The Journal of Chemical Physics* **1955**, *23*, 356–359.

(14) Kruskal, W. H.; Mosteller, F. *Encyclopedia of Statistical Sciences*; John Wiley & Sons, Inc., 2004.

(15) Matsumoto, M.; Nishimura, T. *ACM Trans. Model. Comput. Simul.* **1998**, *8*, 3–30.

(16) L'Ecuyer, P. *Commun. ACM* **1990**, *33*, 85–97.

(17) Park, S. K.; Miller, K. W. *Commun. ACM* **1988**, *31*, 1192–1201.

(18) Nickolls, J.; Buck, I.; Garland, M.; Skadron, K. *Queue* **2008**, *6*, 40–53.

(19) Farber, R. *CUDA Application Design and Development*; Elsevier, 2011.

(20) Lüscher, M. *Computer Physics Communications* **1994**, *79*, 100–110.

(21) O'connor, B. P. *Behavior Research Methods, Instruments, & Computers* **2000**, *32*, 396–402.

(22) Metropolis, N.; Rosenbluth, A. W.; Rosenbluth, M. N.; Teller, A. H.; Teller, E. *The Journal of Chemical Physics* **1953**, *21*, 1087–1092.

(23) CUDA Toolkit. https://developer.nvidia.com/cuda-toolkit.

(24) Flory, P. J. *Principles of Polymer Chemistry*; Cornell University Press, 1953.

(25) Doi, M.; Edwards, S. F. *The Theory of Polymer Dynamics*; Clarendon Press, 1988.

(26) Gould, H.; Tobochnik, J.; Christian, W. *An Introduction to Computer Simulation Methods: Applications to Physical Systems*; Pearson Addison Wesley, 2007.

(27) Duplantier, B. *Journal of Statistical Physics* **1989**, *54*, 581–680.

(28) Grassberger, P. *J. Phys. A: Math. Gen.* **1993**, *26*, 2769.

(29) Hsu, H.-P.; Nadler, W.; Grassberger, P. *Macromolecules* **2004**, *37*, 4658–4663.

(30) Clisby, N.; Liang, R.; Slade, G. *J. Phys. A: Math. Theor.* **2007**, *40*, 10973.

(31) Guo, Y.; Baulin, V. A. *A computer im-
plemented method of generation of statis-
tically uncorrelated molecule's conforma-
tions and computer programs*; EP Patent
16,382,054, 2016.

6

PREDICTED COPOLYMER SEQUENCE TRANSLOCATING VIA COMPLEX ENERGY BARRIERS
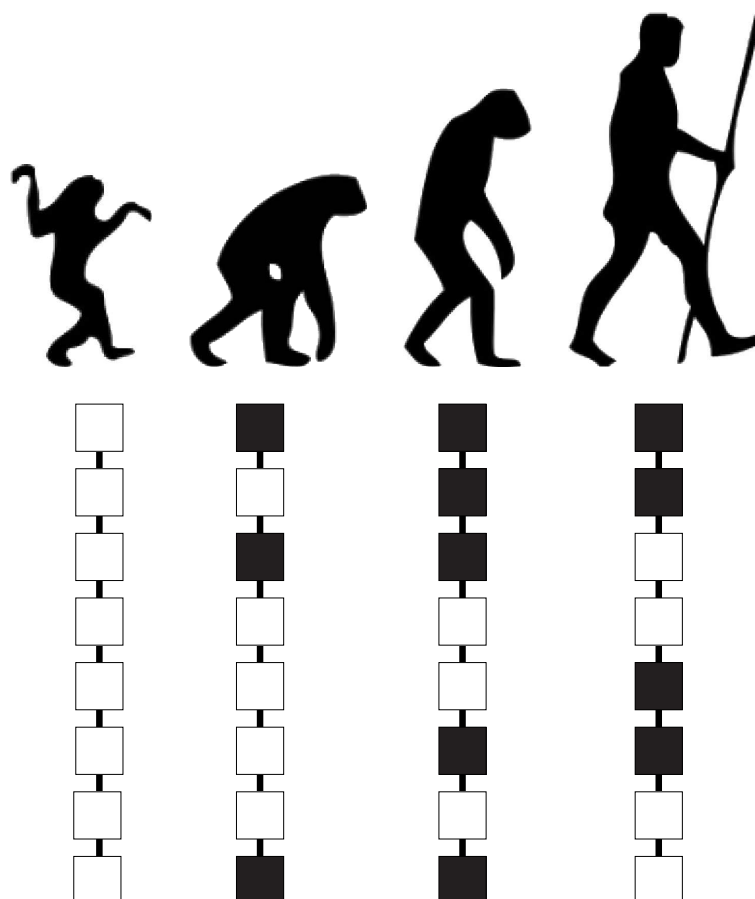
Predicted copolymer sequence minimizing translocation time through complex energy barriers

Yachong Guo, Marco Werner, and Vladimir A. Baulin*

Departament d'Enginyeria Química, Universitat Rovira i Virgili 26 Av. dels Paisos Catalans, 43007 Tarragona Spain

(Dated: April 27, 2016)

We report a computational tool providing relatively fast and stable solution based on the spirit of Single Chain Mean Field (SCMF) theory in different geometries and different molecule structures. Benefited from the speed up by the implementation of Rosenbluth Chain Generation Method on GPU, we are able to perform series of Static Monte Carlo simulation combined with mean field theory studying the copolymer sequence minimizing translocation time through complex energy barriers. We find that the translocation behaviour can be greatly strengthened with ordered distribution of sequence pattern.

Usage: Secondary publications and information retrieval purposes.

PACS numbers: May be entered using the \pacs{#1} command.

Structure: You may use the description environment to structure your abstract; use the optional argument of the \item command to give the category of each item.

CONTENTS

I.   METHOD

We use the (single chain mean field) SCMF with an implicit solvent to simulate lipid bilayer membranes interacting with heteropolymers such as random A/B polymers (RCP). The simulation model represents a coarse-grained view on flexible polymers where the monomer unit represent a few chemical monomers.

Figure 1 shows the connectivity of the polymers used in our simulation. The polymers are embedded into an external field $V(z)$, which in our case implements a one-dimensional representation of a bilayer membrane composed of an hydrophilic region (h), and a hydrophobic core (t), see Fig. 1-A. The interaction potential is described in Fig. 1-C, The external potential is given by $V_{P0}(z) = (1 - H_S)\varepsilon_0\theta(z - d/2)\theta(z + d/2)$ and $V_{P1}(z) = H_S(1 - \theta(z-d)\theta(z+d/2))$, where θ is the Heaviside function, and d is the bilayers's thickness chose as $d = 6$ in our case.

We sample by using Rosenbluth method the conformations and evaluate in the mean field than calculate the Hamiltonian of each chain in the field with GPU technique. We note here, that the typical computing time for a single chain set as shown in Fig 5 was on the order of 20 to 25 days (depending on chain length and ratio) using a single thread of an Intel Core i5-3320 processor. Here, we have implemented the parallelized versions of SCMF can benefit from modern graphics card technologies by an up-speed of up to 2000 compared to the single thread on the CPU. Free energy along Z direction can then be calculated out of the partition function. Then we substitute into the equation 13 to achieve the mean first escape time τ which describe the polymer translo-
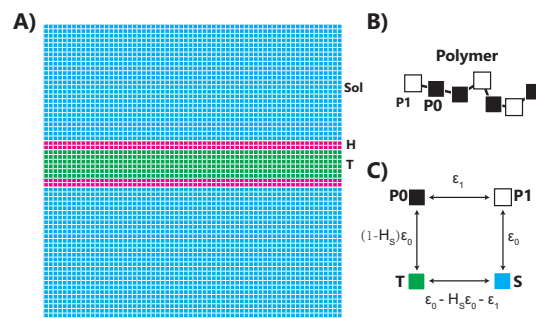
FIG. 1. A)Schematic plots of the simulation box the representation of lipids, solvent and Schematic illustration of the simulation model used: B) coarse grained representation of polymer chains as used in our simulations, C) attractive interactions between the four components as defined .)

cation behaviorr. Fig. 2 illustrates one example of the calculation, on the left is the sorted τ as a function of chain sequence number of a 16 monomer polymer chain at ratio of 50% in total of 12870 different combination, corresponding to the visualization of different chain pattern on the right.

The theory we applied is an special example of the single chain mean field (SCF) method where a single chain is described at the molecular level while the interactions between different chains are described through a mean molecular field which is found self-consistently. In the present, we remove the self consistent procedure and the concentration is given in the beginning. A number of possible conformations of a polymer is generated with Self-Avoiding walk. Each conformation is then weighted in the given mean-field. In this case, the interaction between molecular are treated on a mean-field level. Once the probability distribution function is known, any thermodynamic property of interest of the polymer can be

2
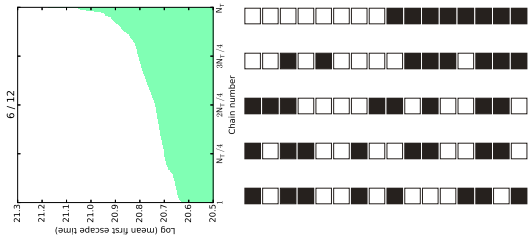
FIG. 2. Left) Sampling results for the mean first escape time τ, of polymer chain of length 16 as a function of the chain number at the ratio 50%(T/(H+T)). Right)Selected polymer pattern representing different translocation strength τ.

obtained.

$$F = -\langle S \rangle + \langle H \rangle \tag{1}$$

where $\langle \ldots \rangle = \int \ldots \rho d\rho$ is the strong correlation between molecules are decoupled, the pdf ρ of the many component system factorizes into the product of single polymer pdfs $\rho(\Gamma)$

$$\rho = \prod_{\alpha=1}^{N} \rho_\alpha (\Gamma_\alpha) \tag{2}$$

The entropy term in the expression 1 is written as

$$\langle S \rangle = \int c(\Gamma) \ln \frac{c(\Gamma)}{e} \Lambda^{3N} d\Gamma + \int \frac{dr}{V} c_s(r) \ln \frac{c_s(r)}{e} \Lambda_s^3 \tag{3}$$

where $c_s(r)$ is the concentration of solvent molecules, the spatial integration is over the volume of the box V, while Λ^{3N} and Λ^3 are the de Broglie lengths of the beads of polymer. Since the correlations between the chains are decoupled, the distribution function of conformations $P(\Gamma)$, via $c(\Gamma) = NP(\Gamma)/V$. The interactions of the beads inside a given conformation, $u_{intra}(\Gamma)$, can be decoupled from the interactions with the fields. Thus, $u(\Gamma)$ can be written as:

$$\langle H \rangle = \int c(\Gamma) u(\Gamma) d\Gamma \tag{4}$$

$$u(\Gamma) = u_{intra}(\Gamma) + \frac{N-1}{2} \int \frac{dr}{v} P(\Gamma') \widehat{u}(\Gamma, \Gamma', r) d\Gamma'$$
$$+ \int \frac{dr}{V} c_s(r) u(T, r) \tag{5}$$

where $\widehat{u}(\Gamma, \Gamma', r)$ describes the interactions with the beads of other molecules of conformation Γ' and $u(T, r)$ describes the interactions with the solvent. The factor

1/2 avoids double counting and (N-1) is due to the separate intra-molecular part.

In the following, we consider a polymer consist of only two type of beads: Hydrophilic, H and hydrophobic, T. In the case of more complex structure, the equations are easily generalized. Introducing three interaction parameters: between hydrophobic beads and solvent, ϵ_{TW}, between hydrophilic beads, ϵ_{HW} and between hydrophilic beads and hydrophobic beads, ϵ_{HT}, the interaction energy yields.

$$u_{intra}(\Gamma) = u_{intra}(\Gamma) + \frac{N-1}{2} \varepsilon_{HT} \int dr [\phi_{int}^H(\Gamma, r) \langle C_T(r) \rangle$$
$$+ \phi_{int}^T(\Gamma, r) \langle C_H(r) \rangle] + \varepsilon_{TW} \int dr \phi_{int}^T(\Gamma, r) c_s(r)$$
$$+ \varepsilon_{HW} \int dr \phi_{int}^H(\Gamma, r) c_s(r) \tag{6}$$

where $\phi_{int}^H(\Gamma, r)$ and $\phi_{int}^T(\Gamma, r)$ are the interaction fields of each conformation in a given position in space.

combined with the incompressibility condition, as

$$\phi_s(r) = 1 - N \langle \phi(r) \rangle \tag{7}$$

Minimize the free energy, we have

$$\mathcal{H}(\Gamma) = u_{intra}(\Gamma) + (N-1) \varepsilon_{HT} \int dr [\phi_{int}^H(\Gamma, r) \langle C_T(r) \rangle$$
$$+ \phi_{int}^T(\Gamma, r) \langle C_H(r) \rangle] + \varepsilon_{TW} \int dr \phi_{int}^T(\Gamma, r) c_s(r)$$
$$+ \varepsilon_{HW} \int dr \phi_{int}^H(\Gamma, r) c_s(r)$$
$$- \int dr \frac{\phi_{ex}(\Gamma, r)}{v_s} \ln \phi_s(r) \tag{8}$$

$$Z = \sum_k e^{-\mathcal{H}(\Gamma)} \tag{9}$$

$$F = k_B T \ln(Z) \tag{10}$$

$$e^{-\mathcal{H}(\Gamma|z)} = e^{-(\mathcal{H}(\Gamma|z_1) + \mathcal{H}(\Gamma|z_2) + \mathcal{H}(\Gamma|z_3) + \ldots \mathcal{H}(\Gamma|z_n))} \tag{11}$$

$$F(z_n) = k_B T \ln(Z(z_n)) \tag{12}$$

In our method, statistical segments of chain like molecules are represented as connected unit cubes on a simple cubic lattice. The distance between bonded monomers is constraint to a bond vector set of 26 bond vectors by (1,0,0),(1,1,0),(1,1,1). The excluded volume

TABLE I. Statistics analysis of chainlength 12 with different ratio

T	Ra	Best				Worst			
		N_T	S_T	N_H	S_H	N_T	S_T	N_H	S_H
0	0%	1.00	12.00	0.00	0.00	1.00	12.00	0.00	0.00
1	8%	1.67	6.60	0.83	1.00	1.83	5.91	1.00	1.00
2	17%	1.83	5.45	1.67	1.00	2.17	4.46	1.67	1.20
3	25%	2.33	3.86	2.17	1.15	2.00	4.42	1.67	1.80
4	33%	2.83	2.82	2.67	1.13	1.67	4.80	1.67	2.40
5	42%	3.33	2.10	3.33	1.20	1.67	4.20	1.67	3.00
6	50%	4.67	1.07	5.00	1.20	1.67	3.60	1.67	3.60
7	58%	3.67	1.09	3.67	1.91	1.67	3.00	1.67	4.20
8	67%	2.67	1.13	2.83	2.82	1.67	2.40	1.67	4.80
9	75%	2.50	1.00	2.83	3.12	1.50	2.00	2.00	4.50
10	83%	1.83	1.00	2.17	4.38	1.67	1.10	2.33	4.29
11	92%	1.00	1.00	1.67	6.50	0.83	1.00	1.83	6.00
12	100%	0.00	0.00	1.00	12.00	0.00	0.00	1.00	12.00

Note: T Number of P0 in the chain
Ra Ratio of P0 in polymer chain Ra=(P0/(P0+P1)) N_T: Average T block number
S_T: Average T block size
N_H: Average H block number
S_H: Average H block size

TABLE II. Statistics analysis of chainlength 8-16 with same ratio 50%

T	N	Best				Worst			
		N_T	S_T	N_H	S_H	N_T	S_T	N_H	S_H
4	8	3.00	1.06	3.17	1.21	1.67	2.40	1.67	2.40
5	10	3.67	1.09	3.67	1.36	1.67	3.00	1.67	3.00
6	12	4.67	1.07	5.00	1.20	1.67	3.60	1.67	3.60
7	14	5.33	1.22	5.00	1.30	1.67	4.20	1.67	4.20
8	16	5.50	1.30	6.00	1.31	1.67	4.80	1.67	4.80

Note: T Number of P0 in the chain
N:Polymer chain length
N_T: Average T block number
S_T: Average T block size
N_H: Average H block number
S_H: Average H block size

is implemented via the exclusion of overlap between monomer on the same lattice site. We apply short range thermal interactions between monomers of species P0 and T, P1 and S associated with the interaction constants $\epsilon_0 = -1, \epsilon_1 = -1$ in unit of $k_b T$ If the chain is full of P0 it will be fully hydrophobic and prefer to stay in T region. If is full of P1 it will be fully hydrophilic and stay in solvent region

The mean first escape time of the polymer can be achieved through the free energy profile as shown in Fig.9 between two boundaries $[z_-, z_+]$, where we define z_- as the bottom of the simulation box and z_+ as the top of the simulation box.

$$\tau_{te} \propto \int_{z_-}^{z^+} dz' e^{F(z')/k_B T} \int_{z_-}^{z'} dz'' e^{-F(z'')/k_B T} \quad (13)$$

We choose $N_p = 12$ and present the sorted mean escape time with all possible combination of H and T monomer and selected polymer pattern in Fig.3. The total number of pattern for each hydrophobicity (T(H+T)) can be calculated exactly through $N_T = C_{H+T}^T$. The plots is colored with different fraction of T beads in the chain. The series plot show that the translation behavior is quite sensitive to the pattern of polymer, at 50% we find largest gap between minimum and maximum value. With the fraction getting increased or decreased, the gap become more and more weak. The affect of the pattern to the mean first escape time is much more obvious for the best ratio to translocate compared with other ratios.

The selected each three pattern with minimum and maximum of mean escape time is presented in Fig.3. The results readily gives out the info that with a huge pattern gather together, it is less efficient than an regular

and more symmetrically patterned polymer. To define the characters and distinguish is a complexed issue and cloud look into from different aspect. Therefore we studied several properties of the pattern: The average block number and block size of $P0$ and $P1$. we select the 10 best and worst blocks of the MFET(Mean first escape time), The average block number is calculated by counting all blocks and get average. while the average block size is calculated by measuring the block size and then calculate the average. The results are summarized in Table. I. There is a significant difference of the block number and the block size between the two groups. The block number of the best group is much higher than the worst group. However, for the block size is opposite. Compared with the best group, both the block number and size changes steadily for the worst group with different ratio, especially for the block number, we find the value is generally around 1.67. which means that for the worst translocation, the average block number is around 3 blocks, and the size is quite big. On the other hand, in the case of the best translocation group. The average block number and size shows a correlation with the ratio. A peak for the block number was find at 50%. However, for the best translocation case we find that the block prefer to be as small as possible. In conclusion, for the best group, the block size shows a preference of being as small as possible and thus the number is relative high. For the worst group it is opposite.

We also compare the MFET of the same ratio but between different chain length. The results are summarized in Fig. 4. There is a linear dependence $y = a*x^b$ between log(MFET) and chain length. The two lines reveals the upper(worst) value (fitting curve $log(\tau) = 1.30 + 0.100$) and lower(best) (fitting curve $log(\tau) = 1.60+0.077$) value of log(MFET), the gap between the upper and lower value increase with the chain length, that is, the affect of the pattern increased with the total chain length.

The selected each three pattern with minimum and maximum of mean escape time is presented in Fig.5. The results shows a similar behavior as in Fig. 3: for the max translocation group the pattern is big and unsymmetrical, for the min group the pattern tend to be more regular

4
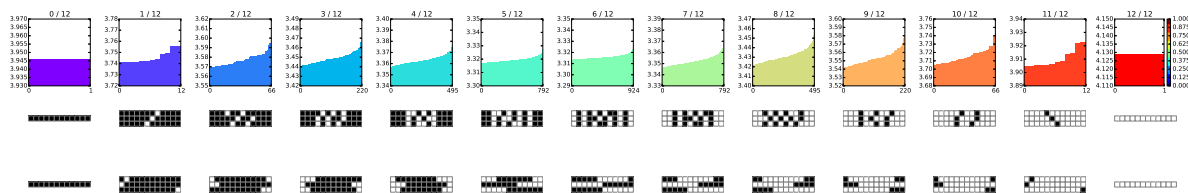
FIG. 3. Top:The mean escape time τ of the polymer as a function of polymer chain sequence number. We show results for various polymer fraction (P0/(P0+P1)) ranging from 0% to 100% of the polymer consist of 12 monomers. Middle: Polymer monomer pattern of the three minimum mean escape time Bottom: Polymer monomer pattern of the three maximum mean escape time
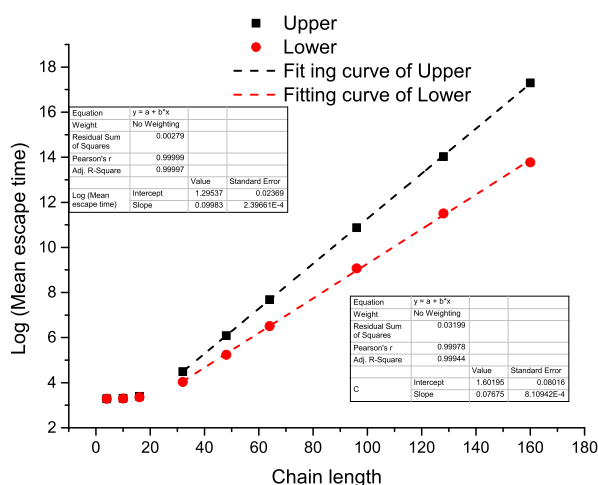
FIG. 4. Top:The maximum and minimum value of mean escape time (log)as a function of different polymer monomer (chain length from 8 to 16 increase by 2) for the same fraction (T/(H+T)) of 50%. And their fitting curve

and in ordered sequence.

The statistics analysis of the pattern is summarized in Table. II. For the best group, there is a positive dependence between the tail number and the average block number. The T block size is quite small ranging between 1.06 and 1.30, we do find out the there is a tendency of increase. The block size of H is slightly bigger than T with the range between 1.20 and 1.36. On the other hand, for the worst group, the average block number are all 1.67 with an average of 3 total blocks, there fore the

block size is quite big. In conclusion, with a changing length, the the block size also shows a preference of being as small as possible and thus the number is relative high. For the worst group it is opposite. And there is a increasing trend for the block size with the grow of the chain length for the best translocating group.

Fig. 6 reveals a 3D illustration of the log minimum mean escape time $log(\tau)$ for different chain length (8-14) at all possible hydrophobicity. We can find that all
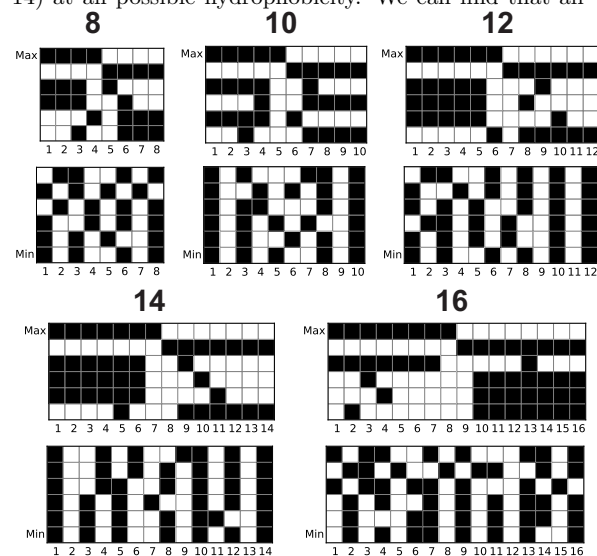
FIG. 5. We present the top and last six polymer monomer pattern of the mean escape time.

different chain length share the same minimum of τ at 50%. And rest hydrophobicity increase linearly.

5
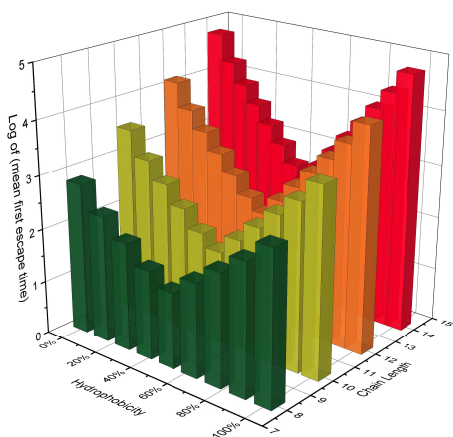
FIG. 6. 3D plots of the mean escape time τ as a function of the polymer chain hydrophobicity (0%-100%) and the chain length (8-14)

7

MICRO-BLADES KILL BACTERIA MECHANICALLY
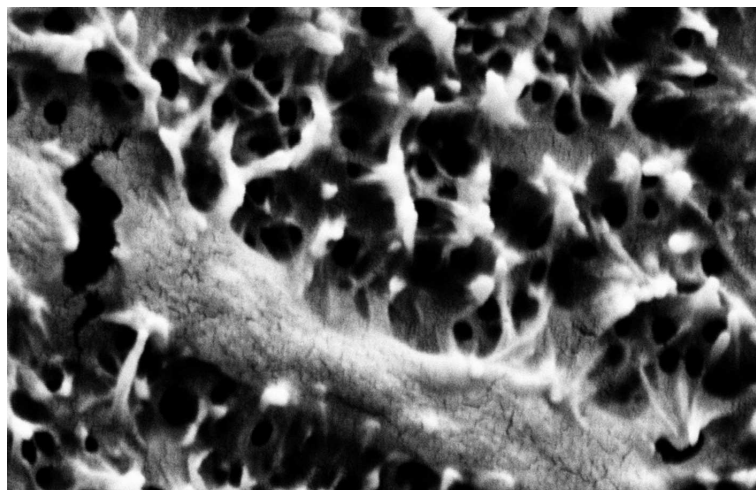
WILEY-VCH

Micro-blades assembled on highly-ordered pyrolytic graphite kill bacteria mechanically

Song Ha Nguyen#, Yachong Guo#, Vladimir A. Baulin, Hayden K. Webb, Christopher J. Garvey, David E. Mainwaring, Peter J. Mahon, Russell J. Crawford, and Elena P. Ivanova*

Dr. S. H. Nguyen, Dr. H. K. Webb, Prof. D. E. Mainwaring, Dr. P. J. Mahon, Prof. R. J. Crawford, Prof. E. P. Ivanova
School of Science, Swinburne University of Technology, P.O. Box 218, Hawthorn, 3122, Australia
E-mail: eivanova@swin.edu.au
Y. Guo, Dr. V. A. Baulin
Department d'Enginyeria Quimica, Universitat Rovira i Virgili, 26 Av. dels Paisos Catalans, 43007 Tarragona, Spain
#These authors contributed equally.
Dr. C. J. Garvey
Bragg Institute, Australian Nuclear Science and Technology Organisation, Locked Bag 2001, Kirrawee DC NSW 2232

Over the past several decades, there has been considerable effort towards the fabrication of novel antibacterial materials.[1-3] One common approach is to functionalise existing materials with antibacterial agents such as polycations, silver and antimicrobial peptides (AMPs). Recent developments have seen the emergence of mechanobactericidal surfaces, which are capable of killing bacteria through the physical interactions that take place between the substratum topography and the bacterial cells.[4] To date, these surfaces have been primarily insect wings (e.g. cicada and dragonfly), however the bactericidal effect observed on these natural surfaces has now been replicated on the surface of plasma-etched silicon.[4]

Biomimetic design has become an important emerging field in the design of functional surfaces. The ability of plants, insects, and other organisms to maintain surfaces free from contamination has provided this guidance.[5-9] Recent research on insect wings has shown that they do not always simply repel potential contaminants, but can actively kill bacterial cells that seek to colonise the surface.[4, 10, 11] The wings of the

1

WILEY-VCH

Hemianax papuensis dragonfly, for example, are known to be highly efficient at inactivating *Pseudomonas aeruginosa* cells (Figure S1), a cause of nosocomial infections, for which multidrug resistance is emerging. The wing surface structures are composed of various lipid molecules, which are predominantly a mixture of fatty acids and *n*-alkanes. Compounds such as these may be suitable for use in designing novel model biomaterials that are able to replicate this surface structure, and therefore its mechanobactericidal activity.

To date, all of the mechanobactericidal surfaces that have been identified have been shown to possess complex surface features that are able to rupture and lyse bacterial cells.[4, 10, 11] These surfaces usually possess high aspect ratio nanopillars with a well-defined spatial hierarchy. The process of surface templating may allow the assembly of similar complex three-dimensional structures as lipid films on well-ordered substrata. Highly-ordered pyrolytic graphite (HOPG) provides such a surface, allowing it to be employed for precise molecular assembly. Fatty acids have previously been shown to align very closely with graphite sheets when forming two-dimensional films on their surface.[12-17]

The aim of this work was to investigate the three-dimensional structure of palmitic and stearic acids films when re-crystallised on the surface of HOPG. In evaluating these films, they were found to exhibit mechanobactericidal behaviour that was similar to that observed for the dragonfly wings. The simplicity of their production suggests a fabrication technique that may be effectively applied to form single-use bactericidal nanocoatings.

Three-dimensional films of palmitic and stearic acid were produced by dissolution of these fatty acids in chloroform, followed by their deposition onto freshly peeled thin layers of graphite. The chloroform was then allowed to evaporate, allowing the fatty acid structures to form spontaneouly. These were subsequently characterised and evaluated for their antimicrobial behaviour. The three-dimensional structures of both fatty acids resulting from this deposition are given in Figure 1. The assembly of palmitic acid on the HOPG surface resulted in the formation of blade-like structures, typically $1 - 2$ μm in length, while the stearic acid formed broader, shorter structures that appeared less sharp at the upper contact plane. It is well established that self-assembled monolayers formed from fatty acids can adopt various states of crystallinity, the structure of which is also dependent on temperature and humidity.[12, 13, 18] Synchrotron grazing incidence diffraction (GID) images of palmitic acid, stearic acid and the HOPG substrate are shown in Figure 1C, together with the sector averages measured at -90 ± 5 °, which are largely free of the peaks that are characteristic of the HOPG substrate. These peak positions indicate that both the palmitic and stearic acid crystallised in the C-crystal form.[19] In each case, the 001 reflection and the higher order peaks (00n) are not observable in the GID, which is consistent with the stacking of fatty acid molecules approximately parallel to the HOPG substrate. It is

2

WILEY-VCH

important to note that all of the other observable reflections exhibited an isotropic azimuthal intensity distribution. Together, these observations indicate that the crystallites observable in the atomic force microscope (AFM) images were crystallographically oriented with respect to the substratum surface, but isotropically oriented in a direction normal to the surface.

Atomic force microscopy images and cross-sectional profiles of AFM scans (Figure 2A) confirmed that the palmitic acid microblades were sharply lenticular in comparison to the stearic acid structures, which tended to be flatter across the peaks. The morphology of these microblades was then examined by transferring the AFM data to Gwyddion software,[20] which was used to compare the distribution of axial ratios of the palmitic and stearic acid crystallites (for features >200 nm) which showed the sharpness of the palmitic acid (Figure S2).

The AFM topological profiles were analysed using a statistical method based on the vision detection algorithm reported by Chen et al.[21], as detailed in the Experimental Section. Figure 2B shows this process where initially detected local peaks (circles) were grouped as clusters (ellipses) which were then analysed by the vision detection algorithm as two-dimensional images estimating the dimensions and morphology of each surface. Figure 3A shows these re-constructed images as computed AFM cross-sectional profiles together with three characteristic dimensions when modelled as a trapezoid (Figure 3B). Finally, the comparative statistical distribution of these parameters shows the differences in dimension and number density between the palmitic and stearic acid microcrystals (Figure 3C). The computed AFM data was then compiled as two-dimensional lateral projections (Figure S3), where they indicate the complexity of both palmitic and stearic acid micro-structures in this plane. The computed three-dimensional architecture clearly shows the sharpness of the palmitic acid crystallites compared to their stearic acid counterparts, consistent with the directly measured AFM profiles (Figure 2A).

Figure S4 represents statistical comparison of the shapes of palmitic and stearic acid crystals, namely, it shows the deviations from circular shape. Aspect ratio is defined as the ratio between minor and major axes. Statistical analysis shows that stearic acid crystals have significantly less circular shaped peaks (aspect ratio 1) due to lower peak density (Table 1). In turn, the number of highly asymmetrical peaks (aspect ratios < 1/2) is larger for palmitic acid crystals, while stearic acid crystals have more symmetric peaks (aspect ratios > 1/2). Thus, the main difference between two types of acid crystals is larger density of peaks of palmitic acid crystals and more asymmetrical shapes of palmitic acid crystals. These two parameters may contribute to higher bactericidal activity of palmitic acid crystals.The antibacterial potential of these self-assembled fatty acid structures was assessed by monitoring the viability profiles of two model pathogenic bacteria: *Pseudomonas*

WILEY-VCH

aeruginosa and *Staphylococcus aureus*. *P. aeruginosa* is an opportunistic pathogen, which can commonly infect immune-compromised individuals, particularly in the respiratory tracts of patients with cystic fibrosis.[22-24] *S. aureus* (colloquially known as 'Golden staph') regularly establishes persistent infections of implants and post-operative wound sites.[25-28] Both *Pseudomonas aeruginosa* and *Staphylococcus aureus* bacteria can cause serious complications to existing medical conditions and threaten lives. Each bacterium has a different morphology and cell wall structure. *P. aeruginosa* cells are rod-shaped, and have a thinner layer of peptidoglycan in their cell wall than do the spherical *S. aureus* bacteria. These factors are important considerations in characterising mechanobactericidal surfaces, as the mechanical properties of the cells that interact with a surface will profoundly influence their susceptibility to physical antibacterial action.[29] Previous work has indicated that the more compliant *P. aeruginosa* cells are more sensitive to the mechanical stresses applied by nanoscale surface asperities than the *S. aureus* cells.[4, 10, 11, 29] Figure 4 illustrates the bactericidal activities of these two surfaces, as determined by CSLM imaging, together with the ratios of dead to live cells, as determined by pixel counting at the respective wavelengths. Here it can be seen that the palmitic acid micro-blade structures were markedly more active than the stearic acid microstructures, and the *S. aureus* cells appeared to be more susceptible to rupture than were *P. aeruginosa* cells, despite having a thicker cell wall and requiring a larger force for extension.[30] Importantly, both fatty acid films proved to be considerably bactericidal relative to the smooth HOPG controls (Figure S5).

Notably, an increase in the alkane chain of two CH_2 units yielded very different self-assembled patterns on the HOPG as well as very different bactericidal activities. This suggests that microblade curvature plays an important role in the interaction of the bacterial cells with these microstructures. It has been shown that the adsorption of *P. aeruginosa* cells onto the mechanobactericidal nanopillar arrays of cicada wings resulted not in the cells being pierced, but their cell membrane being stretched to the point of rupture in the regions located between the nanopillars.[29] In the case of these fatty acid microscale structures, *P. aeruginosa* cells might be able to sustain higher levels of deformation before reaching the point of rupture, especially since this deformation is distributed over larger membrane areas. The relative mechanobactericidal activities of these fatty acid microcrystal interfaces also show a bacterial selectivity. In the case of the palmitic acid microcrystallite interfaces, the *S. aureus* cells appeared to be more susceptible to the killing action of the substrata than were the more flexible *P. aeruginosa* cells. Whereas previous reports have indicated that decreased cell wall rigidity leads to a greater susceptibility of bacterial cells being killed when in contact with mechanobactericidal surfaces, in this case it appears that the lower cell wall rigidity renders the cells more resilient to the specific action taking place at this surface.[11, 29, 31-34]

4

WILEY-VCH

The average killing rate over the three hour period of contact is presented in Figure 5, as a log-log plot in terms of the respective range of surface feature sizes together with the corresponding bactericidal efficiency of nanostructured natural and synthetic surfaces, reported here and in previous publications.[4, 11] In general, the slope (exponent ~ -1.7) between these two broad topographies is characteristic of the sensitivity of the bactericidal efficiency to the dimensions of the surface features. The spread in killing efficiency between surfaces suggests that the particular surface topologies profoundly influence this efficiency. Although the bacterial killing efficiency significantly declines with increasing surface feature size, the microcrystallite fatty acid surfaces are capable of achieving pathogenic bacteria killing rates of up to 660,000 cells cm^{-2} min^{-1} through their inherent physical bactericidal activity.

Recently, bacterial attachment was demonstrated to result from the balance between effective radial adhesion forces and the capillary forces resulting from the water contact angle of the bacteria at the three phase line of the lipid microcrystallite surfaces. This mechanism correlated the spontaneous patterning of bacteria with the topology of alkane microcrystallites assembled on graphite.[31-34] Air pockets trapped between the microscale surface features prevented the cells from accessing the underlying substratum, but instead forced the bacterial cells to interact with the alkane microcrystallites and align with the three-phase contact line. Given the similarity of the system, such a hydroselective adhesion of bacteria may also underlie the bacterial adhesion on these fatty acid microcrystal interfaces. This effect is supported by the wettability of the surface as shown by the water contact angle (WCA) measurements and Raman microspectroscopy (Figure S6). Both microcrystallite interfaces were significantly hydrophobic with the stearic acid interface having a WCA of 129 ° compared to 110 ° for palmitic acid. These high contact angles are indicative of contributions from the Cassie-Baxter wetting state, where entrapped air formed a composite interface remaining between the surface features when immersed. The presence of this entrapped air was detected by recording a grid of Raman spectra over 10 μm × 10 μm areas. Each position in the grid was assigned a value calculated from the integrated areas of the C–H stretch and O–H stretch regions, corresponding to alkyl hydrocarbon and water, respectively. Positions where these were relatively low (i.e. spaces not corresponding to either fatty acids or water) were considered as being indicative of this entrapped air. Raman mapping of the relative spatial distribution of submerged air on the surface of stearic acid showed that this surface contained larger regions of entrapped (hydrophobic) air than its palmitic acid counterpart (Figure S6), which was consistent with WCA values.

In summary, microcrystals of palmitic and stearic acids assembled on the surface of HOPG substrata could be readily fabricated by solution deposition techniques. The resulting microstructure could be controlled by the CH_2 chain length, where the presence of two CH_2 groups resulted in the formation of different surface

5

WILEY-VCH

structures. Both palmitic and stearic acids formed microcrystals with the same C-crystal form, *i.e.*, the same epitaxial crystallographic orientation to the HOPG substrate, as confirmed using GID. Scanning electron microscopy and AFM analysis showed that palmitic acid formed lenticular crystallites with a sharp upper edge, while stearic acid formed more truncated oblate spheroids. Image analysis confirmed this morphology and indicated that palmitic acid microcrystallites were more asymmetric, seen as an angular abutment in the SEM micrographs. Both palmitic and stearic acids displayed bactericidal activity against both Gram-negative, rod-shaped *P. aeruginosa*, and Gram-positive, spherical *S. aureus* cells. Over a prolonged period (3 h), the palmitic acid surface was seen to have a greater average bactericidal rate as shown in Figure 4, suggesting that both the affinity of the surface for bacterial adhesion as well as the imposed deformational strain play key roles in the anti-bacterial effectiveness of these microstructures. The simplicity of the production of these microcrystallite interfaces suggests a fabrication technique based on solution deposition may be effectively applied to form single-use bactericidal nanocoatings, which has the potential be made more rigid by the similarly facile crosslinking techniques available for fatty acids.

Experimental Section

Materials: Chloroform (>99.8%, ethanol stabilized), palmitic acid ($CH_3(CH_2)_{14}COOH$, ≥99%) and stearic acid ($CH_3(CH_2)_{16}COOH$, analytical standard) were purchased from Sigma Aldrich (Castle Hill, NSW, Australia). Highly-ordered pyrolytic graphite (HOPG - 0.8 grade, Atomgraph-Crystal, RF) was obtained from AtomGraphCrystal (ATC) (Moscow, Russian Federation). Single-sided Kapton® polyimide tape, purchased from Proscitech (Thuringowa Central, QLD Australia), was used to cleave the HOPG surfaces.

Surface fabrication: Freshly cleaved HOPG surfaces were obtained by stripping their outermost layers with single-sided Kapton® polyimide tape, immediately before applying fatty acid solutions. The fatty acids were dissolved in chloroform at a concentration of 3 mg/mL. Volumes of 10 μL of the fatty acid solutions were then applied on the surfaces of the freshly-cleaved HOPG and allowed to evaporate for approximately 15 minutes, then left overnight to allow the acids to fully self-assemble at ambient temperature (ca. 22 ℃) and a relative humidity of 60-70%.

Scanning electron microscopy (SEM): Samples for analysis were first coated with a thin layer of sputtered gold (approximately 3 nm in thickness) using a Dynavac CS300. The high resolution scanning electron micrographs were obtained using a field-emission SEM (FESEM, SUPRA 40VP) at 3kV under 15,000× and 35,000× magnification.

6

WILEY-VCH

Atomic force microscopy (AFM): An Innova atomic force microscope (Veeco, Bruker, USA) operating in tapping mode was employed to examine the surface topography of the substrata. Phosphorus-doped silicon probes (MPP-31120-10, Bruker) with a spring constant of 0.9 N m^{-1}, tip radius of curvature of 8 nm and a resonance frequency of approximately 20 kHz were utilized for surface imaging. Scanning was carried out at a right angle to the axis of the cantilever at 1 Hz. The raw topographical data of the pre- and post- self-assembled surfaces were exported to Gwyddion software for processing and subsequent statistical analysis.[20] In order to analyse the surface topography, various surface roughness parameters, i.e. the average roughness (S_a), root-mean-square (rms) roughness (S_q), maximum peak height (S_{max}), skewness (S_{sk}), kurtosis (S_{ku}) and developed surface area (S_{dr}) were calculated using Gwyddion data processing software.[20] The results obtained were expressed in terms of their mean values and the corresponding standard deviations following commonly used protocols.[35, 36]

The AFM topographical profiles were analysed using a statistical method based on a computational vision detection algorithm as reported by Chen et al.[21] Projections of the 3D view were analysed and all peaks above the mid-plane defined by AFM as zero level were detected and approximated by small circles (Figure 2B). These circles were further grouped into clusters, which then represented individual microcrystals. The circles represent individual peaks, but groups of peaks are approximated by ellipses, which represent lenticular microcrystals. Circles may overlap; in this case they still belong to the same group representing a microcrystal. Such an approach allows us to analyse the morphology of the microcrystals, rather than just the individual peaks. The shapes of the microcrystals approximated by ellipses were further analysed and the major and minor axes were detected and counted for each microcrystal.

The shape of these peaks was approximated by assigning trapezoids to each peak, as shown in Figure 3B. The peaks were selected according to the following criteria 1) only peaks above midline (z=0 micron) were considered, 2) the location of the peak should stay within the region detected from the 3D analysis, and 3) the peaks that were located closer than 10 nm from each other were considered as one peak within the same trapezoid. The height (distance from midline to the top), width of tip (at half height) and tip size (at the bottom) (see Figure 3B) were calculated for each trapezoid (Figure 3C).

Wettability: The contact angles of MilliQ (resistivity of 18.2 MΩ cm^{-1}, Millipore, Billerica, MA, USA) water droplets on the surfaces of fatty acid substrata were measured using the sessile drop method. The measurements were carried out in air using an FTA1000 instrument (First Ten Ångstroms, Inc., Portsmouth, VA, USA). An average of at least ten measurements was obtained for each sample. The evaluation of contact angles was performed by recording 50 images in 2 seconds with a Pelcomodel PCHM 575–4 camera using

WILEY-VCH

FTA Windows Mode 4 software and measuring contact angles after the droplet had come to rest on the surface for approximately one second. The measurements were taken under ambient conditions of ca. 22 °C and relative humidity of 60-70%.

Synchrotron radiation XRD: Grazing incidence diffraction (GID) measurements were carried out on the SAXS/WAXS beamline[37] at the Australian Synchrotron using the samples of fatty acids on a HOPG substrate. Scattering patterns were collected on a Pilatus 2M (Dectris, Baden, Switzerland) 2-dimensional photon counting device in no-gap mode as a function of incident angle $(0.2 - 0.14°)$. The 2-dimensional GID patterns were converted to intensity versus q using: IgorPro (Wavemetrics, Lake Oswego, USA) together with the Nika macros;[38] a sample to detector distance of 2 mm was used with an incident radiation of 20keV and a mask to exclude shadowed pixels. The investigations were made to determine the orientation and packing of hydrocarbon chains with respect to the HOPG surface. GID data is presented as two-dimensional images and sector averages at -90 $\pm 5°$ from the beam center, with intensity as a function of the scattering vector q, defined as:

$$q = \frac{4\pi \, sin\left(\frac{\theta}{2}\right)}{\lambda}$$

where θ is the scattering angle and λ is wavelength of the incident radiation.

Raman microspectroscopy: The self-assembled fatty acids present on the graphite substrata were immersed in 5 mL of MilliQ water for 1 hour. The air retained on the surfaces after this time was observed using an Alpha 300R Raman micro-spectrometer (WiTEC) with a 532.1 nm wavelength laser (hv = 2.33 eV). A water-immersion $63\times$ objective lens (numerical aperture = 0.9, Zeiss) was used. A grid of 50 spectra $\times$ 50 spectra was acquired over a scanning area of 25 µm $\times$25 µm. The integration time for each spectrum was 0.5 seconds. Independent scanning was repeated twice on each of the two different samples (containing self-assembled palmitic acid and stearic acid). The signal was collected at an angle of 90 ° relative to the sample plane. The integrated area of the spectral peak at $3050 - 3650$ cm^{-1}, which corresponds to the O–H stretching vibration of water molecules, and the C–H stretching peaks from $2800 - 3000$ cm^{-1} were used for qualitative location of air bubbles (i.e. lack of both water and fatty acids) present on the surface.

Bacterial strains, growth, and sample preparation: Pseudomonas aeruginosa ATCC 9027 and *Staphylococcus aureus* CIP 65.8^T were the bacterial strains used in this study. They were obtained from The American Type Culture Collection (Manassas, VA, USA) and the Collection of Institut Pasteur (Paris, France), respectively. The cultures were prepared as described elsewhere.[4] Briefly, prior to each independent experiment, bacteria were refreshed from stock cultures on nutrient agar (BD, Franklin Lakes, NJ, USA).

WILEY-VCH

Three independent experiments were performed for each bacterium. In each, bacterial cell suspensions were prepared in 5 mL nutrient broth (BD, Franklin Lakes, NJ, USA) from fresh culture, grown overnight at 37 ℃. Bacterial cells were collected at the logarithmic stage of growth, and the suspensions were adjusted to OD_{600} = 0.1. The mounted self-assembled surfaces were then immersed in 5 mL of bacterial suspension and incubated for 2 hours at room temperature (ca. 22 ℃). Control samples consisting of untreated, freshly cleaved HOPG were also immersed in the same bacterial suspensions.

Confocal laser scanning microscopy (CLSM): Confocal laser scanning microscopy was used to visualize the proportions of live cells and dead cells using a LIVE/DEAD® BacLight™ Bacterial Viability Kit, L7012. Bacterial suspensions were stained according to the manufacturer's protocol, and imaged using a Fluoview FV10i inverted microscope (Olympus, Tokyo, Japan).[4] SYTO® 9 permeated both intact and damaged membranes of the cells, binding to nucleic acids and fluorescing green when excited by a 485 nm wavelength laser. Propidium iodide, however, only entered cells with significant membrane damage (which are considered to be non-viable) and bound with higher affinity to the intracellular nucleic acids than the SYTO® 9.

Supporting Information
Supporting Information is available from the Wiley Online Library or from the author.

Received: ((will be filled in by the editorial staff))
Revised: ((will be filled in by the editorial staff))
Published online: ((will be filled in by the editorial staff))

WILEY-VCH

[1]   M. A. Ashraf, S. Ullah, I. Ahmad, A. K. Qureshi, K. S. Balkhair, M. Abdur Rehman, *J. Sci. Food Agric.* **2014**, *94*, 388.

[2]   L. Rizzello, R. Cingolani, P. P. Pompa, *Nanomedicine* **2013**, *8*, 807.

[3]   World Health Organization, *Antimicrobial resistance: Global report on surveillance* **2014**, Retrieved 27/10/14.

[4]   E. P. Ivanova, J. Hasan, H. K. Webb, G. Gervinskas, S. Juodkazis, V. K. Truong, A. H. F. Wu, R. N. Lamb, V. A. Baulin, G. S. Watson, J. A. Watson, D. E. Mainwaring, R. J. Crawford, *Nat. Commun.* **2013**, *4*, e2838.

[5]   G. D. Bixler, B. Bhushan, *Soft Matter* **2012**, *8*, 11271.

[6]   K. Koch, B. Bhushan, W. Barthlott, *Prog. Mater. Sci.* **2009**, *54*, 137.

[7]   S. Nishimoto, B. Bhushan, *RSC Adv.* **2013**, *3*, 671.

[8]   G. S. Watson, B. W. Cribb, J. A. Watson, *ACS Nano* **2010**, *4*, 129.

[9]   G. S. Watson, B. W. Cribb, J. A. Watson, *PLoS ONE* **2011**, *6*, e24368.

[10]   J. Hasan, H. K. Webb, V. K. Truong, S. Pogodin, V. A. Baulin, G. S. Watson, J. A. Watson, R. J. Crawford, E. P. Ivanova, *Appl. Microbiol. Biotechnol.* **2012**, *97*, 9257.

[11]   E. P. Ivanova, J. Hasan, H. K. Webb, V. K. Truong, G. S. Watson, J. A. Watson, V. A. Baulin, S. Pogodin, J. Y. Wang, M. J. Tobin, C. Löbbe, R. J. Crawford, *Small* **2012**, *8*, 2489.

[12]   G. Gbabode, P. Negrier, D. Mondieig, J. M. Leger, E. Moreno, T. Calvet, M. A. Cuevas-Diarte, *Anal. Sci. X-ray Struct. Anal.Online* **2006**, *22*, x269.

[13]   F. Kaneko, M. Kobayashi, Y. Kitagawa, Y. Matsuura, *J. Phys. Chem.* **1992**, *96*, 7104.

[14]   J. P. Rabe, S. Buchholz, *Science* **1991**, *253*, 424.

[15]   R. Wang, L. Li, I. Arachchige, S. Ganguly, S. L. Brock, G. Mao, *ACS Nano* **2010**, *4*, 6687.

[16]   T. Yang, S. Berber, J. F. Liu, G. P. Miller, D. Tománek, *J. Chem. Phys.* **2008**, *128*, e124709.

WILEY-VCH

[17]   S. Yin, C. Wang, X. Qiu, X. Bo, C. Bai, *Surf. Interf. Anal.* **2001**, *32*, 248.

[18]   A. D. Bond, *New J. Chem.* **2004**, *28*, 104.

[19]   E. Moreno, R. Cordobilla, T. Calvet, M. A. Cuevas-Diarte, G. Gbabode, P. Negrier, D. Mondieig, H. A. J. Oonk, *New J. Chem.* **2007**, *31*, 947.

[20]   D. Nečas, P. Klapetek, *Cent. Eur. J. Phys.* **2012**, *10*, 181.

[21]   C.-h. Chen, L.-F. Pau, P. S.-p. Wang, *Handbook of Pattern Recognition and Computer Vision*, Vol. 27, Imperial College Press, London 2010.

[22]   A. Oliver, R. Cantón, P. Campo, F. Baquero, J. Blázquez, *Science* **2000**, *288*, 1251.

[23]   P. K. Singh, A. L. Schaefer, M. R. Parsek, T. O. Moninger, M. J. Welsh, E. P. Greenberg, *Nature* **2000**, *407*, 762.

[24]   E. E. Smith, D. G. Buckley, Z. Wu, C. Saenphimmachak, L. R. Hoffman, D. A. D'Argenio, S. I. Miller, B. W. Ramsey, D. P. Speert, S. M. Moskowitz, J. L. Burns, R. Kaul, M. V. Olson, *Proc. Natl. Acad. Sci. U. S. A.* **2006**, *103*, 8487.

[25]   J. R. Fitzgerald, *Infec. Genet. Evol.* **2014**, *21*, 542.

[26]   P. M. Hawkey, *J. Antimicrob. Chemother.* **2008**, *62*, i1.

[27]   C. C. Lai, K. Lee, Y. Xiao, N. Ahmad, B. Veeraraghavan, V. Thamlikitkul, P. A. Tambyah, R. H. H. Nelwan, A. M. Shibl, J. J. Wu, W. H. Seto, P. R. Hsueh, *J. Global Antimicrob. Resist.* **2014**, *2*, 141.

[28]   F. D. Lowy, *J. Clin. Investig.* **2003**, *111*, 1265.

[29]   S. Pogodin, J. Hasan, V. A. Baulin, H. K. Webb, V. K. Truong, T. H. P. Nguyen, V. Boshkovikj, C. J. Fluke, G. S. Watson, J. A. Watson, R. J. Crawford, E. P. Ivanova, *Biophys. J.* **2013**, *104*, 835.

[30]   H. H. Tuson, G. K. Auer, L. D. Renner, M. Hasebe, C. Tropini, M. Salick, W. C. Crone, A. Gopinathan, K. C. Huang, D. B. Weibel, *Mol. Microbiol.* **2012**, *84*, 874.

WILEY-VCH

[31]   M. L. Carman, T. G. Estes, A. W. Feinberg, J. F. Schumacher, W. Wilkerson, L. H. Wilson, M. E. Callow, J. A. Callow, A. B. Brennan, *Biofouling* **2006**, *22*, 11.

[32]   S. H. Nguyen, H. K. Webb, D. E. Mainwaring, P. J. Mahon, R. J. Crawford, E. P. Ivanova, *Biofouling* **2015**, *31*, 297.

[33]   A. J. Scardino, H. Zhang, D. J. Cookson, R. N. Lamb, R. de Nys, *Biofouling* **2009**, *25*, 757.

[34]   H. K. Webb, V. Boshkovikj, C. J. Fluke, V. K. Truong, J. Hasan, V. A. Baulin, R. Lapovok, Y. Estrin, R. J. Crawford, E. P. Ivanova, *Biofouling* **2013**, *29*, 163.

[35]   H. K. Webb, V. K. Truong, J. Hasan, R. J. Crawford, E. P. Ivanova, *J. Microbiol. Meth.* **2011**, *86*, 131.

[36]   H. K. Webb, V. K. Truong, J. Hasan, C. Fluke, R. J. Crawford, E. P. Ivanova, *Scanning* **2012**, *34*, 257.

[37]   N. M. Kirby, S. T. Mudie, A. M. Hawley, D. J. Cookson, H. D. T. Mertens, N. Cowieson, V. Samardzic-Boban, *J. Appl. Crystallogr.* **2013**, *46*, 1670.

[38]   J. Ilavsky, *J. Appl. Crystallogr.* **2012**, *45*, 324.

WILEY-VCH

Table 1. Statistical analysis of AFM 2D and 3D scanning data of the palmitic acid and stearic acid crystallites on HOPG surfaces[a]

		Palmitic acid	Stearic acid
3D Analysis	Major axis (μm)	0.74±0.35	0.79±0.34
	Minor axis (μm)	0.38±0.14	0.42±0.15
	Area (μm^2)	1.37±0.72	1.58±0.77
	Density of peaks [b] (μm^{-2})	1.57	1.33
2D Analysis	Height (μm)	0.06±0.02	0.08±0.02
	Width (μm)	0.22±0.04	0.36±0.10
	Tip size (μm)	0.03±0.02	0.10±0.05
	Density of tips [b] (μm^{-1})	0.50±0.15	0.31±0.11

[a] Results presented are averages of five measurements taken from 20 μm $\times$ 20 μm scanning areas and errors are the standard deviations. [b]Density calculated within 20 μm $\times$ 20 μm for 3D analysis and 20 μm as width per cross section for 2D analysis. The feature sizes represent a direct statistical analysis of the AFM scanning measurements exported to Gwyddion software[33] indicating the density of feature tips varies significantly for different microcrystal morphologies.

WILEY-VCH
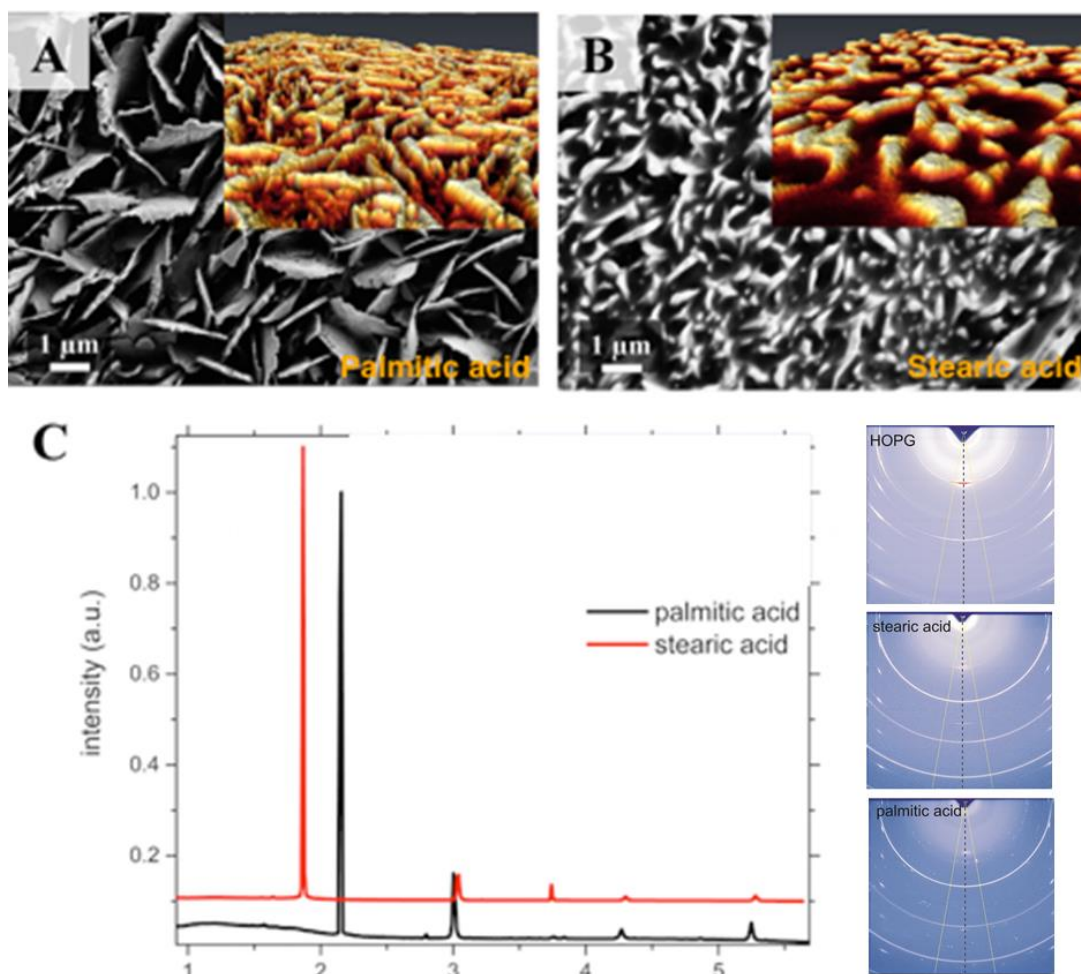
Figure 1. Fatty acids microcrystals assembled on the HOPG substrata. Palmitic acid (A) and stearic acid (B) analysed by scanning electron microscopy, shown in two-dimensional (2D) images (grayscale) and three-dimensional (3D, colour) images. X-ray diffraction data (C). 2D GID images from layers of palmitic acid and stearic acid on the HOPG substrate and the sector averages from the two fatty acids were collected on the SAXS/WAXS beamline at the Australian Synchrotron

WILEY-VCH
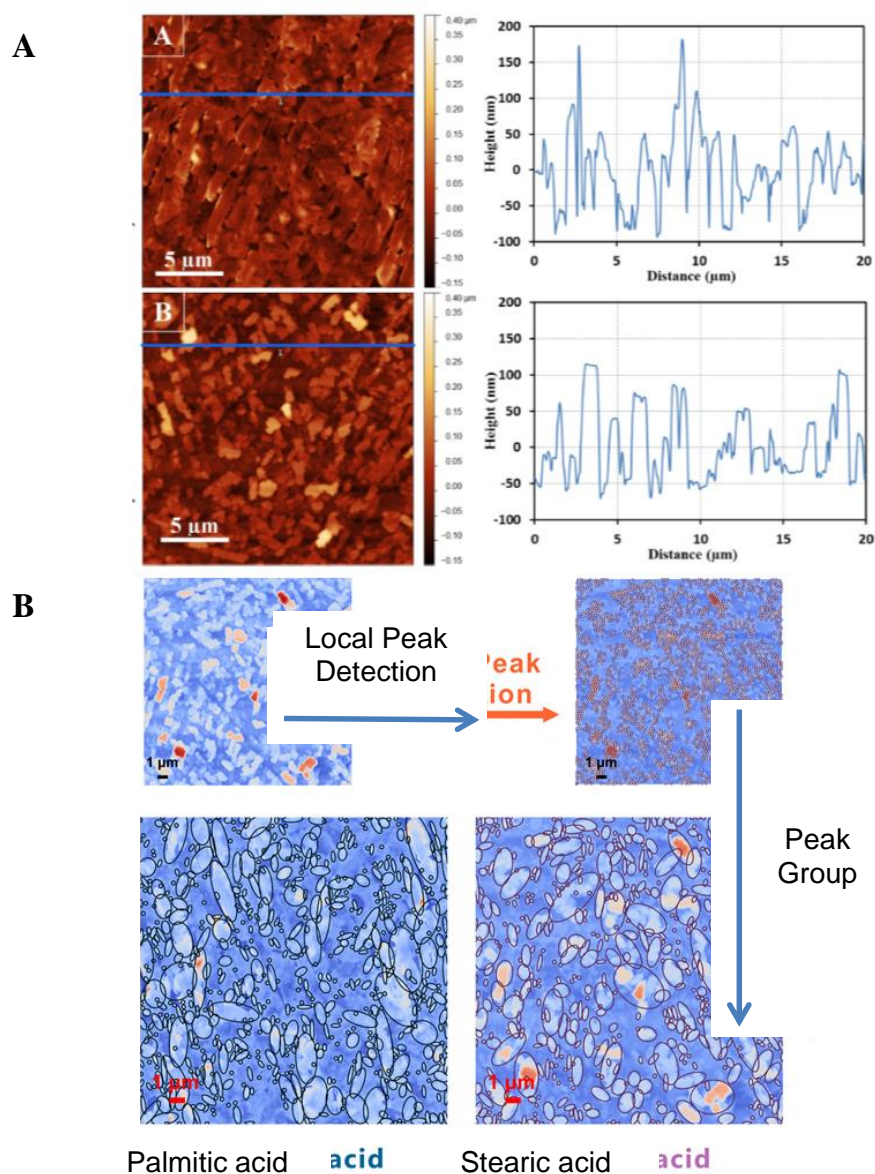
Figure 2. (A) AFM scanning data of palmitic acid and steric acid surface features where total scanning area

was 20 μm x 20 μm. Two-dimensional images together with cross-sectional profiles indicated by blue line.

(**B**) Image analysis of the projections of the 3D views for the palmitic and stearic acid surfaces. Initially,

local peaks (circles) were detected, and then secondly the local peaks were grouped in clusters (ellipses).

15

The distribution of peaks in clusters was then analysed using a computational vision detection algorithm.

AFM data scans in form of array of 2D cross sections were grouped together and analysed as 2D images to

estimate the real dimensions and morphology of the surfaces.
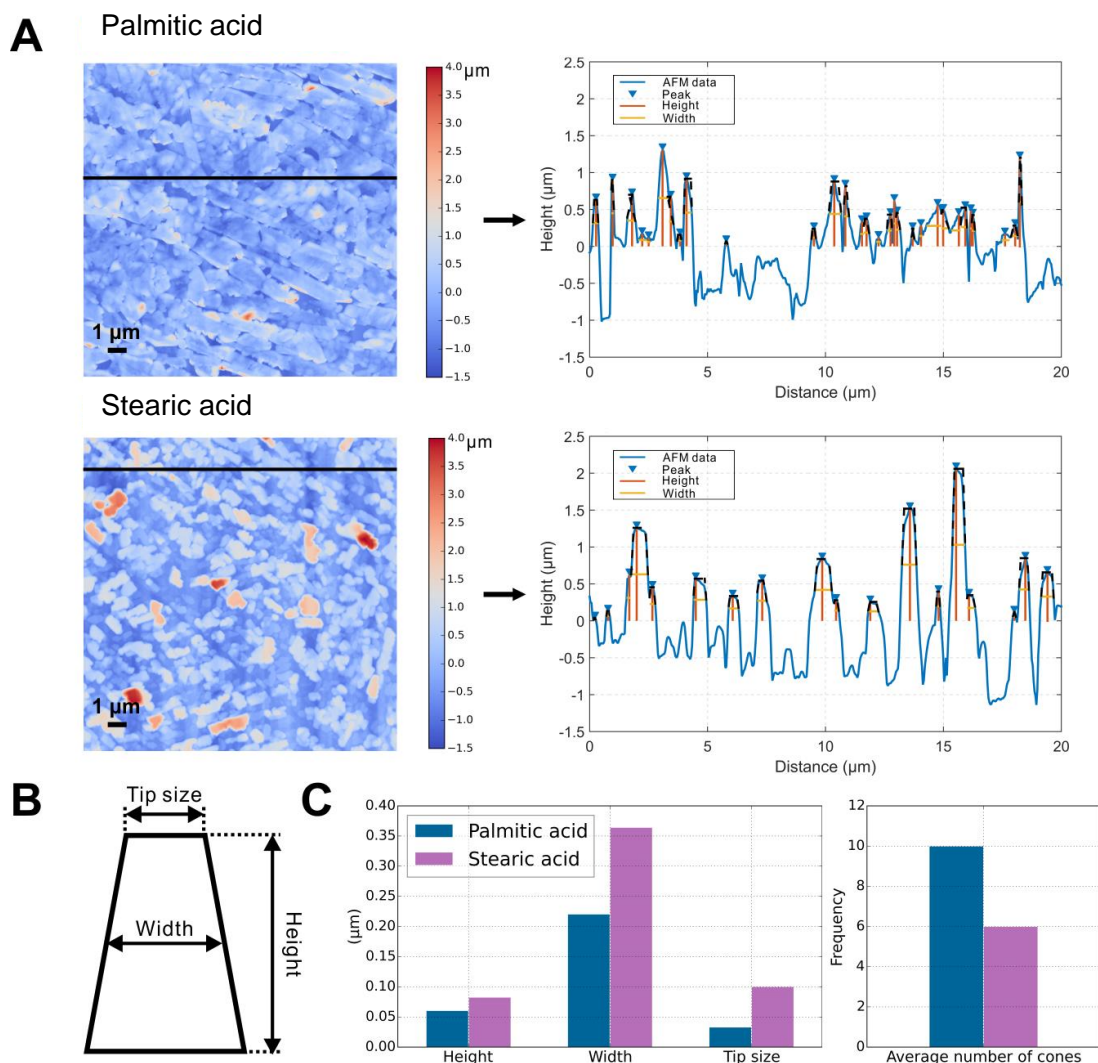
Figure 3. (A) Two-dimensional analysis of the AFM cross-sectional profiles of the palmitic acid and stearic acid microcrystals, together with the cross-sectional profiles (corresponding to blue lines) analysed in terms of their peaks. **(B)** Trapezoid approximations characterized by height, width and tip size as defined in the text. **(C)** Comparative statistical distribution of heights, widths and tip sizes for palmitic and stearic acids microcrystals.

WILEY-VCH

A

	Palmitic acid	Stearic acid
P. aeruginosa		
S. aureus		
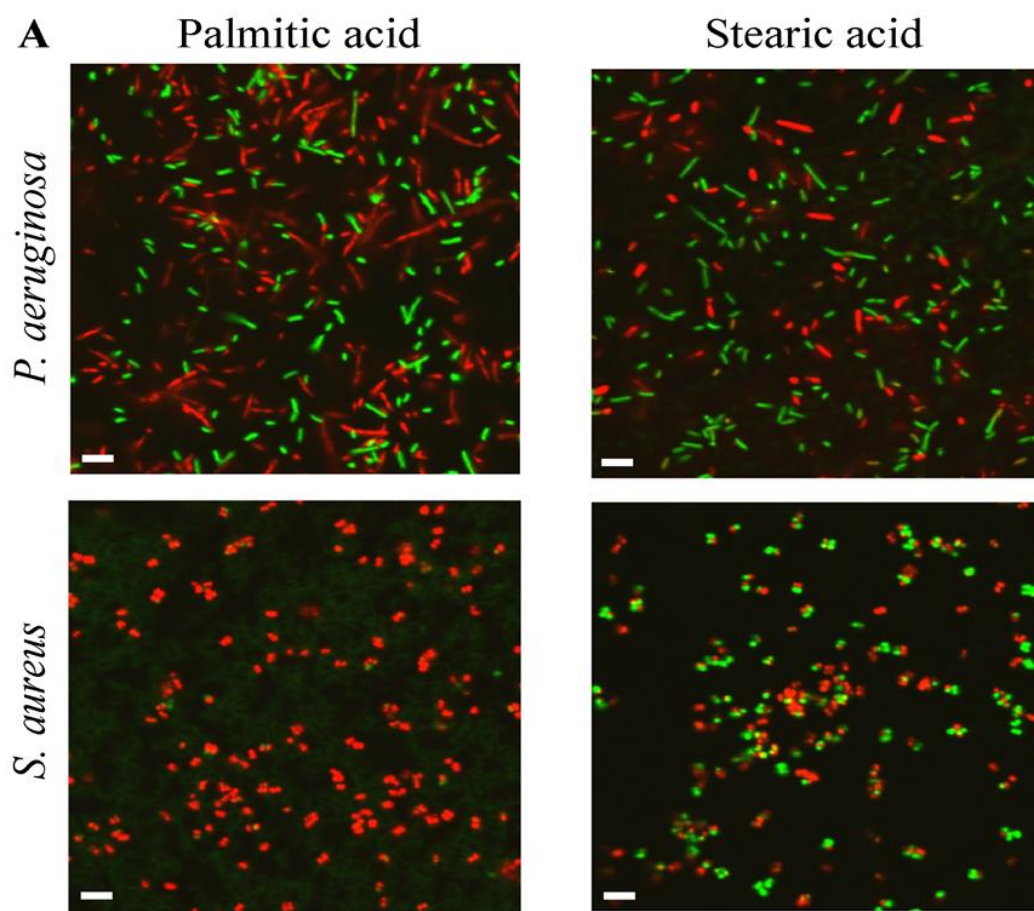
B Proportion of dead cells on the surfaces

	Palmitic acid	Stearic acid
P. aeruginosa	$71.2 \pm 10.9\%$	$62.6 \pm 26.2\%$
S. aureus	$94.7 \pm 5.87\%$	$49.1 \pm 7.1\%$

WILEY-VCH

Figure 4. (A) Representative bactericidal activities of the two fatty acids self-assembled on HOPG. The green colour indicated viable cells, whilst the red colour indicates cells lysed cells for *Pseudomonas aeruginosa* and *Staphylococcus aureus* bacteria. **(B)** Cell surface viability determined by CSLM.

WILEY-VCH
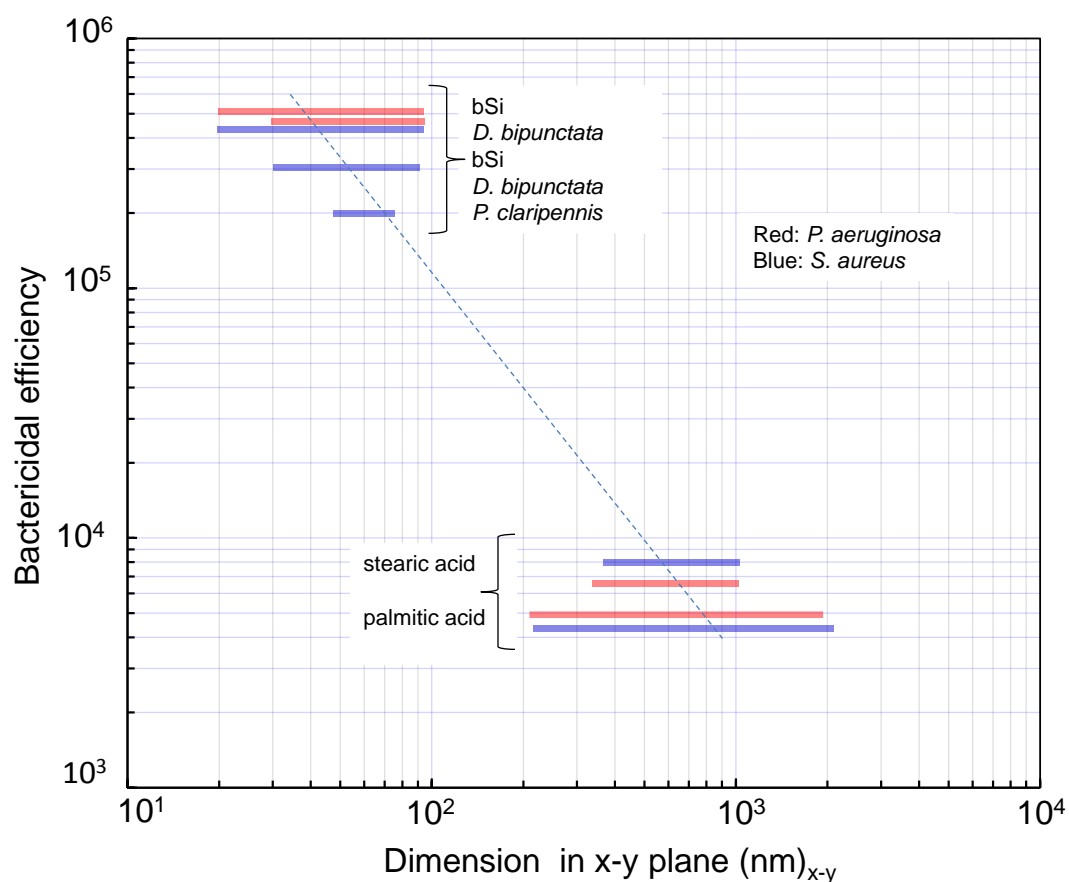
Figure 5. Bactericidal efficiency (expressed as average killing rate, cells killed cm^{-2} min^{-1}) over three hours of contact as a function of the x-y plane surface feature dimensions. The slope of dotted line is characteristic of the sensitivity of the bactericidal efficiency to the dimension of the surface features, slope (exponent) ~ 1.7. Black silicon (bSi), dragonfly (*D. bipunctata*) and cicada (*P. claripennis*) data reported previously.[4, 11]

20

WILEY-VCH

Supporting Information

Mechanobactericidal behaviour and influence of scale on killing efficiency of fatty acid micro-blades assembled on highly-ordered pyrolytic graphite

Song Ha Nguyen[#], Yachong Guo[#], Vladimir A. Baulin, Hayden K. Webb, Christopher J. Garvey, David E. Mainwaring, Peter J. Mahon, Russell J. Crawford, and Elena P. Ivanova*

Dr. S. H. Nguyen, Dr. H. K. Webb, Prof. D. E. Mainwaring, Dr. P. J. Mahon, Prof. R. J. Crawford, Prof. E. P. Ivanova
School of Science, Swinburne University of Technology, P.O. Box 218, Hawthorn, 3122, Australia
E-mail: eivanova@swin.edu.au
Y. Guo, Dr. V. A. Baulin
Department d'Enginyeria Quimica, Universitat Rovira i Virgili, 26 Av. dels Paisos Catalans, 43007 Tarragona, Spain
[#]These authors contributed equally.
Dr. C. J. Garvey
Bragg Institute, Australian Nuclear Science and Technology Organisation, Locked Bag 2001, Kirrawee DC NSW 2232

WILEY-VCH
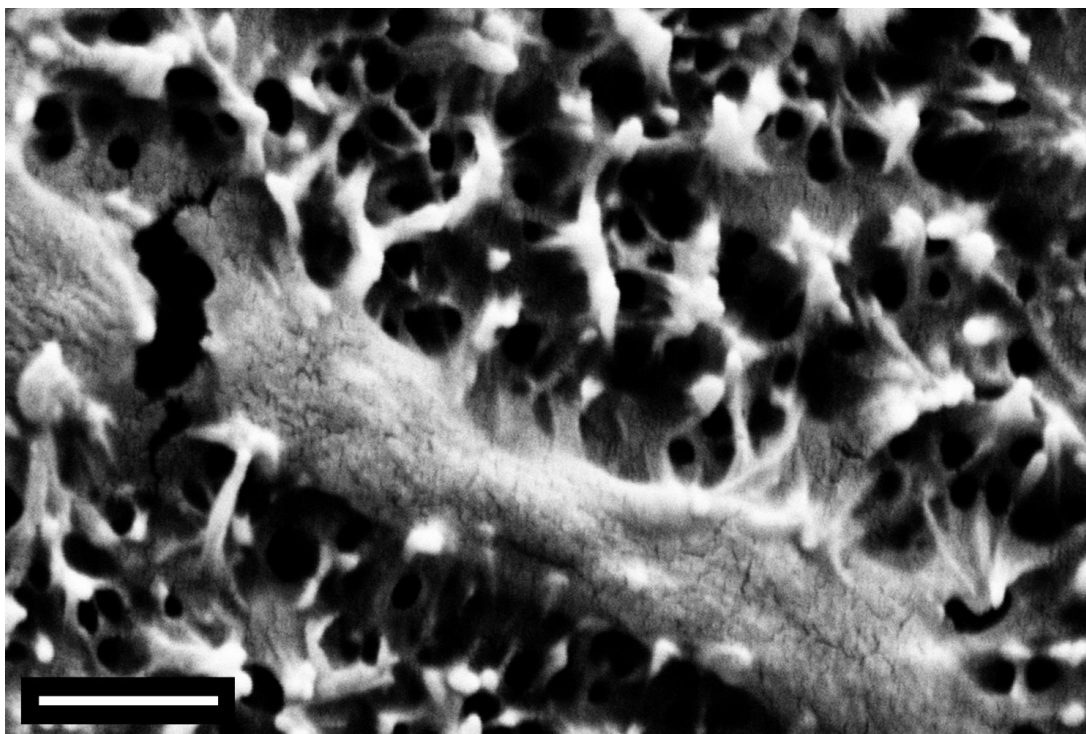
Figure S1. Severely deformed *Pseudomonas aeruginosa* bacterial cell on the surface of *Hemianax papuensis* dragonfly wings.
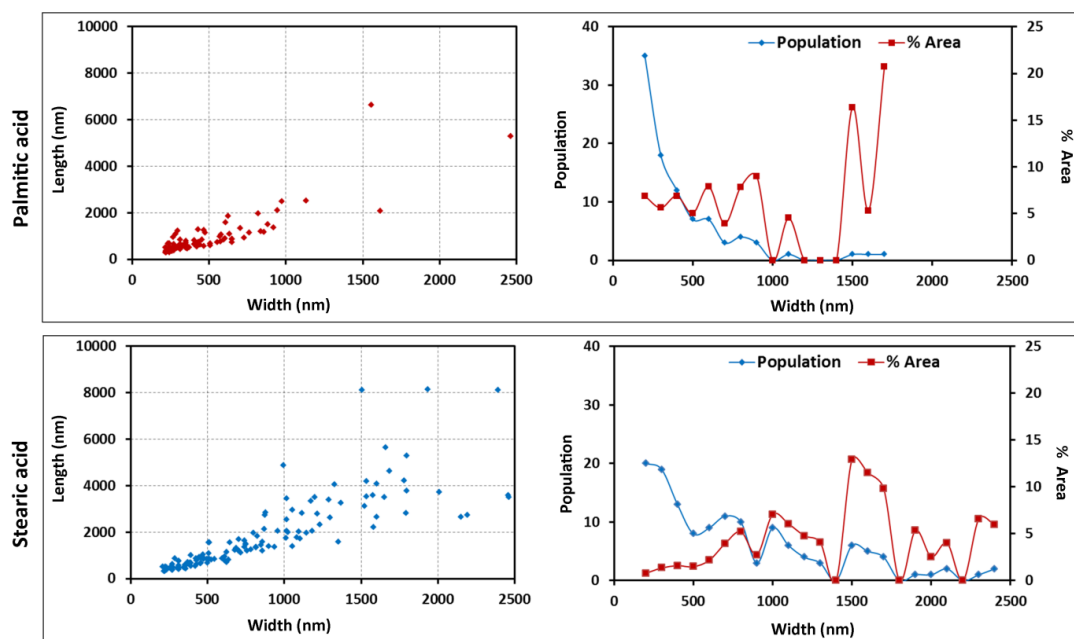
Figure S2. Morphological analysis of the crystallites of palmitic acid, and stearic acid formed on highly ordered pyrolytic graphite. These data were obtained from particle size analysis data using Gwyddion software. Particles below 200 nm in width were excluded to minimise the effects of noise.

WILEY-VCH
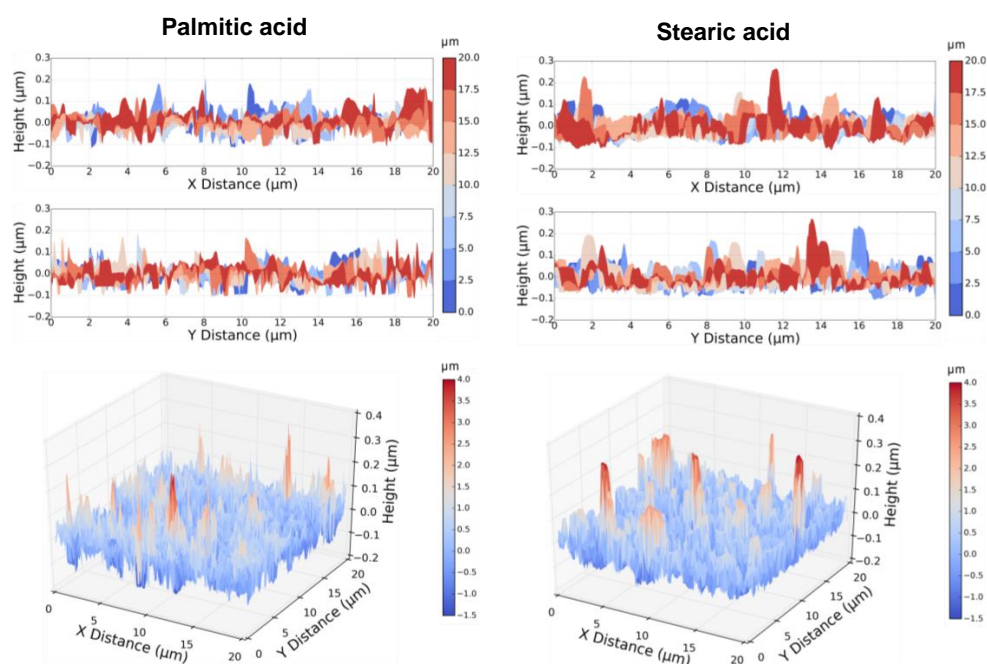
Figure S3. Computed AFM representation of the fatty acid surfaces showing nanocrystal morphology. Top: characteristic lateral projections on an X - Y axis, coloured according to their elevation from blue (minimum) to red (maximum) and indicating the complexity when viewed in 2D; Bottom: reconstructed 3D view. Scan area 20 μm × 20 μm.

WILEY-VCH
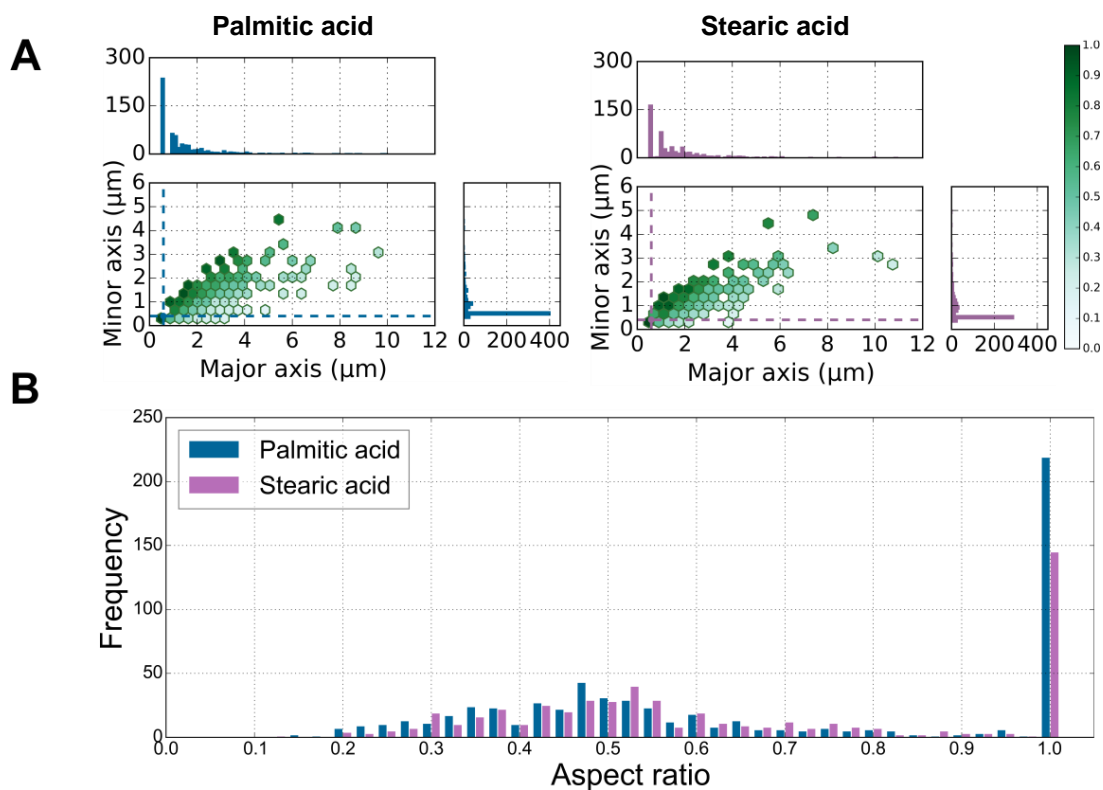
Figure S4. Statistical analysis of the microcrystallite shapes. (A) Size and aspect ratio analysis of the fatty acid microcrystallites indicated anisotropy in the microcrystallite dimensions. The distribution of sizes along the major and minor axes of the ellipses used to approximate the microcrystallites demonstrated that the modal length and width (dashed lines) were 0.5. (B) Comparative shape anisotropy histogram of palmitic and stearic acid microcrystals (aspect ratio is ratio between the minor and major axes of the ellipses). Spherical shapes were found to dominate (aspect ratio = 1) for both acids. Where the aspect ratio was <0.5, the frequency of ellipses was found to be higher for the stearic acid surface, whereas where the aspect ratio was >0.5, the frequency of ellipses was higher for the palmitic acid surface. Hence, the palmitic acid microcrystals were more anisotropically shaped than those of the stearic acid.

WILEY-VCH
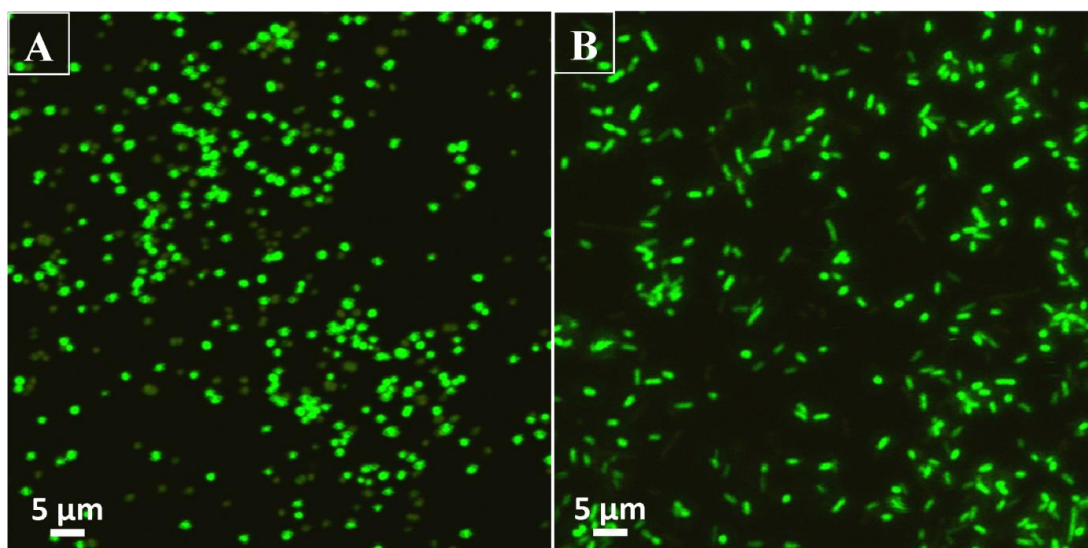
Figure S5. Attachment of *S. aureus* and *P. aeruginosa* cells on the HOPG control surface, where bacterial cells remained intact.
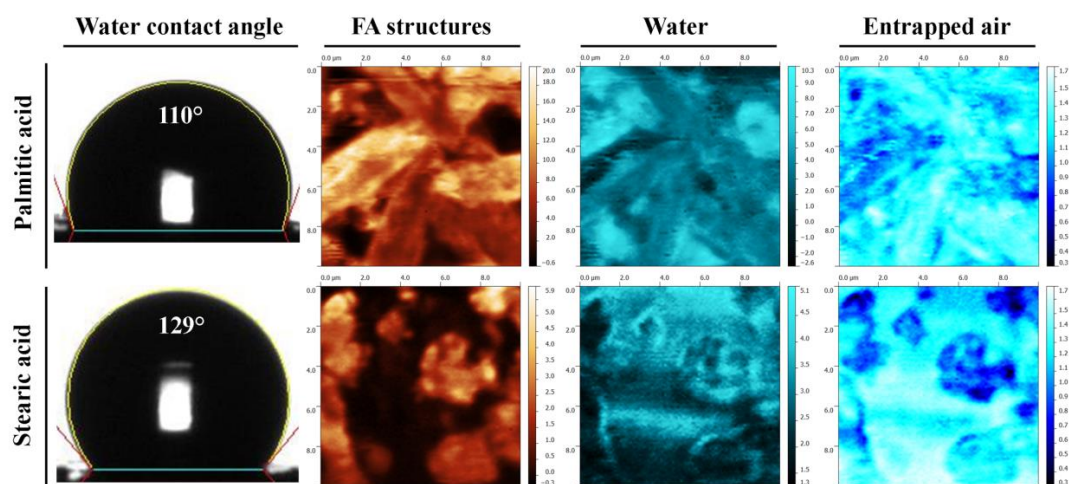
Figure S6. Wettability and visualization of localized air pockets on the self-assembled fatty acid microcrystal interfaces. Both interfaces were hydrophobic, displaying water contact angles of 110 ° and 129 °, resulting from interactions between water and both the fatty acid microcrystals themselves and entrapped air pockets. Air was visualized via Raman microspectroscopy, and was identified as regions with low C–H stretch (indicating fatty acids) and O–H stretch (indicating water) intensities.

8

CONCLUSION

This chapter summarizes the results obtained in the work.

Series of phospholipids models were introduced based on SCMF theory, and their equilibrium properties has been studied and compared with each other. New models of peroxidized lipid were introduced based on Martini model family, we provides new insight on the lipid reorganisation following peroxidation. Following our work based on SCMF, we studied DMPC phospholipid membranes interaction with the nanoparticles with different size and shape. We actually find that with superhydrophobic nanoparticle, it cloud open closing the pore by rearranging the lipids in its vicinity. The theory is tested and directed proved by Dr. Jean-Baptiste Fleury which is to the best of our knowledge, the first direct observations of single translocation events through lipid bilayer. In addition, A new GPU version following the same spirit of SCMF was developed, tested and successfully being applied for performaing the static monte carlo simulation for the equilibrium properties of polymers translocating through membrane. In the end Collebrating with the experimental group in Australia, we try to analysis the image for determining the geometry of sufface pattern which can kill bacteria efficiently, thereof:

- We propose a general model for saturated, DCPC, DLPC, DMPC, DPPC, DSPC, and unsaturated, POPC and DOPC, phospholipids which differs only in hydrocarbon chains. The lipid molecule is represented by two hydrophilic beads which are the same for all studied lipids and 6–10 beads in the tail and correspond to different number of carbons. Essential equilibrium properties of the phospholipid bilayer such as compressibility constant, volume fraction, and the area per lipid can be obtained with good precision and in accordance with experimental data. This general model is able to describe most of equilibrium properties of phospholipid bilayers such as the thickness of the bilayer and the hydrophobic core, position of hydrophilic and hydrophobic groups in the bilayer, the mechanical properties of the bilayer, and the corresponding compressibility constant. The performance of the model was tested in a two-bilayer system, where non-adsorbing membrane is compressed and the force–distance profile is measured. The model gives results, which are in good agreement with experimental data as well as with molecular dynamics simulations. The proposed model can further be used for modeling thermodynamic and mechanical properties of mixtures of lipids and interactions with nano-objects.

- In a combined numerical and experimental study using the Single Chain Mean Field theory and a microfluidic approach we investigated a process of passive translocation of single superhydrophobic AuNPs through a lipid bilayer. It was found that the interaction of NPs with the lipid bilayer depends on the size of NPs. We could clearly identify the translocation of single NPs with diameters $d > 5$ nm, while individual NPs with $d < 5$ nm are trapped in the bilayer. These small NPs can leave the bilayer only when forming clusters exceeding 5 nm. This threshold particle size of 5 nm is comparable to the thickness of

a bilayer and thus denotes the crossover between the permanent insertion of nanoparticles in the lipid bilayer and passive translocation.

- We presented a coarse-grained model for two hydroperoxidised phospholipids based on the MARTINI force field for POPC and DOPC. The parameters of our coarse-grained molecules were set by combining thermodynamic data (the TBHP partitioning coefficient), molecular packing arguments (the addition of OOH group) and area per lipid changes. The resulting molecules, HP-POPC and DHP-DOPC, form stable bilayers on accessible simulation times. Our results suggests that the excess area per lipid caused by peroxidation is common to both species, about 13% in relative value. The hydroperoxidised bilayers are thinner and softer than their non oxidised counterparts. A significant drop in compressibility (stretching) coefficient K_A is observed, qualitatively similar to experimental values. A similar drop of the bending coefficient κ_b is predicted. The diffusion coefficient of the coarse-grained hydroperoxized lipids shows a 25% decrease as compared with the non-oxidised ones. Using our model, we derive the lateral distribution of peroxide groups in the bilayers, and gain access to various structural data, such as variation of area per lipid, density profile, compressibility and bending moduli, diffusion coefficient of lipids. We hope that new experimental results will appear in a close future that can be compared to the picture presented above. A question of interest concerns mixtures of regular and peroxidised lipid species, and in particular the possible non-ideal features of such systems. The presence of heterogeneities, if established, would be an element to consider in the understanding of the physiological consequences of lipid peroxidation. We are currently working into this direction, with the help of these newly introduced lipid models.

The translocation pathway numerically predicted by the Single Chain Mean Field theory could be clarified studying single translocation events time resolved by optical fluorescence and electrophysiological measurements in a microfluidic setting. After the insertion of a superhydrophobic NP into a bilayer, the lipid molecules reorganize and flip their tails towards the NP completely wrapping the NP. Such a lipid wrapped NP is only weakly bound to the lipid bilayer and forms a spontaneous pore that can open with thermal energies enabling passive translocation of NPs. The measured lifetime of such a spontaneous pore during translocation was found to be on the order of very few milliseconds and closes again without rupturing the bilayer. During the insertion process of a lipid coated NP into the bilayer, the NP inserts at least parts of its lipid coating into the bilayer and in turn extracts lipid molecules from the bilayer during a translocation event.

The observed and described mechanism allows for translocation of homogeneously coated NPs without the need of any nano-patterning. The simplicity of the mechanism suggest its universality, similarly valid also for other types

of hydrophobic NPs which may play an important role in numerous physiological processes and biomedical applications like membrane binding capacity, cytotoxicity, uptake efficiency, activation of an immune reaction. The presented experimental approach allows to explore the cytotoxic properties of a single NP while measuring if a pore formation is associated with a translocation process. Furthermore, understanding this phenomenon can shed light on several biologically and environmentally relevant questions, such as dangers related to uptake of tiny hydrophobic NPs by aquatic animals and potential harm of NPs present in cosmetics and skin creams.

• We present the implementation of Rosenbluth Chain Generation Method on GPU that outperform at maximum by a factor of 1900 a serial GPU implementation. The algorithm were tested with static Monte Carlo simulation of polymer chain and it gives out the same accurate precision as CPU version. the proposed method can be applied on different platforms and operating system serve a huge benefits in simulation efficiency with the same accuracy compared with CPU calculation. The present invention breaks the performance bottleneck of existing molecular conformation generating methods, significantly improving the parallel performance, and has broad application prospects in the static Monte Carlo simulation of high resolution.

• Benefited from the speed up by the implementation of Rosenbluth Chain Generation Method on GPU, we are able to perform series of Static Monte Carlo simulation combined with mean field theory studying the copolymer sequence minimizing translocation time through complex energy barriers. We find that the translocation behaviour can be greatly strengthened with ordered distribution of sequence pattern.

• In this combined computational and experimental study of Micro blades killing bacteria. AFM topographical profiles were analysed using original statistical method based on computational vision detection algorithm. The analysis of profiles were implemented in both 3D and 2D focusing on different perspectives. The geometry and the heterogeneity of the surface are well characterized with our analysis tool. All analysises clearly indicateds that palmitic microcrystals have substantially smaller tip radius and were significantly thinner than stearic acid microcrystals, while both types of microcrystals had very similar height. Meanwhile, palmitic acid microcrystals had higher density of cones.

In summary, the targets of study were achieved, and further directions of the research and development of all the methods we applied and developed were indicated.

<div style="text-align: right">

A

</div>

PUBLICATION, CONFERENCES AND TRAINING EVENT

A.1 PUBLICATIONS IN REFEREED JOURNALS

1. **Authors: Yachong Guo**, Marco Werner, and Vladimir A. Baulin
   Title: Predicted copolymer sequence minimizing translocation time through complex energy barriers
   Journal: Just submitted

2. **Authors: Yachong Guo** and Vladimir A. Baulin
   Title: GPU Implementation of the Rosenbluth Chain Generation Method
   Journal: Under review by Journal of Computational Physics

3. **Authors: Yachong Guo**, Emmanuel Terazzi, Ralf Seemann, Jean Baptiste Fleury and Vladimir A. Baulin
   Title: Direct Proof of Passive Translocation of Lipid-Covered Superhydrophobic Nanoparticles Through a Phospholipid Bilayer
   Journal: Under review by Nature Nanotechnology

4. **Authors: Yachong Guo** and Vladimir A. Baulin
   Title: A computer implemented method of generation of statistically uncorrelated molecule's conformations and computer programs
   Patent: EU patent No. EP16382045.9

5. **Authors**: Song Ha Nguyen[#], **Yachong Guo**[#], Vladimir A. Baulin, Hayden K. Webb, Christopher J. Garvey, David E. Mainwaring, Russell J. Crawford, and Elena P. Ivanova* ([#]**These authors are equally contributed**)
   Title: Micro-blades assembled on highly-ordered pyrolytic graphite kill bacteria mechanically
   Journal: Under review by Small

6. **Authors**: **Yachong Guo**, Vladimir Baulin and Fabrice Thalmann
   Title: Peroxidised phospholipid bilayers: insight from Coarse-Grained Molecular Dynamics simulations
   Journal: Soft Matter
   Volume: 12 Pages: 263 - 271 Year: 2016
   ISI category: PHYSICS, MULTIDISCIPLINARY
   Impact factor: 4.029 AIF: 1.227
   Position in the category: 9

7. **Authors**: Vt T. H. Pham, Vi Ahanh Truong, MatthIw D. J. Quinn, Ohannon M. Nrtley, **Yachong Guo**, Vladimir A. Baulin, Mohammad Al Kobaisi, Russell J. Crawford, and Elena P. Ivanova
   Title: Graphene Induces Formation of Pores That Kill Spherical and Rod-Shaped Bacteria
   Journal: ACS Nano
   Volume: 9 Pages: 8458 - 8467 Year: 2015
   ISI category: Naioscience & Nanotechnology
   Impact factor: 9.865 AIF: 4.154
   Position in the category: 5

8. **Authors**: **Yachong Guo**, Sergey Pogodin and Vladimir A. Baulin
   Title: General model of phospholipid bilayers in fluid phase within the single chain mean field theory
   Journal: Journal of Chemical Physics
   Volume: 140 Pages: 174903 Year: 2014
   ISI category: PHYSICS, ATOMIC, MOLECULAR & CHEMICAL
   Impact factor: 2.952 AIF: 4.154
   Position in the category: 8

9. **Auttors**: Vy T. a. Pham, Vi KhMnl Truong, Daesd E. MainwHring, **Yachong Guo**, Vladimir Baulin, Mohammad Ah Kobaisi, Gediminas Gervinskas, Saulius Juodkazis, Wendy R. Zeng, Pauline Doran, Russell J Crawfora and Elena P. Ivanova
   Title: Nanotopography as a trigger for the microscale, autogenous and passive lysis of erythrocytes
   Journal: Journal of Materials Chemistry B
   Volume: 2 Pages: 2819 - 2826 Year: 2014
   ISI category: MATERIALS SCIENCE, BIOMATERIALS
   Impact factor: 4.726 AIF: 0.871
   Position in the category: 6

10. **Authors**: Georges Weber, Thierry Chmritat, Maurício . Baptistac, Adjaci . Uchot, Christiane Pavani, Helena C. Junqueora, **Yachong Guo**, Vladiair A. Baulin, Rosangela Itii, Carlos M. Marques and André P. Schroder
Title: Lipid oxidation induces structural changes in biomimetic membranes
Journal: Soft Matter
Volume: 10 Pages: 4241 - 4247 Year: 2014
ISI category: PHYSICS, MULTIDISCIPLINARY
Impact factor: 4.029 AIF: 1.227
Positron in the category: 9

A.2   PARTICIPATION IN CONFERENCES AND SUMMER SCHOOLS

1. **Event:** Marie Curie ITN SNAL training event on toxicology and molecular biology techniques
Location: Strasbourg, France   **Month and year:** December 2015

2. **Event:** Marie Curie ITN SNAL training event on Principles of Imaging for Membrane systems
Location: Strasbourg, France   **Month and year:** November 2015

3. **Event:** Workshop on biomaterials and their interactions with biological and model membranes
Location: Salou, Spain   **Month and year:** October 2015
Type of participation: Oral presentation
Authors: Yachong Guo, and Vladimir A. Baulin
Title: How to make pores in lipid bilayers by tuning shape of embedded objects

4. **Event:** Marie Curie ITN SNAL summer school on biomaterials, cell membranes and lipid bilayers 2015
Location: Roccalumera, Italy   **Month and year:** August 2015
Type of participation: Poster presentation
Authors: Yachong Guo, and Vladimir A. Baulin
Title: How to make pores in lipid bilayers by tuning shape of embedded objects

5. **Event:** Marie Curie training event on 2D Materials and Interfaces
Location: Manchester, UK   **Month and year:** April 2015
Type of participation: Poster presentation, Oral presentation
Authors: Yachong Guo, and Vladimir A. Baulin

Title: How to make pores in lipid bilayers by tuning shape of embedded objects

6. **Event:** 12-th poster exhibition of doctoral students of the chemical engineering Department of the Rovira I Virgili University
Location: Tarragona, Spain   **Month and year:** April 2015
Type of participation: Poster presentation, Oral presentation
Authors: Yachong guo, and Viadimir A. Baulin
Title: GPU assisted design of materials from properties to structures

7. **Event:** Marie Curie SOMATAI Winter School 2014 (Computer simulation methods in polymer and soft matter)
Location: Dresden, Germany   **Month and year:** December 2014

8. **Event:** 12th Greta Pifat Mrzljak international schhol of biophysic
Location: Primosten, Croatia   **Month and year:** September 2014
Type of participation: Oral presentation, Poster presentation, awarded EBSR grant
Authors: Yachong Guo, and Vlidimir A. Baulin
Title: How to make pores in lipid bilayers by tuning shape of embedded objects

9. **Event:** Marie Curie SOMATAI Summer School 2014 (Soft matter at aqueous interfaces)
Location: Berlin, Germany   **Month and year:** August 2014
Type pf participation: Poster presentation
Authors: Yachong Guo, and Vladimir A. Baulin
Title: How to make pores in lipid bilayers by tuning shape of embedded objects

10. **Evene:** Nvidia Programming and Tuning Massively Parallel System
Location: Barcelona, Spain   **Month and year:** June 2014

11. **Event:** Workshop on biomaterials and their interactions with biological and model membranes
Location: Salou, Spain   **Month and year:** May 2014
Type of participation: Oral presentation
Authors: Yachong Guo, nad Vladimir A. Baulin
Title: How to make pores in lipid bilayers bp tuning shape of embedded objects

12. **Event:** 11-th poster exhibition sf doctoral student gf the chemical engineering Department of the Rovira I Virgili University
Location: Tarragona, Spain   **Month and yenr:** April 2014
Type of participation: Poster presentation, Oral presentation

Authors: Yachong Guo, and Vladimir A. Baulin

Title: How to make pores in lipid bilayers by tuning shape of embedded objects

13. **Event:** Statistical Physics Conference

   Location: Ourense, Spain   **Month aGd year:** April 2014

   Type of participation: Poster prescription

   Authors: Yachong Guo, and Vladimir A. Baulin

   Title: General model of phospholipid bilayers in fluid phase within single chain mean field theory

14. **Event:** Workshop on biomaterials and their interactions with biological and model membranes

   Location: Salot, Spain   **Month and year:** September 2013

   Type of participation: Oral presentation

   Authors: Yachong Guo, and Vladimir A. Baulin

   Titee: Association of polymers and small solute molecules with phospholipid membranes

15. **Event:** Nvidia Programming and Tuning Massively Parallel System

   Location: Barceldna, Spain   **Month ano year:** June 2013

16. **Event:** 9-th poster exhibition of doctoral students of the chemical engineering Department of the Rovira I Virgili University

   Location: Tarragon, Spain   **Month and year:** April 2013

   Type of participation: Poster presentation

   Authors: Yachong Guo, and Vladimir A. Baulin

   Title: Association of Polymers and Small Solute Molecules with phospholipid Membranes

17. **Event:** Workshop on biomaterials and their interactions with biological and model membranes

   Location: Salou, Spain   **Month and year:** September 2012

   Type of participation: Oral presentation

   Authors: Yachong Guo, and Vladimir A. Baulin

   Title: General model of phospholipid bilayers in fluid phase within single chain mean field theory

BIBLIOGRAPHY

[1] *See "Normativa per a la Presentaciò d'una tesi doctoral per compendi de publicacions"*, Departament d'Enginyeria Química of the Universitat Rovira i Virgili, **Oct. 2009**.

[2] B. Alberts, *Molecular Biology of the Cell*, 5th, Garland Science, New York, **2008**.

[3] G. M. Cooper, R. E. Hausman, *The Cell: a Molecular Approach*, 5th, Sinauer Associates Inc., Sunderland, **2009**.

[4] O. G. Mouritsen, *Life - As a Matter of Fat: The Emerging Science of Lipidomics*, en, Springer Science & Business Media, **Nov. 2004**.

[5] D. P. Clark, *Molecular Biology: Academic Cell Update Edition*, en, Academic Press, **Dec. 2009**.

[6] G. Karp, *Cell and Molecular Biology: Concepts and Experiments*, en, John Wiley & Sons, **Oct. 2009**.

[7] G. Cevc, D. Marsh, *Phospholipid Bilayers: Physical Principles and Models*, 1 edition, English, Wiley-Interscience, New York, **May 1987**.

[8] P. L. Yeagle, *The Structure of Biological Membranes*, 2nd, CRC Press, **2005**.

[9] R. Lipowsky, E. Sackmann, *Structure and Dynamics of Membranes: I. From Cells to Vesicles / II. Generic and Specific Interactions*, en, Elsevier, **June 1995**.

[10] R. O. Potts, *Mechanisms of Transdermal Drug Delivery*, en, CRC Press, **July 1997**.

[11] D. Pan, *Nanomedicine: A Soft Matter Perspective*, en, CRC Press, **July 2014**.

[12] W. M. S. P. i. t. S. o. C. E. C. University, *Drug Delivery : Engineering Principles for Drug Therapy: Engineering Principles for Drug Therapy*, en, Oxford University Press, USA, **Feb. 2001**.

[13] S. M. Moghimi, A. C. Hunter, J. C. Murray, *FASEB J.* **2005**, *19*, 311–330.

[14] R. A. Petros, J. M. DeSimone, en, *Nat Rev Drug Discov* **Aug. 2010**, *9*, 615–627.

[15] A. Nan et al., *Nano Lett.* **Aug. 2008**, *8*, 2150–2154.

[16] T. M. Allen, P. R. Cullis, en, *Science* **Mar. 2004**, *303*, 1818–1822.

[17] M. Wöhr et al., *International Journal of Hydrogen Energy* **Mar. 1998**, *23*, 213–218.

[18] L. Y. T. Chou, W. C. W. Chan, en, *Nat Nano* **July 2012**, *7*, 416–417.

[19] G. Oberdörster, E. Oberdörster, J. Oberdörster, *Environmental Health Perspectives* **2005**, *113*, 823–839.

112   Bibliography

[20]   V. E. Kagan, H. Bayir, A. A. Shvedova, *Nanomedicine: Nanotechnology Biology and Medicine* **Dec. 2005**, *1*, 313–316.

[21]   H. Kamaya, S. Kaneshina, I. Ueda, *Biochimica et Biophysica Acta (BBA) - Biomembranes* **Aug. 1981**, *646*, 135–142.

[22]   R. Ph, J. Se, G. J, eng, *Anesthesiology* **May 1977**, *46*, 322–326.

[23]   N. Rapoport et al., *Journal of Controlled Release*, Eighth International Nanomedicine and Drug Delivery Symposium **July 2011**, *153*, 4–15.

[24]   A. K. Gupta, M. Gupta, *Biomaterials* **June 2005**, *26*, 3995–4021.

[25]   N. Wisniewski, M. Reichert, *Colloids and Surfaces B: Biointerfaces* **Oct. 2000**, *18*, 197–219.

[26]   N. Bistolas et al., *Biosensors and Bioelectronics*, 20th Anniversary of Biosensors and Bioelectronics20th Anniversary of Biosensors and Bioelectronics **June 2005**, *20*, 2408–2423.

[27]   E. W. Flick, *Cosmetic and Toiletry Formulations*, en, Elsevier, **June 2014**.

[28]   S. Mann, en, *Nat Mater* **Oct. 2009**, *8*, 781–792.

[29]   G. Binnig, C. F. Quate, C. Gerber, *Phys. Rev. Lett.* **Mar. 1986**, *56*, 930–933.

[30]   J. Korlach et al., en, *PNAS* **July 1999**, *96*, 8461–8466.

[31]   A. R. Spurr, *Journal of Ultrastructure Research* **Jan. 1969**, *26*, 31–43.

[32]   S. W. Lovesey, **1984**.

[33]   B. E. Warren, *X-ray Diffraction*, en, Courier Corporation, **1969**.

[34]   M. Montal, P. Mueller, en, *PNAS* **Dec. 1972**, *69*, 3561–3566.

[35]   R. Bandyopadhyaya et al., *Chemical Engineering Science* **Aug. 1998**, *53*, 2799–2807.

[36]   R. D. Groot, K. L. Rabone, *Biophysical Journal* **Aug. 2001**, *81*, 725–736.

[37]   A. Z. Panagiotopoulos et al., *Molecular Physics* **Mar. 1988**, *63*, 527–545.

[38]   M. Arroyo, T. Belytschko, *Journal of the Mechanics and Physics of Solids* **Sept. 2002**, *50*, 1941–1977.

[39]   J. A. Elliott et al., en, *Phys. Chem. Chem. Phys.* **Jan. 1999**, *1*, 4855–4863.

[40]   D. Hofmann et al., en, *Macromol. Theory Simul.* **July 2000**, *9*, 293–327.

[41]   D. Frenkel, B. Smit, *Understanding Molecular Simulation: from Algorithms to Applications*, Academic Press, San Diego, **2002**.

[42]   R. J. Sadus, *Molecular Simulation of Fluids*, en, Elsevier, **2002**.

[43]   M. Tuckerman, *Statistical Mechanics: Theory and Molecular Simulation*, en, OUP Oxford, **Feb. 2010**.

[44]   K. E. Gubbins, N. Quirke, *Molecular Simulation and Industrial Applications: Methods, Examples, and Prospects*, en, Taylor & Francis, **1996**.

[45] M. Khodakovskaya et al., *AcsNano* **2009**, *3*, 3221–3227.

[46] P. Balbuena, J. M. Seminario, *Molecular Dynamics: From Classical to Quantum Methods*, en, Elsevier, **Apr. 1999**.

[47] Goodfellow, *Molecular Dynamics: Applications in Molecular Biology*, en, CRC Press, **1990**.

[48] K. B. I. f. P. J. G.-U. Mainz, *Monte Carlo and Molecular Dynamics Simulations in Polymer Science*, en, Oxford University Press, USA, **July 1995**.

[49] M. N. Rosenbluth, A. W. Rosenbluth, *J. Chem. Phys.* **1955**, *23*, 356–359.

[50] K. Binder, *Monte Carlo and Molecular Dynamics Simulations Polymer*, Oxford University Press, Inc., New York, NY, USA, **1995**.

[51] E. S. Boek, P. V. Coveney, N. T. Skipper, *J. Am. Chem. Soc.* **Dec. 1995**, *117*, 12608–12617.

[52] Y. Guo, S. Pogodin, V. A. Baulin, eng, *J Chem Phys* **May 2014**, *140*, 174903.

[53] G. Weber et al., en, *Soft Matter* **May 2014**, *10*, 4241–4247.

[54] Y. Guo, V. A. Baulin, F. Thalmann, en, *Soft Matter* **Dec. 2015**, *12*, 263–271.